J. Fluid Mech. (2023), *vol*. 969, A14, doi:10.1017/jfm.2023.571

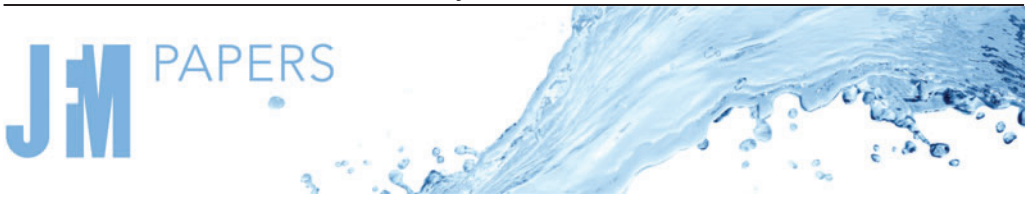

Spatio-temporal fluctuations of interscale and interspace energy transfer dynamics in homogeneous turbulence

H.S. Larssen[1],† **and J.C. Vassilicos**[1,2],†

[1]Department of Mathematics, Imperial College London, London SW7 2AZ, UK

[2]UMR 9014 - LMFL - Laboratoire de Mécanique des fluides de Lille - Kampé de Feriet, Univ. Lille, CNRS, ONERA, Arts et Métiers ParisTech, Centrale Lille, F-59000 Lille, France

(Received 8 August 2022; revised 18 May 2023; accepted 4 July 2023)

We study fluctuations of all co-existing energy exchange/transfer/transport processes in stationary periodic turbulence including those that average to zero and are not present in average cascade theories. We use a Helmholtz decomposition of accelerations that leads to a decomposition of all terms in the Kármán–Howarth–Monin–Hill (KHMH) equation (scale-by-scale two-point energy balance) causing it to break into two energy balances, one resulting from the integrated two-point vorticity equation and the other from the integrated two-point pressure equation. The various two-point acceleration terms in the Navier–Stokes difference (NSD) equation for the dynamics of two-point velocity differences have similar alignment tendencies with the two-point velocity difference, implying similar characteristics for the NSD and KHMH equations. We introduce the two-point sweeping concept and show how it articulates with the fluctuating interscale energy transfer as the solenoidal part of the interscale transfer rate does not fluctuate with turbulence dissipation at any scale above the Taylor length but with the sum of the time derivative and the solenoidal interspace transport rate terms. The pressure fluctuations play an important role in the interscale and interspace turbulence transfer/transport dynamics as the irrotational part of the interscale transfer rate is equal to the irrotational part of the interspace transfer rate and is balanced by two-point fluctuating pressure work. We also study the homogeneous/inhomogeneous decomposition of interscale transfer. The statistics of the latter are skewed towards forward cascade events whereas the statistics of the former are not. We also report statistics conditioned on intense forward/backward interscale transfer events.

Key words: turbulence theory, intermittency

† Email addresses for correspondence: h.larssen18@imperial.ac.uk, john-christos.vassilicos@cnrs.fr

1. Introduction

Modelling of turbulence dissipation is a cornerstone of one-point turbulent flow prediction methods based on the Reynolds-averaged Navier–Stokes (RANS) equations such as the widely used k–ε and the k–ω models (see Pope 2000; Leschziner 2016) and also of two-point turbulence flow prediction methods based on filtered Navier–Stokes (NS) equations, namely large eddy simulations (LES) (see Pope 2000; Sagaut 2000). The turbulence dissipation rate away from walls is intimately linked to the turbulence cascade (Pope 2000; Vassilicos 2015). The physical understanding of this cascade that, to this day, has underpinned these prediction methods is based on Kolmogorov's average cascade in statistically homogeneous and stationary turbulence. Notwithstanding recent advances that have shown that the turbulence dissipation and cascade are different from Kolmogorov's both in non-stationary (see, e.g. Vassilicos 2015; Goto & Vassilicos 2016; Steiros 2022) and in non-homogeneous turbulence (Chen *et al.* 2021; Chen & Vassilicos 2022), Kolmogorov's cascade is in fact valid only as an average cascade even in homogeneous stationary turbulence. Turbulence has been known to be intermittent since the late 1940s (see Frisch (1995) and references therein), and this intermittency has mainly been taken into account as structure function exponent corrections to Kolmogorov's average picture. However, studies such as those by Schumacher *et al.* (2014) and Yasuda & Vassilicos (2018) examined intermittent fluctuations without reference to structure function exponents that require high Reynolds numbers to be well defined and to be predicted from Kolmogorov's theory or various intermittency-accounting variants of this theory (see Frisch (1995) and references therein). Yasuda & Vassilicos (2018) concentrated their attention on the actual fundamental basis of Kolmogorov's theory that is scale-by-scale equilibrium for statistically homogeneous and stationary turbulence, and not on the theory's structure function and energy spectrum scaling consequences. The scale-by-scale equilibrium implied by statistical homogeneity and stationarity is that the average interscale turbulence energy transfer rate is balanced by nothing more than the average scale-by-scale viscous diffusion rate, average turbulence dissipation rate and average energy input rate by a stirring force, irrespective of Reynolds number (except that the Reynolds number needs to be large enough for the presence of random fluctuations). It is most natural for a study of intermittency to start with the fluctuations around this balance, which means that along with the fluctuations of interscale transfer, dissipation, diffusion and energy input, all other fluctuating turbulent energy change rates need to be taken into account as well even if their spatio-temporal average is zero in statistically stationary homogeneous turbulence. The intermittency corrections to Kolmogorov's average cascade theory that have been developed since the 1960s (see, e.g. Frisch 1995; Sreenivasan & Antonia 1997) are often based on the intermittent fluctuations of the local (in space and time) turbulence dissipation rate, yet Yasuda & Vassilicos (2018) demonstrated that these dissipation fluctuations are much less intense than the fluctuations of other turbulent energy change rates such as the nonlinear interspace energy transfer rate (which is a scale-by-scale rate of turbulent transport in physical space), the fluctuating work resulting from the correlation of the fluctuating pressure gradient with the fluctuating velocity and the time derivative of the scale-by-scale turbulent kinetic energy. Yasuda & Vassilicos (2018) made these observations using direct numerical simulations (DNS) of statistically stationary periodic turbulence at low to moderate Taylor length-based Reynolds numbers from about 80 to 170. Even though their Reynolds numbers were not high enough to test the high-Reynolds-number scaling consequences of Kolmogorov's theory, they observed an energy spectrum with a near-decade power law range where the power law exponent was not too far from Kolmogorov's $-5/3$.

However, they did not observe a significant range of scales where the scale-by-scale equilibrium reduces to a scale-by-scale balance between average interscale turbulence energy transfer rate and average turbulence dissipation as predicted by the Kolmogorov theory for statistically stationary homogeneous turbulence at asymptotically high Reynolds numbers. This high-Reynolds-number scale-by-scale equilibrium is the hallmark of the Kolmgorov average cascade and is typically not put in question by existing intermittency corrections to Kolmogorov's theory (see, e.g. Frisch 1995).

Given the low to moderate Reynolds numbers of the DNS used by Yasuda & Vassilicos (2018), their observations concern interscale turbulence energy transfers more than the turbulence cascade *per se* if the concept of turbulence cascade is taken to have meaning only at very large Reynolds numbers. They demonstrated that an interscale transfer picture appears that is radically different from Kolmogorov's if the average is lifted and all spatio-temporal intermittent fluctuations are taken into account. This different picture involves highly fluctuating processes that vanish on average in statistically stationary and homogeneous turbulence and are not taken into account by the Kolmogorov theory for that very reason. We stress once more that Yasuda & Vassilicos (2018) made this demonstration in statistically homogeneous and stationary turbulence, the very type of turbulence that Kolmogorov's theory has been designed for.

It is hard to imagine that the complex turbulence energy transfer picture educed by the DNS of Yasuda & Vassilicos (2018) does not survive at asympotically high Reynolds numbers because it is known that the small-scale turbulence becomes increasingly intermittent with increasing Reynolds number (see, e.g. Frisch 1995; Sreenivasan & Antonia 1997). A DNS study at higher Reynolds numbers is nevertheless needed to ascertain this point. However, this is not the study proposed in this paper. In this paper our aim is to gain deeper insight into the fluctuating energy transfer picture revealed by the DNS of Yasuda & Vassilicos (2018) and we do this in terms of Helmholtz decomposed solenoidal and irrotational acceleration fields. Given that the computational cost involved in this Helmholtz decomposition is high (see following two sections) it is not possible for us to carry out our study for a variety of increasing Reynolds numbers and thereby combine it with a Reynolds number dependence study. We therefore limit ourselves to Reynolds numbers comparable to those of Yasuda & Vassilicos (2018).

The radically different turbulence energy transfer picture that appears when all intermittent turbulence fluctuations are taken into account exhibits correlations between fluctuations of different processes: in particular, the fluctuating pressure–velocity term mentioned above is correlated with the interscale energy transfer rate, and the time derivative of the turbulent kinetic energy below a certain two-point length r is correlated with the interspace energy transport rate at the same length r. Yasuda & Vassilicos (2018) explained the former correlation as resulting from the link between nonlinearity and non-locality (via the pressure field) and the latter correlation as reflecting the passive sweeping of small turbulent eddies by large ones (Tennekes 1975). However, this sweeping (also termed 'random Taylor hypothesis') has been studied by reference to the one-point incompressible NS equation (e.g. Tennekes 1975; Tsinober, Vedula & Yeung 2001) rather than the two-point Kármán–Howarth–Monin–Hill (KHMH) equation, used by Yasuda & Vassilicos (2018) in their study of the fluctuating turbulence cascade. The KHMH equation is a scale-by-scale energy budget local in space and time, directly derived from the incompressible NS equations for the instantaneous velocity field (see Hill 2002) without decomposition (e.g. Reynolds decomposition), without averages (e.g. Reynolds averages) and without any assumption made about the turbulent flow (e.g. homogeneity, isotropy, etc.). The initial motivation of the present paper is to substantiate the claim of

Yasuda & Vassilicos (2018) concerning correlations being caused by random sweeping by translating the sweeping analysis of Tsinober *et al.* (2001) to the KHMH equation. It is in doing so that we use the Helmholtz decomposition that Tsinober *et al.* (2001) introduced for the analysis of the acceleration field. We apply it to the two-point Navier–Stokes difference (NSD) equation (which is the equation governing the dynamics of two-point velocity differences) and the KHMH equation that derives from it. This decomposition into solenoidal and irrotational terms breaks the NS equation into two equations, one being the irrotational balance between nonlinearity and non-locality (pressure) and the other being the solenoidal balance between local unsteadiness and advection that encapsulates the sweeping. With this decomposition we substantiate all the correlations observed by Yasuda & Vassilicos (2018) between different KHMH terms representing different energy change processes, not only those caused by sweeping. In fact, we educe the relation between interspace turbulence energy transfer/transport and two-point sweeping (i.e. the random Taylor hypothesis that we generalize to two-point statistics), and we extend the correlation study to solenoidal and irrotational sub-terms of the KHMH equation that leads to even stronger correlations than those found by Yasuda & Vassilicos (2018). This approach sheds some light on the way that two-point sweeping and interscale energy transfer relate to each other. We then ask whether the scale-by-scale equilibrium that is at the basis of Kolmogorov's theory and that disappears when the average is lifted does nevertheless exist locally at relatively high energy transfer events, a question that leads us to consider whether two-point sweeping also holds at such events. Finally, we study the recently introduced decomposition (Alves Portela, Papadakis & Vassilicos 2020) of the interscale transfer rate into a homogeneous and an inhomogeneous interscale transfer component. We analyse their fluctuations and the correlations of these fluctuations, both unconditionally and conditionally on relatively rare intense interscale transfer events.

In the following section we introduce our DNS of forced periodic turbulence. Section 3.1 is a reminder of the application of this decomposition to the one-point NS equation by Tsinober *et al.* (2001). In this subsection we also validate our DNS by retrieving the conclusions of Tsinober *et al.* (2001) on sweeping and by comparing our DNS results on one-point acceleration dynamics to theirs. In §§ 3.2 and 3.3 we apply the Helmholtz decomposition to the two-point NSD equation for the case of homogeneous/periodic turbulence and in § 3.4 we derive from the Helmholtz decomposed NSD equations corresponding KHMH equations. Section 3.4 formalises the connection between the NS and KHMH dynamics, clarifies under which conditions a link exists between NS and KHMH dynamics and provides results on scale and Reynolds number dependencies of the KHMH dynamics. By considering the NSD dynamics in terms of solenoidal and irrotational dynamics, we derive two new KHMH equations. In § 4 we use these two new KHMH equations to obtain new results on the fluctuating cascade dynamics across scales both unconditionally and conditionally on rare extreme interscale energy transfer events. In § 5 we analyse the inhomogeneous and homogeneous contributions to the interscale energy transfer rate. Finally, § 6 summarises our results.

2. The DNSs of body-forced period turbulence

Our study requires turbulence data from a turbulent flow where the Kolmogorov equilibrium theory for statistically homogeneous and stationary turbulence is applicable. We therefore follow Yasuda & Vassilicos (2018) and perform DNS of body-forced periodic NS turbulence with the same pseudo-spectral code that they used. This code solves

N	$\langle Re_\lambda \rangle_t$	$\nu/10^3$	$k_{max}\langle \eta \rangle_t$	$2\pi/\langle L \rangle_t$	$\langle \lambda \rangle/\langle L \rangle_t$	T_s/T	$\Delta T/T$
256	112	1.80	1.88	5.6	3.5	21	0.01
512	174	0.72	1.89	5.4	5.2	27	0.12

Table 1. Specifications of the numerical simulations. Here N denotes the number of grid points in each Cartesian coordinate, Re_λ the Taylor-scale Reynolds number, ν the kinematic viscosity, $k_{max} = \sqrt{2}/3N$ is the highest resolved wavenumber, η and λ are, respectively, the Kolmogorov and Taylor lengths and $\langle \cdots \rangle_t$ denotes a time average; L is the integral lengths calculated from the three-dimensional energy spectrum $E(k, t)$: $L(t) = (3\pi/4)\int_0^\infty k^{-1}E(k, t)\,\mathrm{d}k/K(t)$, where $K(t)$ is the kinetic energy per unit mass; T_s denotes the total sampling time over which converged statistics are calculated by sampling randomly in space–time, ΔT denotes the time between samples and $T \equiv \langle L \rangle_t/\sqrt{2/3\langle K \rangle_t}$ is the turnover time.

numerically the vorticity equation

$$\frac{\partial \boldsymbol{\omega}}{\partial t} = \boldsymbol{\nabla}_{\boldsymbol{x}} \times (\boldsymbol{u} \times \boldsymbol{\omega}) + \nu \nabla_{\boldsymbol{x}}^2 \boldsymbol{\omega} + \boldsymbol{\nabla}_{\boldsymbol{x}} \times \boldsymbol{f}, \tag{2.1}$$

subjected to the continuity equation

$$\boldsymbol{\nabla}_{\boldsymbol{x}} \cdot \boldsymbol{u} = 0, \tag{2.2}$$

where $\boldsymbol{u}(\boldsymbol{x}, t)$, $\boldsymbol{f}(\boldsymbol{x}, t)$ and $\boldsymbol{\omega}(\boldsymbol{x}, t)$ are the velocity, force and vorticity fields, respectively, and ν is the kinematic viscosity. All fields are 2π periodic in each one of the three orthogonal spatial coordinates x_1, x_2 and x_3, and $\boldsymbol{x} = (x_1, x_2, x_3)$. The pseudo-spectral method is fully dealised with a combination of phase shifting and spherical truncation (Patterson & Orszag 1971). The forcing method is a negative damping forcing (Linkmann & Morozov 2015; McComb *et al.* 2015*b*)

$$\hat{\boldsymbol{f}}(\boldsymbol{k}, t) = (\epsilon_W/2K_f)\hat{\boldsymbol{u}}(\boldsymbol{k}, t) \quad \text{for } 0 < |\boldsymbol{k}| < k_f, \tag{2.3}$$

$$= 0 \quad \text{otherwise}, \tag{2.4}$$

where $\hat{\boldsymbol{f}}(\boldsymbol{k}, t)$ and $\hat{\boldsymbol{u}}(\boldsymbol{k}, t)$ are the Fourier transforms of $\boldsymbol{f}(\boldsymbol{x}, t)$ and $\boldsymbol{u}(\boldsymbol{x}, t)$, respectively, k_f is the cutoff wavenumber, ϵ_W is the energy input rate per unit mass and K_f is the kinetic energy per unit mass in the wavenumber band $0 < |\boldsymbol{k}| < k_f$. Note that this forcing is incompressible and has therefore no irrotational part. The addition of a potential, i.e. irrotational, term to the forcing would effectively just be subsumed into the pressure required to keep the flow incompressible.

We perform two DNS of forced periodic/homogeneous turbulence with forcing parameters $\epsilon_W = 0.1$ and $k_f = 2.5$ at both simulation sizes 256^3 grid points and 512^3 grid points. Average statistics are given in table 1. For these two simulation sizes respectively, deviations around these averages are as follows: the standard deviations of L are $0.007L_b$ and $0.006L_b$ (where $L_b = 2\pi$) and the maximum L values are $0.188L_b$ and $0.202L_b$; the standard deviations of λ are 2.5 % and 3.7 % of $\langle \lambda \rangle_t$; and the standard deviation of $k_{max}\eta$ are 0.025 and 0.035.

McComb *et al.* (2015*a*) performed DNS with the same combinations of N, ν and forcing as in our simulations. The time-averaged Taylor-scale Reynolds numbers $\langle Re_\lambda \rangle_t$, the ratios of the box size to the time-averaged integral length $2\pi/\langle L \rangle_t$ and the time-averaged Kolmogorov microscales $\langle \eta \rangle_t$ are all very similar (and $\langle \ldots \rangle_t$ denotes a time average). This study reports slightly poorer small-scale resolution $k_{max}\langle \eta \rangle_t$ than ours due to their more severe spherical truncation for dealiasing.

We have also verified that the results do not significantly change when the flow is forced at small wavenumbers with an ABC forcing with $A = B = C$ (Podvigina & Pouquet 1994). In contrast to the negative damping forcing, this forcing is independent of time and of the velocity field and is also maximally helical as $\boldsymbol{\nabla}_{\boldsymbol{x}} \times \boldsymbol{f}$ is parallel to $\boldsymbol{f}$ (Galanti & Tsinober 2000). The helicity input of the ABC forcing has been studied in the context of the energy cascade in terms of its effect on the dissipation coefficient in Linkmann (2018).

Our Reynolds numbers are relatively limited due to the high computational expense of our NSD and KHMH post-processing (which is typically at least one order of magnitude more expensive than DNSs). We detail the computational expense of the post-processing once the relevant terms have been introduced in § 3.3.

In the following section we show how we apply the Helmholtz decomposition to the KHMH equation. We start in § 3.1 by applying this decomposition to the one-point NS equation following Tsinober *et al.* (2001). In this subsection we also validate our DNS by retrieving the conclusions of Tsinober *et al.* (2001), in particular on sweeping, and by comparing our DNS results on one-point acceleration dynamics to theirs. In §§ 3.2 and 3.3 we apply the Helmholtz decomposition to the two-point NSD equation for the case of homogeneous/periodic turbulence and in § 3.4 we derive from the Helmholtz decomposed NSD equations corresponding KHMH equations.

3. Helmholtz decomposition of two-point NS dynamics and corresponding turbulent energy exchanges

3.1. *Solenoidal and irrotational acceleration fluctuations*

The Helmholtz decomposition states that a twice continously differentiable three-dimensional vector field $\boldsymbol{q}(\boldsymbol{x}, t)$ defined on a domain $V \subseteq \mathbb{R}^3$ can be expressed as the sum of an irrotational vector field $\boldsymbol{q}_I(\boldsymbol{x}, t)$ and a solenoidal vector field $\boldsymbol{q}_S(\boldsymbol{x}, t)$ (Helmholtz 1867; Stewart 2012; Bhatia *et al.* 2013),

$$\boldsymbol{q}_I(\boldsymbol{x},\, t) = -\boldsymbol{\nabla}_x \phi(\boldsymbol{x},\, t), \quad \boldsymbol{q}_S(\boldsymbol{x},\, t) = \boldsymbol{\nabla}_x \times \boldsymbol{B}(\boldsymbol{x},\, t), \tag{3.1a,b}$$

where $\phi(\boldsymbol{x}, t)$ is a scalar potential and $\boldsymbol{B}(\boldsymbol{x}, t)$ is a vector potential. The Helmholtz decomposition and its interpretation can be applied to any vector field $\boldsymbol{q}(\boldsymbol{x}, t)$ satisfying the above conditions, and Tsinober *et al.* (2001) applied it to fluid accelerations and the incompressible NS equation.

The solenoidal and irrotational NS equations in homogeneous/periodic turbulence can be derived from the incompressible NS equation in Fourier space (see Appendix A). After transformation back to physical space, one obtains

$$\frac{\partial \boldsymbol{u}}{\partial t} + (\boldsymbol{u} \cdot \boldsymbol{\nabla}_{\boldsymbol{x}} \boldsymbol{u})^{\mathrm{T}} = \nu \nabla_{\boldsymbol{x}}^2 \boldsymbol{u} + \boldsymbol{f}^{\mathrm{T}}, \tag{3.2}$$

$$(\boldsymbol{u} \cdot \boldsymbol{\nabla}_{\boldsymbol{x}} \boldsymbol{u})^{L} = -\frac{1}{\rho} \boldsymbol{\nabla}_{\boldsymbol{x}} p + \boldsymbol{f}^{L}, \tag{3.3}$$

where the superscripts L and T denote fields obtained from longitudinal and transverse parts of respective Fourier vector fields (see Appendix A for precise definitions and Pope (2000); Stewart (2012)), $p = p(\boldsymbol{x}, t)$ is the pressure field and ρ is the density. For any periodic vector field $\boldsymbol{q}$, $\boldsymbol{q}^L$ equals the irrotational field $\boldsymbol{q}_I$ and $\boldsymbol{q}^{\mathrm{T}}$ equals the solenoidal field $\boldsymbol{q}_S$ (see Appendix A and Stewart 2012). From (3.2)–(3.3), one arrives at

	$\boldsymbol{a}_c$	$\boldsymbol{a}_l$	$\boldsymbol{a}_{c_S}$	$\boldsymbol{a}_{c_I}$	$\boldsymbol{a}_p$	$\boldsymbol{a}$	$\boldsymbol{a}_\nu$	$\boldsymbol{f}$	$\langle Re_\lambda \rangle_t$
$\langle \boldsymbol{q}^2 \rangle / (3\langle \epsilon \rangle^{3/2} \nu^{-1/2})$	8.47	5.87	5.93	2.55	2.55	2.60	0.05	0.007	112
$\langle \boldsymbol{q}^2 \rangle / (3\langle \epsilon \rangle^{3/2} \nu^{-1/2})$	14.28	11.21	11.26	3.03	3.03	3.09	0.05	0.005	174
$\langle \boldsymbol{q}^2 \rangle / \langle \boldsymbol{a}_c^2 \rangle$	1	0.69	0.70	0.30	0.30	0.31	0.0062	0.00081	112
$\langle \boldsymbol{q}^2 \rangle / \langle \boldsymbol{a}_c^2 \rangle$	1	0.78	0.79	0.21	0.21	0.22	0.0038	0.00032	174

Table 2. Normalised average magnitudes $\langle \boldsymbol{q}^2 \rangle / (3\langle \epsilon \rangle^{3/2} \nu^{-1/2})$ and $\langle \boldsymbol{q}^2 \rangle / \langle \boldsymbol{a}_c^2 \rangle$ for NS accelerations and forces $\boldsymbol{q}$ defined in the fourth paragraph of § 3.1 for our two $\langle Re_\lambda \rangle_t$. The accelerations and forces $\boldsymbol{q}$ are listed on the top row, $\boldsymbol{q}^2 \equiv q_i q_i$, ϵ denotes the viscous dissipation rate and $\langle \cdots \rangle$ denotes a spatio-temporal average.

(Tsinober *et al.* 2001)

$$\frac{\partial \boldsymbol{u}}{\partial t} + (\boldsymbol{u} \cdot \boldsymbol{\nabla}_{\boldsymbol{x}} \boldsymbol{u})_S = \nu \boldsymbol{\nabla}_{\boldsymbol{x}}^2 \boldsymbol{u} + \boldsymbol{f}_S, \tag{3.4}$$

$$(\boldsymbol{u} \cdot \boldsymbol{\nabla}_{\boldsymbol{x}} \boldsymbol{u})_I = -\frac{1}{\rho} \boldsymbol{\nabla}_{\boldsymbol{x}} p + \boldsymbol{f}_I, \tag{3.5}$$

which we refer to as Tsinober equations. Equation (3.4) contains only solenoidal vector fields and (3.5) contains only irrotational vector fields. Note that in the case of an incompressible periodic velocity field, the velocity field is solenoidal, i.e. $\boldsymbol{u} = \boldsymbol{u}_S$. This follows immediately from the scalar potential ϕ being the solution to $\nabla_{\boldsymbol{x}}^2 \phi = 0$ with periodic boundary conditions for $\boldsymbol{\nabla}_{\boldsymbol{x}} \phi$, yielding $\phi = const.$

In Appendix C we show that (3.4) is the integrated vorticity equation and that (3.5) is the integrated Poisson equation for pressure. The procedure presented in Appendix C for obtaining the Tsinober equations is also used in this same appendix to obtain generalized Tsinober equations for non-homogeneous/non-periodic turbulence with arbitrary boundary conditions.

Following the notation of Tsinober *et al.* (2001), we define $\boldsymbol{a}_l \equiv \partial \boldsymbol{u} / \partial t$, $\boldsymbol{a}_c \equiv \boldsymbol{u} \cdot \boldsymbol{\nabla}_{\boldsymbol{x}} \boldsymbol{u}$, $\boldsymbol{a} \equiv \boldsymbol{a}_l + \boldsymbol{a}_c$, $\boldsymbol{a}_p \equiv -1/\rho \boldsymbol{\nabla}_{\boldsymbol{x}} p$ and $\boldsymbol{a}_\nu \equiv \nu \boldsymbol{\nabla}_{\boldsymbol{x}}^2 \boldsymbol{u}$. In such notation, (3.4)–(3.5) are $\boldsymbol{a}_l + \boldsymbol{a}_{c_S} = \boldsymbol{a}_\nu + \boldsymbol{f}_S$ and $\boldsymbol{a}_{c_I} = \boldsymbol{a}_p + \boldsymbol{f}_I$. Tsinober *et al.* (2001) in fact wrote these equations for statistically homogeneous/periodic NS turbulence without body forces, i.e. with $\boldsymbol{f} = 0$. In general, however, the body forcing can be considered, as in the present work, to be non-zero and typically incompressible, i.e. $\boldsymbol{f}_I = \boldsymbol{0}$ but $\boldsymbol{f}_s \not\equiv \boldsymbol{0}$, given that a compressible component of the forcing can be subsumed into the pressure field in incompressible turbulence. In body-forced statistically stationary homogeneous/periodic turbulence, the average forcing magnitude $\langle \boldsymbol{f}^2 \rangle$, where the brackets denote spatio-temporal averaging, tends to be small compared with $\langle \boldsymbol{a}_\nu^2 \rangle$ when the forcing is applied only to the largest scales (Vedula & Yeung 1999). Given that $\langle \boldsymbol{f} \cdot \boldsymbol{u} \rangle = \langle \epsilon \rangle$, where ϵ is the local turbulence dissipation rate, $\boldsymbol{f}^2$ can be quite small if $\boldsymbol{f}$ is not close to orthogonal to the velocity field. This is indeed the case with the negative damping and ABC forcings used in this study. In cases where $\boldsymbol{f}$ is close to orthogonal to the velocity field, which is conceivable in electromagnetic situations (Lorentz force), $\boldsymbol{f}^2$ needs to be large enough for $\langle \boldsymbol{f} \cdot \boldsymbol{u} \rangle$ to balance $\langle \epsilon \rangle$. In this study we have not considered such forcings and some of our results might not be applicable to such situations. Our results for the forcings we used indicate that $\langle \boldsymbol{f}^2 \rangle$ is indeed much smaller than $\langle \boldsymbol{a}_\nu^2 \rangle$ (see results from our DNS in table 2) and the probability to find values of $\boldsymbol{f}^2$ large enough to be comparable to the other terms in the Tsinober equations is extremely small (see results from our DNS in figure 1 and table 3) where we see, in particular, that $|\boldsymbol{f}| > 0.1 |\boldsymbol{a}_{c_S}|$ in 15.3 % and 6.3 % of the spatio-temporal

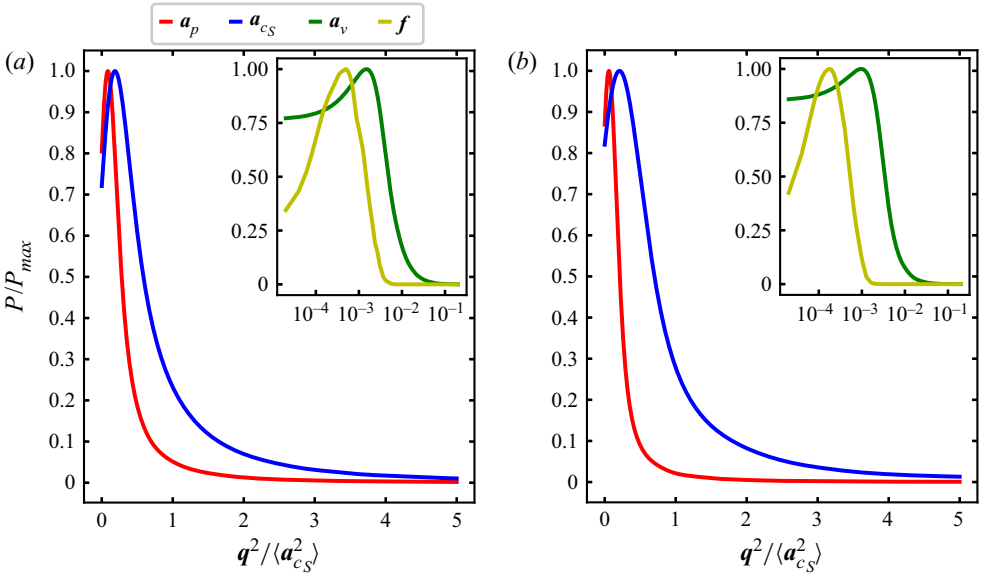

Figure 1. Probability density functions (PDFs) P of NS acceleration and force magnitudes q^2 for terms q listed at the top of (*a*). Here P_{max} for the PDF of q^2 denotes its maximum value. Results are shown for (*a*) $\langle Re_\lambda \rangle_t = 112$, (*b*) $\langle Re_\lambda \rangle_t = 174$.

α	0.001	0.01	0.1	1
Prob($a_v^2 > \alpha a_{cS}^2$)	(0.893, 0.808)	(0.441, 0.308)	(0.068, 0.037)	(0.004, 0.002)
Prob($f^2 > \alpha a_{cS}^2$)	(0.707, 0.476)	(0.155, 0.063)	(0.008, 0.003)	$(3 \times 10^{-4}, 9 \times 10^{-5})$

Table 3. Probabilities of events $q^2 > \alpha p^2$ for NS terms (q, p) with α specified on the top row. The two probability values in the brackets for each (q, p, α) combination refer to $\langle Re_\lambda \rangle_t = 112$ and $\langle Re_\lambda \rangle_t = 174$, respectively.

domain for the two Reynolds numbers, respectively, the percentage being smaller for the higher Reynolds number. If we consider $|f| > \sqrt{0.1}|a_{cS}| \approx 0.32|a_{cS}|$, we see that this is only satisfied in 0.8 % and 0.3 % of the spatio-temporal domain, respectively. Furthermore, figure 1 and table 3 show that f is also typically much smaller than a_v. We can therefore write $a_l + a_{cS} \approx a_v$, this being a good approximation in the majority of the flow for the majority of the time. With $a_{cI} = a_p$ given that $f_I = 0$, these two equations are very close to the way that Tsinober *et al.* (2001) originally wrote them ($a_l + a_{cS} = a_v$ and $a_{cI} = a_p$ for the $\mathbf{f} \equiv 0$ case) and we can therefore expect our DNS to retrieve the DNS results and conclusions of Tsinober *et al.* (2001).

The DNS of Tsinober *et al.* (2001) showed that a_v is typically negligible (i.e. in a statistical sense, not everywhere at any time in the flow) compared with all the other acceleration terms in the Tsinober equations, namely a_l, a_{cS}, a_{cI} and a_p. This is confirmed by our DNS results in tables 2–3 and in figure 1 that are for similar Reynolds numbers to those of Tsinober *et al.* (2001) and where we report root-mean-square values, and probabilities of various acceleration terms. It is worth noting that a_v is not everywhere always negligible, at these Reynolds numbers at least. For example, $|a_v| > 0.1|a_{cS}|$ in 44.1 % and 30.8 % of the space–time domain for our lower and higher Reynolds number,

respectively; and if we consider $|\boldsymbol{a}_v| > 0.32|\boldsymbol{a}_{cS}|$, this is satisfied in 6.8 % and 3.7 % of cases. Note that the DNS results of Tsinober *et al.* (2001) suggest that the viscous force typically decreases in magnitude compared with $\boldsymbol{a}_{cS}$ as the Reynolds number increases and our results for our two Reynolds numbers agree with this trend. One may therefore expect the first of the two Tsinober equations for homogeneous/periodic turbulence with the kind of forcing we consider here to typically reduce to

$$\boldsymbol{a}_I + \boldsymbol{a}_{cS} \approx 0 \tag{3.6}$$

at high enough Reynolds numbers, the approximation being valid in the sense that the neglected terms are significantly smaller than the retained ones in the majority of the flow for the majority of the time. There exist, however, some relatively rare spatio-temporal events where the neglegted viscous force and/or body force are significant (for example, as stated a few lines above, $|\boldsymbol{a}_v|$ is larger than $0.32|\boldsymbol{a}_{cS}|$ in 6.8 % and 3.7 % of all spatio-temporal events for our lower and higher Reynolds numbers, respectively) and where the right-hand side of (3.6) is therefore not zero. In fact, many of these relatively rare events can be expected to account for some or even much of the average turbulence dissipation that is a sum of squares of fluctuating velocity gradients. More generally, one cannot use (3.6) to derive statistics of fluctuating velocity gradients, as in Tang, Antonia & Djenidi (2022) for example.

The second of the two Tsinober equations, namely

$$\boldsymbol{a}_{cI} = \boldsymbol{a}_p, \tag{3.7}$$

is exact everywhere and at any time and we keep it as it is.

Equations (3.6)–(3.7) suggest similar magnitudes and strong alignment between $\boldsymbol{a}_I$ and $-\boldsymbol{a}_{cS}$ and equal magnitudes as well as perfect alignment between $\boldsymbol{a}_{cI}$ and $\boldsymbol{a}_p$. Such magnitudes and alignments were observed in the DNS of Tsinober *et al.* (2001) and are also strongly confirmed by our own DNS in table 4 ($\boldsymbol{a}_{cS}$ and $\boldsymbol{a}_{cI}$ are calculated on the basis of (A1*a*,*b*) in Appendix A and aliasing errors associated with nonlinear terms are removed by phase shifting and truncation Patterson & Orszag 1971). As suggested by previous DNS and experimental results (e.g. Tsinober *et al.* 2001; Chevillard *et al.* 2005; Yeung *et al.* 2006), and as also supported by our own DNS results in tables 2 and 4, $\boldsymbol{a} \approx \boldsymbol{a}_p$ and $\langle \boldsymbol{a}_I^2 \rangle / \langle \boldsymbol{a}^2 \rangle \sim \langle Re_\lambda \rangle_t^{1/2}$. In fact, the scaling $\langle \boldsymbol{a}_I^2 \rangle / \langle \boldsymbol{a}^2 \rangle \sim \langle Re_\lambda \rangle_t^{1/2}$ follows from the analysis of Tennekes (1975) who expressed the concept of passive sweeping by pointing out that 'at high Reynolds number the dissipative eddies flow past an Eulerian observer in a time much shorter than the time scale which characterizes their own dynamics'. It then follows from (3.6)–(3.7), from $\langle \boldsymbol{a}_I^2 \rangle / \langle \boldsymbol{a}^2 \rangle \sim \langle Re_\lambda \rangle_t^{1/2}$ and from $\langle \boldsymbol{a}_p^2 \rangle \approx \langle \boldsymbol{a}^2 \rangle$ that $\langle \boldsymbol{a}_{cS}^2 \rangle / \langle \boldsymbol{a}_{cI}^2 \rangle \sim \langle Re_\lambda \rangle_t^{1/2}$ with increasing $\langle Re_\lambda \rangle_t$, i.e. $\boldsymbol{a}_c$ becomes increasingly solenoidal with increasing $\langle Re_\lambda \rangle_t$. In this way, the anti-alignment in (3.6) leads to an increasing anti-alignment tendency between $\boldsymbol{a}_I$ and $\boldsymbol{a}_c$ with increasing Reynolds number, which is consistent with the notion of passive sweeping of small eddies by large ones, i.e. the random Taylor hypothesis of Tennekes (1975). These observations and conclusions were all made by Tsinober *et al.* (2001). They are now confirmed by our DNS results in table 2 and this reiterates that they do not require a large Taylor length-based Reynolds number to emerge.

As a final point, it is a general property of isotropic random vector fields $\boldsymbol{q}$ that $\langle \boldsymbol{q}_I(\boldsymbol{x}, t) \cdot \boldsymbol{q}_S(\boldsymbol{x} + \boldsymbol{r}, t) \rangle_x = 0$ for any $\boldsymbol{r}$ (including $\boldsymbol{r} = 0$), where $\langle \cdots \rangle_{\boldsymbol{x}}$ signifies a spatial average (Monin, Yaglom & Lumley 1975). Thus, $\langle \boldsymbol{a}_c^2 \rangle = \langle \boldsymbol{a}_{cI}^2 \rangle + \langle \boldsymbol{a}_{cS}^2 \rangle$ if the small-scale turbulence is isotropic. Both our DNS and the DNS of Tsinober *et al.* (2001) confirm this equality. From this equality and from (3.6), $\langle \boldsymbol{a}_{cS}^2 \rangle / \langle \boldsymbol{a}_{cI}^2 \rangle \sim \langle Re_\lambda \rangle_t^{1/2}$, (3.7), $\boldsymbol{a} \approx \boldsymbol{a}_p$ and

$\langle Re_\lambda\rangle_t$	$\langle\cos(\boldsymbol{a}_{c_I}, \boldsymbol{a}_p)\rangle$	$\langle\cos(\boldsymbol{a}, \boldsymbol{a}_p)\rangle$	$\langle\cos(\boldsymbol{a}_l, \boldsymbol{a}_{c_S})\rangle$	$\langle\cos(\boldsymbol{a}_l, \boldsymbol{a}_c)\rangle$	$\langle\cos(\boldsymbol{a}_c, \boldsymbol{a}_p)\rangle$
112	0.9999	0.972	−0.985	−0.726	0.388
174	0.9999	0.975	−0.990	−0.796	0.308

Table 4. NS average alignments $\langle\cos(\boldsymbol{q}, \boldsymbol{p})\rangle$ for NS acceleration pairs $(\boldsymbol{q}, \boldsymbol{p})$.

$\langle \boldsymbol{a}^2\rangle \gg \langle \boldsymbol{a}_v^2\rangle \gg \langle \boldsymbol{f}^2\rangle$, we have all in all

$$\langle \boldsymbol{a}_c^2\rangle \geq \langle \boldsymbol{a}_{c_S}^2\rangle \approx \langle \boldsymbol{a}_l^2\rangle \gg \langle \boldsymbol{a}_{c_I}^2\rangle = \langle \boldsymbol{a}_p^2\rangle \approx \langle \boldsymbol{a}^2\rangle \gg \langle \boldsymbol{a}_v^2\rangle \gg \langle \boldsymbol{f}^2\rangle \tag{3.8}$$

for large enough $\langle Re_\lambda\rangle_t$. The average magnitude ordering in (3.8) is confirmed in our DNS (see table 2) and the DNS of Tsinober *et al.* (2001) even though the Reynolds numbers of these DNS are moderate and so the difference between $\langle \boldsymbol{a}_{c_I}^2\rangle$ and $\langle \boldsymbol{a}_l^2\rangle$ is not so large. Tsinober's way to formulate sweeping is encapsulated in $\langle \boldsymbol{a}_{c_S}^2\rangle \approx \langle \boldsymbol{a}_l^2\rangle \gg \langle \boldsymbol{a}_{c_I}^2\rangle = \langle \boldsymbol{a}_p^2\rangle \approx \langle \boldsymbol{a}^2\rangle$ and in the alignments implied by (3.6) and (3.7) that are also statistically confirmed by our DNS in table 4.

3.2. *From one-point to two-point NS dynamics in periodic/homogeneous turbulence*

The NSD equation at centroid $\boldsymbol{x}$ and separation vector $\boldsymbol{r}$ is derived by subtracting the NS equation at location $\boldsymbol{x}^+ = \boldsymbol{x} + \boldsymbol{r}/2$ from the NS equation at location $\boldsymbol{x}^- = \boldsymbol{x} - \boldsymbol{r}/2$. Defining $\delta\boldsymbol{q}(\boldsymbol{x}, \boldsymbol{r}, t) \equiv \boldsymbol{q}(\boldsymbol{x} + \boldsymbol{r}/2, t) - \boldsymbol{q}(\boldsymbol{x} - \boldsymbol{r}/2, t)$ for any NS term $\boldsymbol{q}(\boldsymbol{x}, t)$, the NSD equation (Hill 2002) reads

$$\frac{\partial \delta\boldsymbol{u}}{\partial t} + \delta\boldsymbol{a}_c = -\frac{1}{\rho}\nabla_{\boldsymbol{x}}\delta p + \delta\boldsymbol{a}_v + \delta\boldsymbol{f}. \tag{3.9}$$

The NSD equation governs the evolution of $\delta\boldsymbol{u}$, which can be thought of as pertaining to the momentum at scales smaller or comparable to $|\boldsymbol{r}|$. We derive the solenoidal NSD equation by subtracting (3.4) at $\boldsymbol{x} - \boldsymbol{r}/2$ from the same equation at $\boldsymbol{x} + \boldsymbol{r}/2$. The same operation is used to derive the irrotational NSD equation. The resulting equations read

$$\frac{\partial \delta\boldsymbol{u}}{\partial t} + \delta\boldsymbol{a}_{c_S} = \delta\boldsymbol{a}_v + \delta\boldsymbol{f}_S, \tag{3.10}$$

$$\delta\boldsymbol{a}_{c_I} = -\frac{1}{\rho}\nabla_{\boldsymbol{x}}\delta p + \delta\boldsymbol{f}_I, \tag{3.11}$$

where $\delta\boldsymbol{a}_{c_S}(\boldsymbol{x}, \boldsymbol{r}, t) \equiv \boldsymbol{a}_{c_S}(\boldsymbol{x} + \boldsymbol{r}/2, t) - \boldsymbol{a}_{c_S}(\boldsymbol{x} - \boldsymbol{r}/2, t)$ and $\delta\boldsymbol{a}_{c_I}(\boldsymbol{x}, \boldsymbol{r}, t) \equiv \boldsymbol{a}_{c_I}(\boldsymbol{x} + \boldsymbol{r}/2, t) - \boldsymbol{a}_{c_I}(\boldsymbol{x} - \boldsymbol{r}/2, t)$ and note that these terms refer to solenoidal and irrotational terms in $\boldsymbol{x}$ space rather than $\boldsymbol{r}$ space. The forcings we consider have no irrotational part and so $\delta\boldsymbol{f}_I = 0$. At the moderate $\langle Re_\lambda\rangle_t$ of our DNS, the approximate (3.6) is valid in the sense explained in the text that accompanies it in the previous subsection, i.e. for a majority of spatio-temporal events. If the magnitude of the separation vector $\boldsymbol{r}$ is not too small for viscosity to matter directly nor too large for the forcing to be directly present, we may safely subtract (3.6) at $\boldsymbol{x} - \boldsymbol{r}/2$ from (3.6) at $\boldsymbol{x} + \boldsymbol{r}/2$ to obtain an approximation to (3.10) for a sufficiently high Reynolds number: this is the first of the two equations below where

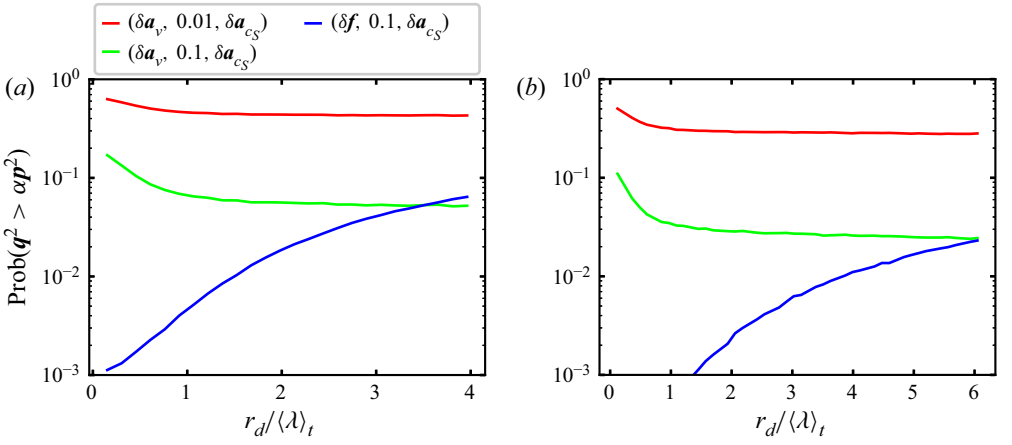

Figure 2. The NSD exceedance probabilities $\mathrm{Prob}(\boldsymbol{q}^2 > \alpha \boldsymbol{p}^2)$ for the NSD terms on top of (*a*) as a function of separation length $r_d = |\boldsymbol{r}|$. The legend entries read $(\boldsymbol{q}, \alpha, \boldsymbol{p})$ for the NSD terms introduced in the first paragraph of § 3.2. Results are shown for (*a*) $\langle Re_\lambda\rangle_t = 112$, $\langle L\rangle_t = 3.5\langle\lambda\rangle_t$; (*b*) $\langle Re_\lambda\rangle_t = 174$, $\langle L\rangle_t = 5.2\langle\lambda\rangle_t$. The NSD terms are sampled at scale $r_d = |\boldsymbol{r}|$ at random orientations $\boldsymbol{r}$.

$\delta \boldsymbol{a}_l \equiv \partial \delta \boldsymbol{u}/\partial t$,

$$\delta \boldsymbol{a}_l + \delta \boldsymbol{a}_{cS} \approx 0, \tag{3.12}$$

$$\delta \boldsymbol{a}_{cI} = -\frac{1}{\rho}\nabla_{\boldsymbol{x}} \delta p. \tag{3.13}$$

The second equation (3.13) follows directly from (3.11) with $\delta \boldsymbol{f}_I = 0$ without any restriction on either $\boldsymbol{r}$ or Reynolds number and is exact.

Like (3.6), (3.12) can be expected to be valid broadly except where and when $\delta \boldsymbol{a}_\nu + \delta \boldsymbol{f}_S$ is large enough not to be negligible. Figure 2 shows statistically converged estimations of exceedance probabilities of NSD viscous and external force terms that suggest that (3.12) is indeed a good approximation for most of space and time at the Reynolds numbers of our two DNS, at the very least for separation distances larger than $\langle\lambda\rangle_t$ and smaller than $\langle L\rangle_t$. With regards to the forcing, $\mathrm{Prob}(|\delta \boldsymbol{f}| > 0.32|\delta \boldsymbol{a}_{cS}|)$ is typically of the order of 1 %, in particular for our higher Reynolds number. With regards to the viscous force, $\mathrm{Prob}(|\delta \boldsymbol{a}_\nu| > 0.32|\delta \boldsymbol{a}_{cS}|)$ is typically of the order of 5 % for $r \geq \langle\lambda\rangle_t$ and even less for our higher Reynolds number.

The link between nonlinearity and non-locality (via the pressure field) invoked in the two-point analysis of Yasuda & Vassilicos (2018) has its root in (3.13) that parallels (3.7) and states that $\delta \boldsymbol{a}_{cI}$ and $\delta \boldsymbol{a}_p$ are perfectly aligned and have the same magnitudes. Furthermore, similarly to the way that (3.6) supports the concept of sweeping of small turbulent eddies by large ones in the usual one-point sense, (3.12) suggests similar magnitudes for and strong alignment between $\delta \boldsymbol{a}_l$ and $-\delta \boldsymbol{a}_{cS}$. A two-point concept of sweeping similar to that of Tennekes (1975) that relies on alignment between $\delta \boldsymbol{a}_l$ and $-\delta \boldsymbol{a}_c$ should also require that $\delta \boldsymbol{a}_c$ tends towards $\delta \boldsymbol{a}_{c_s}$ with increasing Reynolds number, i.e. that $\delta \boldsymbol{a}_c$ becomes increasingly solenoidal. We therefore seek to obtain inequalities and approximate equalities similar to (3.8). Note that (3.12) and (3.13) immediately imply $\langle \delta \boldsymbol{a}_{cS}^2\rangle \approx \langle \delta \boldsymbol{a}_l^2\rangle$, $\langle \delta \boldsymbol{a}_{cI}^2\rangle = \langle \delta \boldsymbol{a}_p^2\rangle$ and $\langle \delta \boldsymbol{a}_p^2\rangle \approx \langle \delta \boldsymbol{a}^2\rangle$. It therefore remains to argue that $\langle \delta \boldsymbol{a}_c^2\rangle \geq \langle \delta \boldsymbol{a}_{cS}^2\rangle \gg \langle \delta \boldsymbol{a}_{cI}^2\rangle$, which is exactly what we need to complete the new concept of two-point sweeping.

We start from

$$\langle \delta \boldsymbol{q} \cdot \delta \boldsymbol{q} \rangle(\boldsymbol{r}) = \langle \boldsymbol{q}^+ \cdot \boldsymbol{q}^+ \rangle - \langle \boldsymbol{q}^+ \cdot \boldsymbol{q}^- \rangle + \langle \boldsymbol{q}^- \cdot \boldsymbol{q}^- \rangle - \langle \boldsymbol{q}^- \cdot \boldsymbol{q}^+ \rangle, \tag{3.14}$$

$$= 2[\langle \boldsymbol{q} \cdot \boldsymbol{q} \rangle - \langle \boldsymbol{q}^+ \cdot \boldsymbol{q}^- \rangle(\boldsymbol{r})], \tag{3.15}$$

where $\boldsymbol{q}^+ \equiv \boldsymbol{q}(\boldsymbol{x} + \boldsymbol{r}/2)$ and $\boldsymbol{q}^- \equiv \boldsymbol{q}(\boldsymbol{x} - \boldsymbol{r}/2)$ and where we used $\langle \boldsymbol{q}^+ \cdot \boldsymbol{q}^+ \rangle = \langle \boldsymbol{q}^- \cdot \boldsymbol{q}^- \rangle = \langle \boldsymbol{q} \cdot \boldsymbol{q} \rangle$ because of statistical homogeneity/periodicity. Previous studies (Hill & Thoroddsen 1997; Vedula & Yeung 1999; Gulitski *et al.* 2007; Xu *et al.* 2007) demonstrated that fluid accelerations, pressure gradients and viscous forces have limited spatial correlations in terms of alignments at scales larger than $\langle \lambda \rangle_t$ for moderate and high $\langle Re_\lambda \rangle_t$. Thus, if we assume the two-point term to be negligible compared with the one-point term in (3.15) for scales $|\boldsymbol{r}|$ larger than $\langle \lambda \rangle_t$, we have that $\langle \delta \boldsymbol{q} \cdot \delta \boldsymbol{q} \rangle(\boldsymbol{r})$ is approximately equal to $2\langle \boldsymbol{q} \cdot \boldsymbol{q} \rangle$ for $|\boldsymbol{r}|$ larger than $\langle \lambda \rangle_t$. From (3.8) we therefore obtain

$$\langle \delta \boldsymbol{a}_c^2 \rangle \geq \langle \delta \boldsymbol{a}_{cS}^2 \rangle \approx \langle \delta \boldsymbol{a}_l^2 \rangle \gg \langle \delta \boldsymbol{a}_{cI}^2 \rangle = \langle \delta \boldsymbol{a}_p^2 \rangle \approx \langle \delta \boldsymbol{a}^2 \rangle \gg \langle \delta \boldsymbol{a}_\nu^2 \rangle \gg \langle \delta \boldsymbol{f}^2 \rangle \tag{3.16}$$

for $|\boldsymbol{r}|$ larger than $\langle \lambda \rangle_t$, but $\langle \delta \boldsymbol{a}_c^2 \rangle \geq \langle \delta \boldsymbol{a}_{cS}^2 \rangle$ and $\langle \delta \boldsymbol{a}_{cI}^2 \rangle = \langle \delta \boldsymbol{a}_p^2 \rangle$ are in fact valid for any $\boldsymbol{r}$. Inequality $\langle \delta \boldsymbol{a}_c^2 \rangle \geq \langle \delta \boldsymbol{a}_{cS}^2 \rangle$ follows from $\langle \delta \boldsymbol{a}_c^2 \rangle = \langle \delta \boldsymbol{a}_{cI}^2 \rangle + \langle \delta \boldsymbol{a}_{cS}^2 \rangle$ that itself follows from $\langle \boldsymbol{a}_{cI}(\boldsymbol{x}, t) \cdot \boldsymbol{a}_{cS}(\boldsymbol{x} + \boldsymbol{r}, t) \rangle_{\boldsymbol{x}} = 0$ for any $\boldsymbol{r}$ if the turbulence is isotropic (Monin *et al.* 1975). Equality $\langle \delta \boldsymbol{a}_{cI}^2 \rangle = \langle \delta \boldsymbol{a}_p^2 \rangle$ follows directly from (3.13) that is exact and holds for any $\boldsymbol{r}$ and any Reynolds number. Of equalities/inequalities (3.16), the ones that we did not already directly derive from/with (3.12) and (3.13) are $\langle \delta \boldsymbol{a}_c^2 \rangle \geq \langle \delta \boldsymbol{a}_{cS}^2 \rangle \gg \langle \delta \boldsymbol{a}_{cI}^2 \rangle$ and $\langle \delta \boldsymbol{a}_\nu^2 \rangle \gg \langle \delta \boldsymbol{f}^2 \rangle$. The present way to formulate the new concept of two-point sweeping follows from Tsinober's way to formulate sweeping and is encapsulated in $\delta \boldsymbol{a}_{cS}^2 \rangle \approx \langle \delta \boldsymbol{a}_l^2 \rangle \gg \langle \delta \boldsymbol{a}_{cI}^2 \rangle = \langle \delta \boldsymbol{a}_p^2 \rangle \approx \langle \delta \boldsymbol{a}^2 \rangle$ and in the alignments implied by (3.12) and (3.13). We confirm (3.12), (3.13) and (3.16) with our DNS in the remainder of this subsection.

To test (3.16) with our DNS data in a manageable way, we calculate spatio-temporal averages of $\boldsymbol{r}$-orientation-averaged quantities

$$(\delta \boldsymbol{q} \cdot \delta \boldsymbol{q})^a(\boldsymbol{x}, r_d, t) \equiv \frac{1}{\pi r_d^2} \iiint_{|\boldsymbol{r}| = r_d} \delta \boldsymbol{q}(\boldsymbol{x}, \boldsymbol{r}, t) \cdot \delta \boldsymbol{q}(\boldsymbol{x}, \boldsymbol{r}, t), \mathrm{d}\boldsymbol{r}, \tag{3.17}$$

which we plot in figure 3(*a*1,*a*2) as ratios of such quantities versus the two-point length r_d. In figure 3(*a*1,*a*2) we plot spatio-temporal averages of $\boldsymbol{r}$-orientation-averaged quantities (3.17) for various acceleration/force terms in the NSD and the Helmholtz decomposed NSD equations. A comparison of relative magnitudes in the plots of figure 3(*a*1,*a*2) with relative magnitudes in table 2 makes it clear that the results are consistent with (3.16) and $\langle \delta \boldsymbol{q} \cdot \delta \boldsymbol{q} \rangle(\boldsymbol{r}) / \langle \boldsymbol{q} \cdot \boldsymbol{q} \rangle$ close to 2 for $r_d \geq \langle \lambda \rangle_t$ at both $\langle Re_\lambda \rangle_t$ to a good degree of accuracy ($\langle \delta \boldsymbol{q} \cdot \delta \boldsymbol{q} \rangle(\boldsymbol{r}) / \langle \boldsymbol{q} \cdot \boldsymbol{q} \rangle$ increases from 1.8 to 2.0 as r_d grows from $\langle \lambda \rangle_t$ to $\langle L \rangle_t$). Note, in particular, that in figure 3(*a*1,*b*1) the average quantities corresponding to $\delta \boldsymbol{a}_l$ and $\delta \boldsymbol{a}_{cS}$ overlap and those corresponding to $\delta \boldsymbol{a}_p$, $\delta \boldsymbol{a}$ and $\delta \boldsymbol{a}_{cI}$ also overlap. At scales below $\langle \lambda \rangle_t$, the average relative magnitudes change slightly, but the NSD magnitude separations still abide by (3.16), the NSD analogue to (3.8), at all scales.

In figure 3(*b*1,*b*2) we use our DNS data to plot spatio-temporal averages of $\boldsymbol{r}$-orientation-averaged cosines of angles between various NSD terms $\delta \boldsymbol{q}$ and $\delta \boldsymbol{w}$ to test for average alignments as a function of r_d. These alignment results are of course in perfect agreement with (3.13) but they are also in good agreement with (3.12) and acceptable agreement with $\delta \boldsymbol{a} \approx \delta \boldsymbol{a}_p$ (the cosine of the angle between these two acceleration vectors is higher than 0.9 for all r_d). They also show that we should not expect $\delta \boldsymbol{a}_l$ to be extremely well aligned with $-\delta \boldsymbol{a}_c$ at our moderate Reynolds numbers. This demonstrates

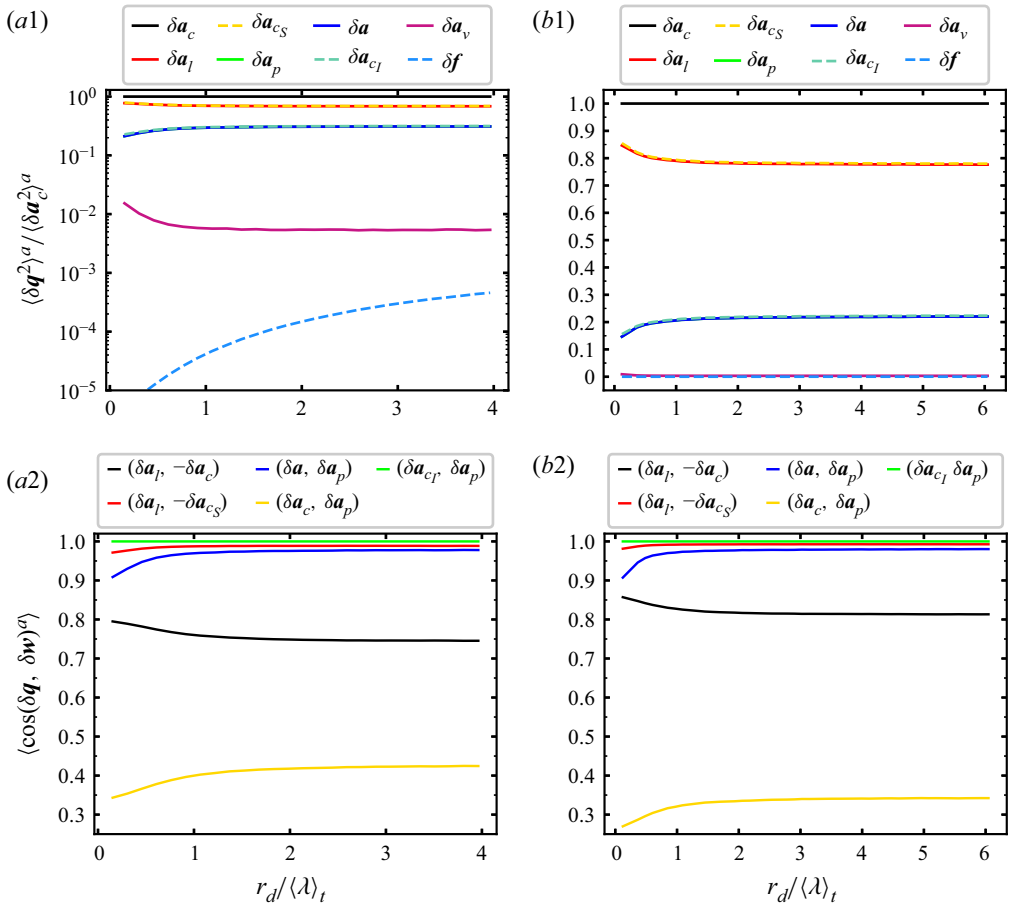

Figure 3. (*a*1,*b*1) Spatio-temporal averages of spherically averaged NSD magnitudes $(\delta q^2)^a \equiv (\pi r_d^2)^{-1} \iint_{|r|=r_d} \delta q(x, r, t) \cdot \delta q(x, r, t),\ \mathrm{d}r$ for NSD terms δq listed on top of the figures as a function of r_d: (*a*1) $\langle Re_\lambda \rangle_t = 112$, (*b*1) $\langle Re_\lambda \rangle_t = 174$. The magnitudes of the terms δa_l and δa_{c_S}) overlap and the magnitudes of the terms (δa_p, δa and δa_{c_I}) also overlap. (*a*2,*b*2) Average NSD alignments between NSD terms $(\delta q, \delta w)$ listed on top of the figures as a function of r_d: (*a*2) $\langle Re_\lambda \rangle_t = 112$, (*b*2) $\langle Re_\lambda \rangle_t = 174$.

the pertinence of the solenoidal–irrotational decomposition that has revealed very good alignments at our moderate Reynolds numbers for which there are significantly weaker alignments without this decomposition.

In conclusion, figure 3 provides strong support for (3.12), (3.13) and (3.16) that establish the two-point link between nonlinearity and non-locality, and also a concept of two-point sweeping.

3.3. *Interscale transfer and physical space transport accelerations*

The convective nonlinearity is responsible for nonlinear turbulence transport through space and nonlinear transfer through scales. We want to separate these two effects and, therefore, decompose the two-point nonlinear acceleration term δa_c into an interscale transfer acceleration a_Π and a physical space transport acceleration $a_\mathcal{T}$ (Hill 2002), i.e. $\delta a_c = a_\Pi + a_\mathcal{T}$ with

$$a_\mathcal{T}(x, r, t) = \tfrac{1}{2}(u^+ + u^-) \cdot \nabla_x \delta u, \quad a_\Pi(x, r, t) = \delta u \cdot \nabla_r \delta u \qquad (3.18a,b)$$

With this decomposition of the nonlinear term, the NSD equation (3.9) reads

$$\frac{\partial \delta \boldsymbol{u}}{\partial t} + \boldsymbol{a}_{\Pi} + \boldsymbol{a}_{\mathcal{T}} = -\frac{1}{\rho}\boldsymbol{\nabla}_{\boldsymbol{x}}\delta p + \delta \boldsymbol{a}_{\nu} + \delta \boldsymbol{f}. \tag{3.19}$$

We note relations $\boldsymbol{a}_{\Pi} = \delta \boldsymbol{a}_C + u_j^+(\partial/\partial x_j^-)\boldsymbol{u}^- - u_j^-(\partial/\partial x_j^+)\boldsymbol{u}^+$ and $\boldsymbol{a}_{\mathcal{T}} = \delta \boldsymbol{a}_C - u_j^+(\partial/\partial x_j^-)\boldsymbol{u}^- + u_j^-(\partial/\partial x_j^+)\boldsymbol{u}^+$ that can be easily used to show that $\langle \boldsymbol{a}_{\Pi}^2 \rangle$ and $\langle \boldsymbol{a}_{\mathcal{T}}^2 \rangle$ tend towards each other as the amplitude of the separation vector $\boldsymbol{r}$ grows above the integral length scale. We report DNS evidence of this tendency below in this paper.

We want to consider the effects of the interscale transfer and interspace transport terms in the solenoidal and irrotational NSD dynamics and we therefore need to break down the NSD equation (3.19) into two equations, one irrotational and one solenoidal. We therefore perform Helmholtz decompositions in centroid space $\boldsymbol{x}$ for a given separation $\boldsymbol{r}$ at time t, for example, $\delta \boldsymbol{q}(\boldsymbol{x}, \boldsymbol{r}, t) = \delta \boldsymbol{q}_{\bar{I}}(\boldsymbol{x}, \boldsymbol{r}, t) + \delta \boldsymbol{q}_{\bar{S}}(\boldsymbol{x}, \boldsymbol{r}, t)$, where $\delta \boldsymbol{q}_{\bar{I}}(\boldsymbol{x}, \boldsymbol{r}, t)$ and $\delta \boldsymbol{q}_{\bar{S}}(\boldsymbol{x}, \boldsymbol{r}, t)$ are, respectively, the irrotational and solenoidal parts in centroid space of $\delta \boldsymbol{q}(\boldsymbol{x}, \boldsymbol{r}, t)$. This decomposition in centroid space differs in general from the difference of the Helmholtz decomposed terms in the NS equations that gives (3.10) and (3.11), but in periodic/homogeneous turbulence $\delta \boldsymbol{q}_I = \delta \boldsymbol{q}_{\bar{I}}$ and $\delta \boldsymbol{q}_S = \delta \boldsymbol{q}_{\bar{S}}$ (see Appendix B). Furthermore, from $\delta \boldsymbol{a}_c = \boldsymbol{a}_{\Pi} + \boldsymbol{a}_{\mathcal{T}}$, immediately follow $\delta \boldsymbol{a}_{c_{\bar{S}}} = \boldsymbol{a}_{\Pi_{\bar{S}}} + \boldsymbol{a}_{\mathcal{T}_{\bar{S}}}$ and $\delta \boldsymbol{a}_{c_{\bar{I}}} = \boldsymbol{a}_{\Pi_{\bar{I}}} + \boldsymbol{a}_{\mathcal{T}_{\bar{I}}}$. Thus, we can rewrite the NSD solenoidal and irrotational equations (3.10) and (3.11) as

$$\boldsymbol{a}_{\Pi_{\bar{I}}} + \boldsymbol{a}_{\mathcal{T}_{\bar{I}}} = \delta \boldsymbol{a}_p, \tag{3.20}$$

$$\delta \boldsymbol{a}_l + \boldsymbol{a}_{\Pi_{\bar{S}}} + \boldsymbol{a}_{\mathcal{T}_{\bar{S}}} = \delta \boldsymbol{a}_{\nu} + \delta \boldsymbol{f}, \tag{3.21}$$

in periodic/homogeneous turbulence.

We emphasize that the interscale transfer term $\boldsymbol{a}_{\Pi_{\bar{S}}}$ is related non-locally in space to two-point vortex stretching and compression terms governing the evolution of vorticity difference $\delta \boldsymbol{\omega}$. This follows from the fact that, as for the Tsinober equations, the NSD solenoidal equation is an integrated vorticity difference equation. We provide mathematical detail on the connection between $\boldsymbol{a}_{\Pi_{\bar{S}}}$ and $\delta \boldsymbol{\omega}$ in Appendix C. This relation between $\boldsymbol{a}_{\Pi_{\bar{S}}}$ and the vorticity difference dynamics provides an instantaneous connection between the interscale momentum dynamics and two-point vorticity stretching and compression dynamics.

Equation (3.20) can also be obtained by integrating the Poisson equation for δp in centroid space similarly to (3.21) that, as already mentioned, can be obtained by integrating the vorticity difference equation in that same space. We use this approach in Appendix C to derive these equations for periodic/homogeneous turbulence but also their generalized form for non-homogeneous turbulence. By deriving the exact equations for $\boldsymbol{a}_{\mathcal{T}_{\bar{I}}}(\boldsymbol{x}, \boldsymbol{r}, t)$ and $\boldsymbol{a}_{\Pi_{\bar{I}}}(\boldsymbol{x}, \boldsymbol{r}, t)$ in Fourier centroid space we show in Appendix B that we have $\boldsymbol{a}_{\mathcal{T}_{\bar{I}}}(\boldsymbol{x}, \boldsymbol{r}, t) = \boldsymbol{a}_{\Pi_{\bar{I}}}(\boldsymbol{x}, \boldsymbol{r}, t)$ in periodic/homogeneous turbulence. This result combined with (3.20) yields

$$\boldsymbol{a}_{\Pi_{\bar{I}}} = \boldsymbol{a}_{\mathcal{T}_{\bar{I}}} = \tfrac{1}{2}\delta \boldsymbol{a}_p = \tfrac{1}{2}\delta \boldsymbol{a}_{cI} \tag{3.22}$$

in periodic/homogeneous turbulence. In figure 4 we plot spatio-temporal averages of $\boldsymbol{r}$-orientation-averaged quantities (3.17) for various acceleration/force terms in the NSD and the Helmholtz decomposed NSD equations and in figure 5 we plot spatio-temporal averages of $\boldsymbol{r}$-orientation-averaged cosines of angles between various two-point acceleration terms in these equations. The overlapping magnitudes in figure 4 and the average alignments in figure 5 confirm (3.22), or rather validate our DNS given that (3.22) is exact.

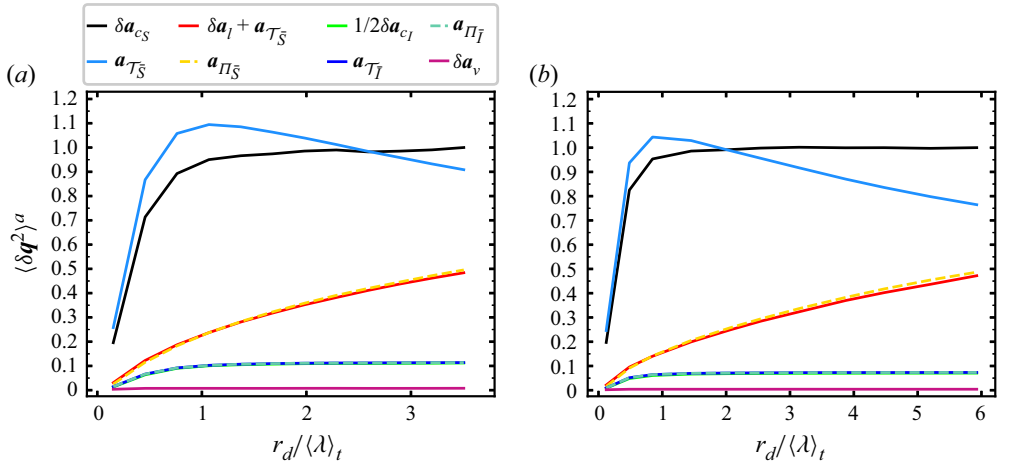

Figure 4. Average magnitudes $\langle \delta q^2 \rangle^a$ of NSD terms present in the irrotational and solenoidal NSD equations (3.21) and (3.22) listed on top of (a). All values have been normalised with $\langle \delta a_{c_S}^2 \rangle^a$ at the largest considered separation r_d. The magnitudes of the terms $(\delta a_l + a_{\mathcal{T}_{\bar{S}}}$ and $a_{\Pi_{\bar{S}}})$ overlap and the magnitudes of the terms $(1/2\delta a_{c_I}, a_{\mathcal{T}_{\bar{I}}}$ and $a_{\Pi_{\bar{I}}})$ also overlap. Results are shown for (a) $\langle Re_\lambda \rangle_t = 112$, (b) $\langle Re_\lambda \rangle_t = 174$.

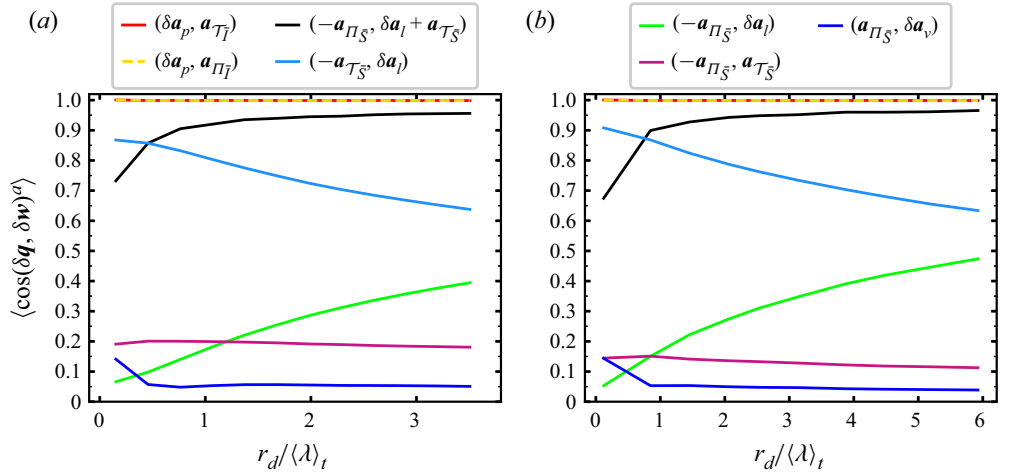

Figure 5. Average alignments of NSD terms $(\delta q, \delta w)$ listed on top of (a,b). The average alignments of $(\delta a_p, a_{\mathcal{T}_{\bar{I}}})$ and $(\delta a_p, a_{\Pi_{\bar{I}}})$ overlap: (a) $\langle Re_\lambda \rangle_t = 112$, (b) $\langle Re_\lambda \rangle_t = 174$.

The computational procedure to calculate the various $\boldsymbol{r}$-orientation-averaged terms in these figures is computationally expensive. To calculate the NSD irrotational and solenoidal parts of the interscale and interspace transport terms at a given time t and separation $\boldsymbol{r}$, we use the pseudo-spectral algorithm of Patterson & Orszag (1971) with one phase shift and spherical truncation. We apply this algorithm to δu_j and $\partial \delta u_i/\partial r_j$ for the interscale transfer and for $(u_j^+ + u_j^-)/2$ and $\partial \delta u_i/\partial x_j$ for the interspace transfer. Hence, we express these vectors/tensors in Fourier space (see (B13)–(B16) in Appendix B) and apply the pseudo-spectral method of Patterson & Orszag (1971) to calculate $\widehat{\boldsymbol{a}_{\mathcal{T}}}(\boldsymbol{k}, \boldsymbol{r}, t)$ and $\widehat{\boldsymbol{a}_{\Pi}}(\boldsymbol{k}, \boldsymbol{r}, t)$ without aliasing errors. We next decompose these fields to irrotational and solenoidal fields with the projection operator and inverse these fields to physical space

to obtain $\boldsymbol{a}_{\Pi_{\bar{S}}}(\boldsymbol{x},\boldsymbol{r},t)$, $\boldsymbol{a}_{\Pi_{\bar{I}}}(\boldsymbol{x},\boldsymbol{r},t)$, $\boldsymbol{a}_{\mathcal{T}_{\bar{S}}}(\boldsymbol{x},\boldsymbol{r},t)$ and $\boldsymbol{a}_{\mathcal{T}_{\bar{I}}}(\boldsymbol{x},\boldsymbol{r},t)$. These fields can then be sampled over $\boldsymbol{x}$ to calculate, e.g. $\boldsymbol{a}^2_{\Pi_{\bar{S}}}(\boldsymbol{x},\boldsymbol{r},t)$ or KHMH terms such as $2\delta\boldsymbol{u}\cdot\boldsymbol{a}_{\Pi_{\bar{S}}}(\boldsymbol{x},\boldsymbol{r},t)$ (see § 3.4). If we assume that the cost of a DNS time step is similar to the cost of the pseudo-spectral method to calculate the NS nonlinear term, the calculation of solenoidal and irrotational interspace and interscale transfers for one t and one $\boldsymbol{r}$ has similar cost to one DNS time step. The total cost of the pseudo-spectral post-processing method is proportional to the total number N_r of separation vectors $\boldsymbol{r}$ that we use in our spherical averaging across scales r_d and to the total number $T_s/\Delta T$ of samples in time (see table 1). With a total number of separation vectors $N_r \sim 10^3$–10^4 and our $T_s/\Delta T$ values, the total cost of the pseudo-spectral post-processing method in terms of DNS time steps is at least one order of magnitude larger than the cost of the DNS itself. This high post-processing cost limits the possible number of grid points in this study. If we estimate the wall time of a 1024^3 simulation to be approximately 10 days, the post-processing would require approximately three to four months.

The NSD solenoidal equation (3.21) describes a balance between the time derivative, solenoidal interscale transfer, solenoidal interspace transport, viscous and forcing terms. From the point we made in the sentence directly following (3.19), we expect $\langle \boldsymbol{a}^2_{\mathcal{T}_{\bar{S}}}\rangle$ and $\langle \boldsymbol{a}^2_{\Pi_{\bar{S}}}\rangle$ to tend to become equal to each other as the amplitude of $\boldsymbol{r}$ tends to values significantly larger than $\langle L\rangle_t$. Figure 4 confirms this trend for the second-order orientation-averaged moments of $\boldsymbol{a}_{\mathcal{T}_{\bar{S}}}$ and $\boldsymbol{a}_{\Pi_{\bar{S}}}$. For brevity, in what follows we refer to such statistics as second-order magnitudes. With decreasing r_d, the magnitudes of $\boldsymbol{a}_{\Pi_{\bar{S}}}$ decrease relative to those of $\boldsymbol{a}_{\mathcal{T}_{\bar{S}}}$. At all scales $r_d \geq \langle\lambda\rangle_t$ the second-order magnitudes of $\boldsymbol{a}_{\mathcal{T}_{\bar{S}}}$ and $\boldsymbol{a}_{\Pi_{\bar{S}}}$ are one order of magnitude larger than those of the viscous term $\delta\boldsymbol{a}_\nu$ and this separation is greater for the larger $\langle Re_\lambda\rangle_t$. The magnitudes of $\delta\boldsymbol{a}_\nu$ are themselves much larger than those of $\delta\boldsymbol{f}$ (not shown in figure 4 for not overloading the figure but see figure 3a1). These observations suggest that the solenoidal NSD equation (3.21) reduces to the approximate

$$\delta\boldsymbol{a}_l + \boldsymbol{a}_{\mathcal{T}_{\bar{S}}} \approx -\boldsymbol{a}_{\Pi_{\bar{S}}}, \tag{3.23}$$

where this equation is understood as typical in terms of second-order magnitudes: i.e. in most regions of the flow for the majority of the time, the removed terms are at least one order of magnitude smaller than the retained terms. (As for the NS dynamics, we do expect dynamically important regions localised in space and time where the dynamics differ from (3.23).) Figure 4 confirms (3.23) in a second-order sense and shows that the relatively rare spatio-temporal events that are neglected when writing (3.23) are indeed present as the second-order statistics do show a very small deviation from (3.23). An additional important observation to be made from figure 4 is that $\delta\boldsymbol{a}_{cs}$ tends to become increasingly dominated by $\boldsymbol{a}_{\mathcal{T}_{\bar{S}}}$ rather than $\boldsymbol{a}_{\Pi_{\bar{S}}}$ as r_d decreases.

Equation (3.23) is the same as (3.12), and similarly to figure 3 that provides support for (3.12), figures 4 and 5 provide strong support for (3.23), in particular for $r_d > \langle\lambda\rangle_t$. It is interesting to note that the average alignment between the left- and right-hand sides of (3.23) lies between 90 % and 100 % (typically 95 %) for $r_d > \langle\lambda\rangle_t$. Whilst this is strong support for approximate (3.23), the fact that the alignment is not 100 % is a reminder of the nature of the approximation, i.e. that relatively rare spatio-temporal events do exist where the viscous and/or driving forces are not negligible.

At length scales $r_d \leq \langle\lambda\rangle_t$, the alignment between $\delta\boldsymbol{a}_l$ and $-\boldsymbol{a}_{\mathcal{T}_{\bar{S}}}$ improves while the alignment between $\delta\boldsymbol{a}_l + \boldsymbol{a}_{\mathcal{T}_{\bar{S}}}$ and $-\boldsymbol{a}_{\Pi_{\bar{S}}}$ worsens with decreasing r_d (see figure 5), presumably because of direct dissipation and diffusion effects, so that $\delta\boldsymbol{a}_l + \boldsymbol{a}_{\mathcal{T}_{\bar{S}}} \approx 0$

becomes a better approximation than (3.23) at $r_d < 0.5\langle\lambda\rangle_t$. This observation is consistent with our parallel observation that the magnitude of $\boldsymbol{a}_{\mathcal{T}_{\bar{S}}}$ increases while the magnitude of $\boldsymbol{a}_{\Pi_{\bar{S}}}$ decreases with decreasing r_d and that $\delta\boldsymbol{a}_{cS}$ in (3.12) tends to be dominated by $\boldsymbol{a}_{\mathcal{T}_{\bar{S}}}$ at the very smallest scales.

On the other end of the spectrum, i.e. as the length scale r_d grows towards $\langle L\rangle_t$, the alignment between $\delta\boldsymbol{a}_l$ and $-\boldsymbol{a}_{\mathcal{T}_{\bar{S}}}$ worsens while the alignment between $\delta\boldsymbol{a}_l$ and $-\boldsymbol{a}_{\Pi_{\bar{S}}}$ improves (see figure 5), both reaching a comparable level of alignment/misalignment that contribute together to keep approximation (3.23) statistically well satisfied with 95 % alignment between $\delta\boldsymbol{a}_l + \boldsymbol{a}_{\mathcal{T}_{\bar{S}}}$ and $-\boldsymbol{a}_{\Pi_{\bar{S}}}$.

The strong anti-alignment between $\boldsymbol{a}_{\mathcal{T}_{\bar{S}}}$ and $\delta\boldsymbol{a}_l$, increasingly so at smaller r_d (see figure 5) expresses the sweeping of the two-point momentum difference $\delta\boldsymbol{u}$ at scales r_d and smaller by the mainly large scale velocity $(\boldsymbol{u}^+ + \boldsymbol{u}^-)/2$. Note that this two-point sweeping differs from anti-alignment between $\delta\boldsymbol{a}_l$ and $\delta\boldsymbol{a}_c$ for two reasons. Firstly, by using the Helmholtz decomposition we have removed the pressure effect embodied in the $\boldsymbol{a}_{c_I}$ contribution to $\boldsymbol{a}_c$ that balances the pressure gradient. This was first understood in Tsinober *et al.* (2001) in a one-point setting and is here extended to a two-point setting. Secondly, $\delta\boldsymbol{a}_{cS}$ is the sum of an interspace transport $\boldsymbol{a}_{\mathcal{T}_{\bar{S}}}$ and an interscale transfer term $\boldsymbol{a}_{\Pi_{\bar{S}}}$ such that the interpretation of two-point sweeping as anti-alignment between $\boldsymbol{a}_{cS}$ and $\boldsymbol{a}_l$ as sweeping cannot be exactly accurate. The advection of $\delta\boldsymbol{u}$ by the large-scale velocity is attributable to $\boldsymbol{a}_{\mathcal{T}_{\bar{S}}}$, and figure 5 shows that the two-point sweeping anti-alignment between $\delta\boldsymbol{a}_l$ and $\boldsymbol{a}_{\mathcal{T}_{\bar{S}}}$ increases with decreasing r_d.

The sweeping anti-alignment between $\delta\boldsymbol{a}_l$ and $\boldsymbol{a}_{\mathcal{T}_{\bar{S}}}$ is by no means perfect even if it reaches about 90 % accuracy at $r_d < \langle\lambda\rangle_t$, as is clear from the similar magnitudes and very strong alignment tendency between $\delta\boldsymbol{a}_l + \boldsymbol{a}_{\mathcal{T}_{\bar{S}}}$ and $-\boldsymbol{a}_{\Pi_{\bar{S}}}$ at scales $|\boldsymbol{r}| \geq \langle\lambda\rangle_t$ (see figures 4 and 5). Note, in passing, that the Lagrangian solenoidal acceleration $\delta\boldsymbol{a}_l + \boldsymbol{a}_{\mathcal{T}_{\bar{S}}}$ and $\boldsymbol{a}_{\Pi_{\bar{S}}}$ are both Galilean invariant. Equation (3.23) may be interpreted to mean that the Lagrangian solenoidal acceleration of $\delta\boldsymbol{u}$ (which is actually solenoidal) moving with the mainly large-scale velocity $(\boldsymbol{u}^+ + \boldsymbol{u}^-)/2$, namely $\delta\boldsymbol{a}_l + \boldsymbol{a}_{\mathcal{T}_{\bar{S}}}$, is evolving in time and space in response to $-\boldsymbol{a}_{\Pi_{\bar{S}}}$: when there is an influx of momentum from larger scales, there is an increase in $\delta\boldsymbol{a}_l + \boldsymbol{a}_{\mathcal{T}_{\bar{S}}}$ and $\delta\boldsymbol{u}$ and it vice versa.

3.4. *From NSD dynamics to KHMH dynamics in homogeneous/periodic turbulence*

The scale-by-scale evolution of $|\delta\boldsymbol{u}|^2$ locally in space and time is governed by a KHMH equation. This makes KHMH equations crucial tools for examining the turbulent energy cascade. The original KHMH equation and the new solenoidal and irrotational KHMH equations that we derive below are simply projections of the corresponding NSD equations onto $2\delta\boldsymbol{u}$. Hence, KHMH dynamics depend on NSD dynamics and the various NSD terms' alignment or non-alignment tendencies with $2\delta\boldsymbol{u}$. In this subsection we present five KHMH results.

By contracting the NSD equation (3.9) with $2\delta\boldsymbol{u}$, one obtains the KHMH equation (Hill 2002; Yasuda & Vassilicos 2018)

$$\frac{\partial}{\partial t}|\delta\boldsymbol{u}|^2 + \frac{u_k^+ + u_k^-}{2}\frac{\partial}{\partial x_k}|\delta\boldsymbol{u}|^2 + \frac{\partial}{\partial r_k}\left(\delta u_k|\delta\boldsymbol{u}|^2\right) = -\frac{2}{\rho}\frac{\partial}{\partial x_k}\left(\delta u_k\delta p\right) + 2\nu\frac{\partial^2}{\partial r_k^2}|\delta\boldsymbol{u}|^2$$
$$+ \frac{\nu}{2}\frac{\partial^2}{\partial x_k^2}|\delta\boldsymbol{u}|^2 - \left[2\nu\left(\frac{\partial u_i^+}{\partial x_k^+}\right)^2 + 2\nu\left(\frac{\partial u_i^-}{\partial x_k^-}\right)^2\right] + 2\delta u_k\delta f_k, \tag{3.24}$$

where no fluid velocity decomposition nor averaging operations have been used. In line with the naming convention of Yasuda & Vassilicos (2018) this equation can be written as

$$\mathcal{A}_t + \mathcal{T} + \Pi = \mathcal{T}_p + \mathcal{D}_{r,\nu} + \mathcal{D}_{x,\nu} - \epsilon + \mathcal{I}, \tag{3.25}$$

where the first, second and third terms on the left-hand sides of (3.24) and (3.25) correspond to each other and so do the first, second, third, fourth and fifth terms on the right-hand sides. Pre-empting notation used further down in this paper, (3.25) is also written as $\mathcal{A} = \mathcal{T}_p + \mathcal{D} + \mathcal{I}$ or $\mathcal{A}_t + \mathcal{A}_c = \mathcal{T}_p + \mathcal{D} + \mathcal{I}$, where $\mathcal{A}_c \equiv \mathcal{T} + \Pi$, $\mathcal{A} \equiv \mathcal{A}_t + \mathcal{A}_c$ and $\mathcal{D} \equiv \mathcal{D}_{r,\nu} + \mathcal{D}_{x,\nu} - \epsilon$.

To examine the KHMH dynamics in terms of irrotational and solenoidal dynamics, we contract the irrotational and solenoidal NSD equations with $2\delta\boldsymbol{u}$ to derive what we refer to as irrotational and solenoidal KHMH equations. Each of the KHMH terms can be subdivided into a contribution from the NSD irrotational part and a contribution from the NSD solenoidal part of the respective term in the NSD equation. A solenoidal KHMH term corresponding to a $\delta\boldsymbol{q}(\boldsymbol{x},\boldsymbol{r},t)$ or $\boldsymbol{q}(\boldsymbol{x},\boldsymbol{r},t)$ term in (3.21) equals $\mathcal{Q}_{\bar{S}} = 2\delta\boldsymbol{u}\cdot\delta\boldsymbol{q}_{\bar{S}}$ or $\mathcal{Q}_{\bar{S}} = 2\delta\boldsymbol{u}\cdot\boldsymbol{q}_{\bar{S}}$, and an irrotational KHMH term corresponding to a $\delta\boldsymbol{q}(\boldsymbol{x},\boldsymbol{r},t)$ or $\boldsymbol{q}(\boldsymbol{x},\boldsymbol{r},t)$ term in (3.22) equals $\mathcal{Q}_{\bar{I}} = 2\delta\boldsymbol{u}\cdot\delta\boldsymbol{q}_{\bar{I}}$ or $\mathcal{Q}_{\bar{I}} = 2\delta\boldsymbol{u}\cdot\boldsymbol{q}_{\bar{I}}$. With $\mathcal{Q} = 2\delta\boldsymbol{u}\cdot\delta\boldsymbol{q}$ or $\mathcal{Q} = 2\delta\boldsymbol{u}\cdot\boldsymbol{q}$, we have $\mathcal{Q} = \mathcal{Q}_{\bar{I}} + \mathcal{Q}_{\bar{S}}$. The irrotational and solenoidal KHMH equations for periodic/homogeneous turbulence follow from (3.21) and (3.22), respectively, and read

$$\mathcal{A}_t + \mathcal{T}_{\bar{S}} + \Pi_{\bar{S}} = \mathcal{D}_{r,\nu} + \mathcal{D}_{x,\nu} - \epsilon + \mathcal{I}, \tag{3.26}$$

$$\Pi_{\bar{I}} = \mathcal{T}_{\bar{I}} = \tfrac{1}{2}\mathcal{T}_p, \tag{3.27}$$

where use has been made of the fact that the velocity and velocity difference fields are solenoidal. These two equations are our first KHMH result.

Space-local changes in time of $|\delta\boldsymbol{u}|^2$, expressed via $\mathcal{A}_t$, are only due to solenoidal KHMH dynamics in (3.26) that include interspace transport, interscale transport, viscous and forcing effects. The irrotational KHMH equation (3.27) formulates how the imposition of incompressibility by the pressure field affects interspace and interscale dynamics and, in turn, energy cascade dynamics. Generalized solenoidal and irrotational KHMH equations also valid for non-periodic/non-homogeneous turbulence are given in Appendix B.

We first consider the spatio-temporal average of these equations in statistically steady forced periodic/homogeneous turbulence. As $\langle\mathcal{T}_p\rangle = 0$, we obtain from (3.27), $\langle\Pi_{\bar{I}}\rangle = \langle\mathcal{T}_{\bar{I}}\rangle = 0$. As $\langle\mathcal{T}_{\bar{S}}\rangle + \langle\mathcal{T}_{\bar{I}}\rangle = \langle\mathcal{T}\rangle = 0$, we have $\langle\mathcal{T}_{\bar{S}}\rangle = 0$, such that the spatio-temporal average of (3.26) reads

$$\langle\Pi\rangle = \langle\Pi_{\bar{S}}\rangle = \langle\mathcal{D}_{r,\nu}\rangle - \langle\epsilon\rangle + \langle\mathcal{I}\rangle. \tag{3.28}$$

If an intermediate inertial subrange of scales $|\boldsymbol{r}|$ can be defined where viscous diffusion and forcing are negligible, (3.28) reduces to $\langle\Pi_{\bar{S}}\rangle \approx -\langle\epsilon\rangle$ in that range. This theoretical conclusion (which is not part of our DNS study) is the backbone of the Kolmogorov (1941*a*,*b*,*c*) theory for a high Reynolds number statistically homogeneous stationary small-scale turbulence with the additional information that the part of the average interscale transfer rate involved in Kolmogorov's equilibrium balance is the solenoidal interscale transfer rate only. This is our second KHMH result. On average, there is a cascade of turbulence energy from large to small scales where the rate of interscale transfer is dominated by two-point vortex stretching (see Appendix C for the relation between the solenoidal interscale transfer and vortex stretching) and is equal to $-\langle\epsilon\rangle$ independently of $|\boldsymbol{r}|$ over a range of scales where viscous diffusion and forcing are negligible.

In this paper we concentrate on the fluctuations around the average picture described by the scale-by-scale equilibrium (3.28) for any Reynolds number. If we subtract the

spatio-temporal average solenoidal KHMH equation (3.28) from the solenoidal KHMH equation (3.26) and use the generic notation $\mathcal{Q}' \equiv \mathcal{Q} - \langle \mathcal{Q} \rangle$, we attain the fluctuating solenoidal KHMH equation

$$\mathcal{A}_t + \mathcal{T}'_{\bar{S}} + \Pi'_{\bar{S}} = \mathcal{D}'_{r,\nu} + \mathcal{D}_{x,\nu} - \epsilon' + \mathcal{I}'. \tag{3.29}$$

This equation governs the fluctuations of the KHMH solenoidal dynamics around its spatio-temporal average. Clearly, if these non-equilibrium fluctuations are large relative to their average values, the average picture expressed by (3.28) is not characteristic of the interscale transfer dynamics. We now study the KHMH fluctuations in statistically stationary periodic/homogeneous turbulence on the basis of (3.27) and (3.29). Concerning (3.27), note that $\Pi'_{\bar{I}} = \Pi_{\bar{I}}$, $\mathcal{T}'_{\bar{I}} = \mathcal{T}_{\bar{I}}$ and $\mathcal{T}'_{\bar{p}} = \mathcal{T}_{\bar{p}}$.

We start by determining the relative fluctuation magnitudes of the spatio-temporal fluctuations of each term in the KHMH equations (3.27) and (3.29). These relative fluctuation magnitudes can emulate those of respective terms in the NSD equations under the following sufficient conditions: (i) the fluctuations are so intense that they dwarf averages, so that $\langle (\mathcal{Q}\prime)^2 \rangle \approx \langle \mathcal{Q}^2 \rangle$; (ii) the mean square of any KHMH term $\mathcal{Q} = 2\delta \boldsymbol{u} \cdot \delta \boldsymbol{q}$ corresponding to a NSD term $\delta \boldsymbol{q}(\boldsymbol{x}, \boldsymbol{r}, t)$ (equivalently $\mathcal{Q} = 2\delta \boldsymbol{u} \cdot \boldsymbol{q}$ corresponding to $\boldsymbol{q}(\boldsymbol{x}, \boldsymbol{r}, t)$) can be approximated as

$$\langle \mathcal{Q}^2 \rangle(\boldsymbol{r}) \approx 4 \langle |\delta \boldsymbol{u}|^2 \rangle \langle |\delta \boldsymbol{q}|^2 \rangle \langle \cos^2(\theta_q) \rangle, \tag{3.30}$$

where the approximate equality results from a degree of decorrelation and θ_q is the angle between $\delta \boldsymbol{q}(\boldsymbol{x}, \boldsymbol{r}, t)$ (or $\boldsymbol{q}(\boldsymbol{x}, \boldsymbol{r}, t)$) and $\delta \boldsymbol{u}(\boldsymbol{x}, \boldsymbol{r}, t)$; (iii) $\langle \cos^2(\theta_q) \rangle$ is not very sensitive to the choice of NSD term $\delta \boldsymbol{q}$ (or $\boldsymbol{q}$). Under these conditions, we get

$$\frac{\langle (2\delta \boldsymbol{u} \cdot \delta \boldsymbol{q})^2 \rangle(\boldsymbol{r})}{\langle (2\delta \boldsymbol{u} \cdot \delta \boldsymbol{w})^2 \rangle(\boldsymbol{r})} \approx \frac{\langle |\delta \boldsymbol{u}|^2 \rangle \langle |\delta \boldsymbol{q}|^2 \rangle \langle \cos^2(\theta_q) \rangle(\boldsymbol{r})}{\langle |\delta \boldsymbol{u}|^2 \rangle \langle |\delta \boldsymbol{w}|^2 \rangle \langle \cos^2(\theta_w) \rangle(\boldsymbol{r})} \approx \frac{\langle |\delta \boldsymbol{q}|^2 \rangle(\boldsymbol{r})}{\langle |\delta \boldsymbol{w}|^2 \rangle(\boldsymbol{r})}, \tag{3.31}$$

which means that KHMH relative fluctuation magnitudes and NSD relative fluctuation magnitudes are approximately identical. The first approximate equality in (3.31) follows directly from (3.30) and the second approximate equality follows from hypothesis (iii) that $\cos^2(\theta_q)$ and $\cos^2(\theta_w)$ are about equal.

We test hypothesis (i) by comparing the plots in figure 6(*a*1,*b*1) with those in figure 6(*a*2,*b*2). Figure 6(*a*1,*b*1) shows average magnitudes of KHMH spatio-temporal fluctuations for terms with non-zero spatio-temporal averages. Comparing with figure 6(*a*2,*b*2), we find that $\langle (\mathcal{Q}\prime)^2 \rangle^a \approx \langle \mathcal{Q}^2 \rangle^a$, i.e. hypothesis (i), for all four terms plotted in figure 6(*a*1,*b*1) at all length scales r_d considered. Note that this does not hold for $\mathcal{D}'_{r,\nu}$ and $\mathcal{I}'$ that are the only KHMH fluctuations such that $\sqrt{\langle (\mathcal{Q}\prime)^2 \rangle^a}/\langle \epsilon \rangle^a$ is smaller (in fact significantly smaller) than 1 at all scales. Figure 6 also makes it clear that the magnitudes of the fluctuations of all other KHMH terms (solenoidal and irrotational) are much higher than those of the turbulence dissipation at all scales $r_d > 0.5\langle \lambda \rangle_t$, and more so for the higher of the two Reynolds numbers. For scales $r_d \geq \langle \lambda \rangle_t$, the largest average fluctuating magnitudes are those of $\mathcal{A}'_c$, followed closely by $\mathcal{A}_t$ and $\mathcal{T}'_{\bar{S}}$. Next come the magnitudes of $\Pi'_{\bar{S}}$ and $\mathcal{A}_t + \mathcal{T}'_{\bar{S}}$. Thereafter follow the irrotational terms $\Pi_{\bar{I}} = \mathcal{T}_{\bar{I}}$ $(= 0.5\mathcal{T}_p)$ and finally the viscous, dissipative and forcing terms $\mathcal{D}'$, ϵ' and $\mathcal{I}'$ in that order. This order of fluctuations is our third KHMH result. An average description of the interscale turbulent energy transfer dynamics in terms of its spatio-temporal average cannot, therefore, be accurate. In order to characterize these dynamics, attention must be directed at most if not all KHMH term fluctuations, and in fact to much more than just the turbulence dissipation fluctuations given that they are among the weakest.

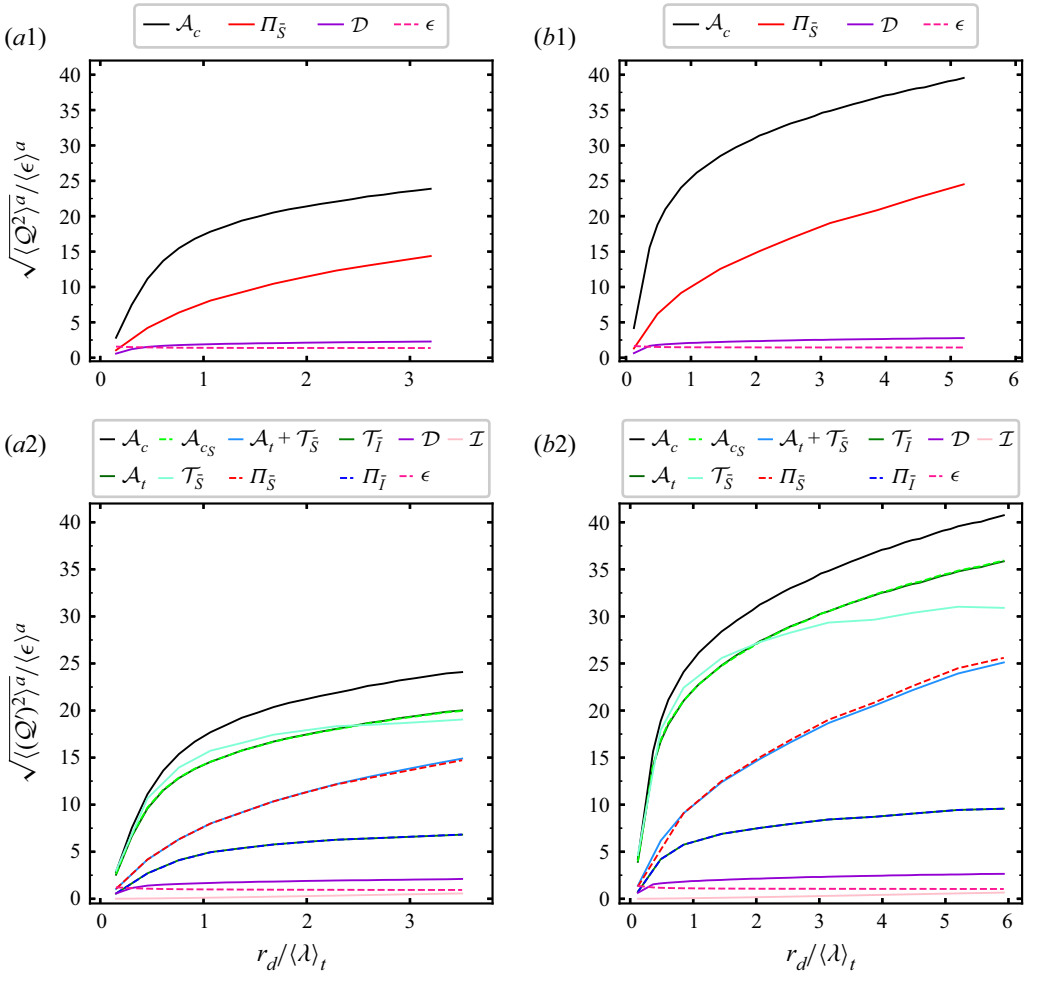

Figure 6. (*a*1,*b*1) The KHMH average square magnitudes $\langle \mathcal{Q}^2 \rangle^a$ and (*a*2,*b*2) KHMH average square fluctuating magnitudes $\langle (\mathcal{Q}')^2 \rangle^a$, where $\mathcal{Q}' = \mathcal{Q} - \langle \mathcal{Q} \rangle$, for the KHMH terms $\mathcal{Q}$ listed above the figures and introduced in the third and fourth paragraphs of § 3.4. All entries are normalised with $\langle \epsilon \rangle^a$ (see (3.24) and (3.25)). The following pairs of KHMH terms have overlapping magnitudes in (*a*2,*b*2): $\mathcal{A}_t$ and $\mathcal{A}_{cS}$; $\mathcal{A}_t + \mathcal{T}_{\bar{S}}$ and $\Pi_{\bar{S}}$; $\mathcal{T}_{\bar{I}}$ and $\Pi_{\bar{I}}$. Results are shown for (*a*1,*a*2) $\langle Re_\lambda \rangle_t = 112$, (*b*1,*b*2) $\langle Re_\lambda \rangle_t = 174$.

Next, we test hypothesis (ii) by testing the validity of (3.30) and hypothesis (iii) concerning approximately similar $\cos^2(\theta_q)$ behaviour for different KHMH terms. In figure 7(*a*1,*b*1) we plot ratios of the right-hand sides to left-hand sides of (3.30) and see that (3.30) is not valid, but that it is nevertheless about 65 % to 98 % accurate for $r_d \geq \langle \lambda \rangle_t$. Note that (3.30) might be sufficient but that it is by no means necessary for the leftmost and rightmost sides of (3.31) to approximately balance. In those cases where the variations between the ratios plotted in figure 7(*a*1,*b*1) are not too large and the assumption of approximately similar $\cos^2(\theta_q)$ for different KHMH terms more or less holds, the leftmost and rightmost sides of (3.31) can approximately balance.

Incidentally, figure 7(*a*2,*b*2) also shows that the angles θ_q are not random but that they are more likely to be small rather than large in an approximately similar way for all important NSD terms: $\cos^2(\theta_q)$ ranges between about 0.28 and 0.36 for all NSD terms

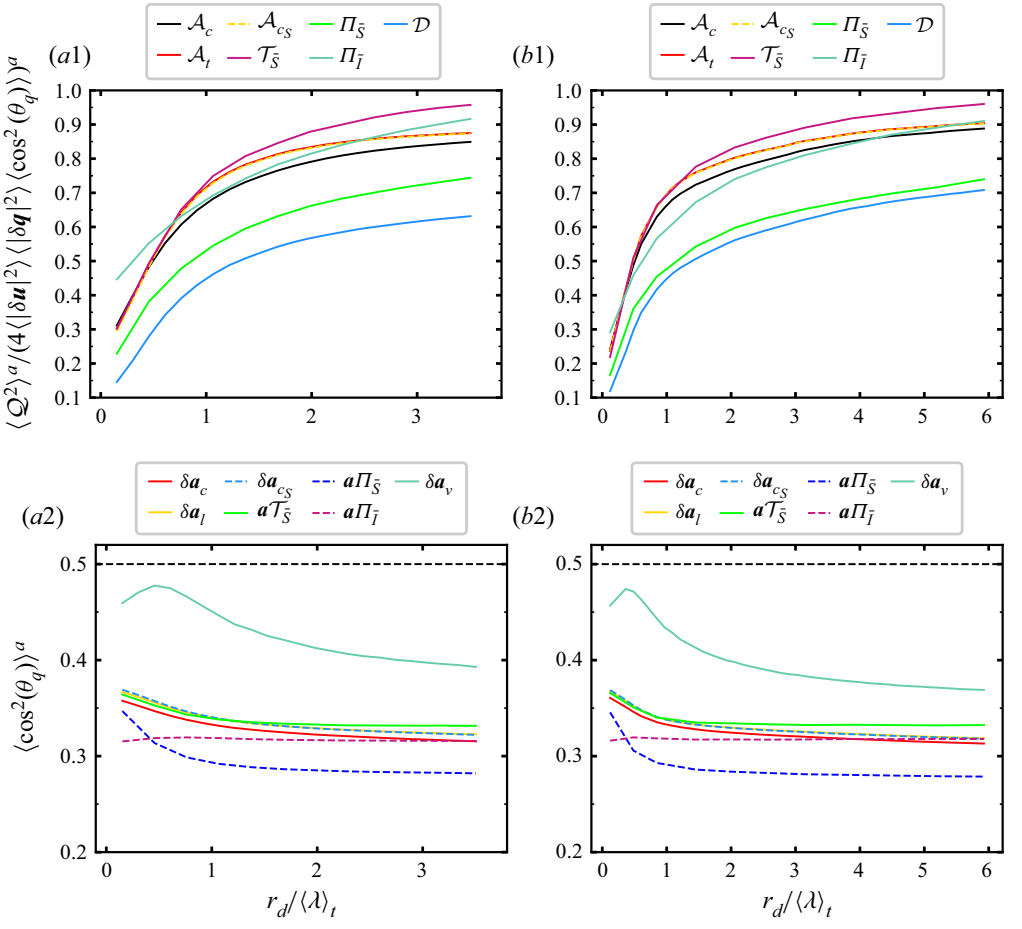

Figure 7. Test of the assumptions (ii) and (iii) in the seventh paragraph of § 3.4 related to relations (3.30) and (3.31) connecting NSD and KHMH relative magnitudes. (*a*1,*b*1) Test of assumption (ii) by taking the ratio of the left-hand and right-hand sides of (3.30) for the KHMH terms $\mathcal{Q}$ listed above the figures. (*a*2,*b*2) Test of assumption (iii) used in (3.31) by comparing the behaviour of $\langle\cos^2(\theta_q)\rangle^a$ for the various NSD terms listed above the figures. The black horizontal line 0.5 corresponds to the value of $\langle\cos^2(\theta_q)\rangle$ if θ_q is uniformly distributed. Results are shown for (*a*1,*a*2) $\langle Re_\lambda\rangle_t = 112$, (*b*1,*b*2) $\langle Re_\lambda\rangle_t = 174$.

(except the viscous acceleration difference and the viscous force difference) at all scales r_d. These values are much smaller than 0.5, the value that $\cos^2(\theta_q)$ would have taken if the angles θ_q were random. There is therefore an alignment tendency between $\delta\boldsymbol{u}$ and NSD terms that is similar for all the important NSD terms, thereby allowing the balance between the leftmost (ratio of KHMH terms) and the rightmost (ratio of NSD terms) sides of (3.31) to approximately hold as seen by comparing the plots (*a*1)-(*b*1) (mean square NSD terms) with the plots (*a*2)-(*b*2) (mean square KHMH terms) in figure 8. (Note that the viscous term is bounded from above, $\langle\mathcal{D}^2\rangle(\boldsymbol{r}) \leq 4\langle|\delta\boldsymbol{u}|^2|\delta\boldsymbol{a}_\nu|^2\rangle$, which indicates limited magnitudes compared with the irrotational and dominant solenoidal terms because of the limited magnitude of $\langle\delta\boldsymbol{a}_\nu^2\rangle$. The limited fluctuations of the viscous terms are clearly seen in figure 6.)

Figure 8 does indeed confirm the close correspondence between NSD and KHMH statistics that is a significant step further from the correspondence reported earlier in this

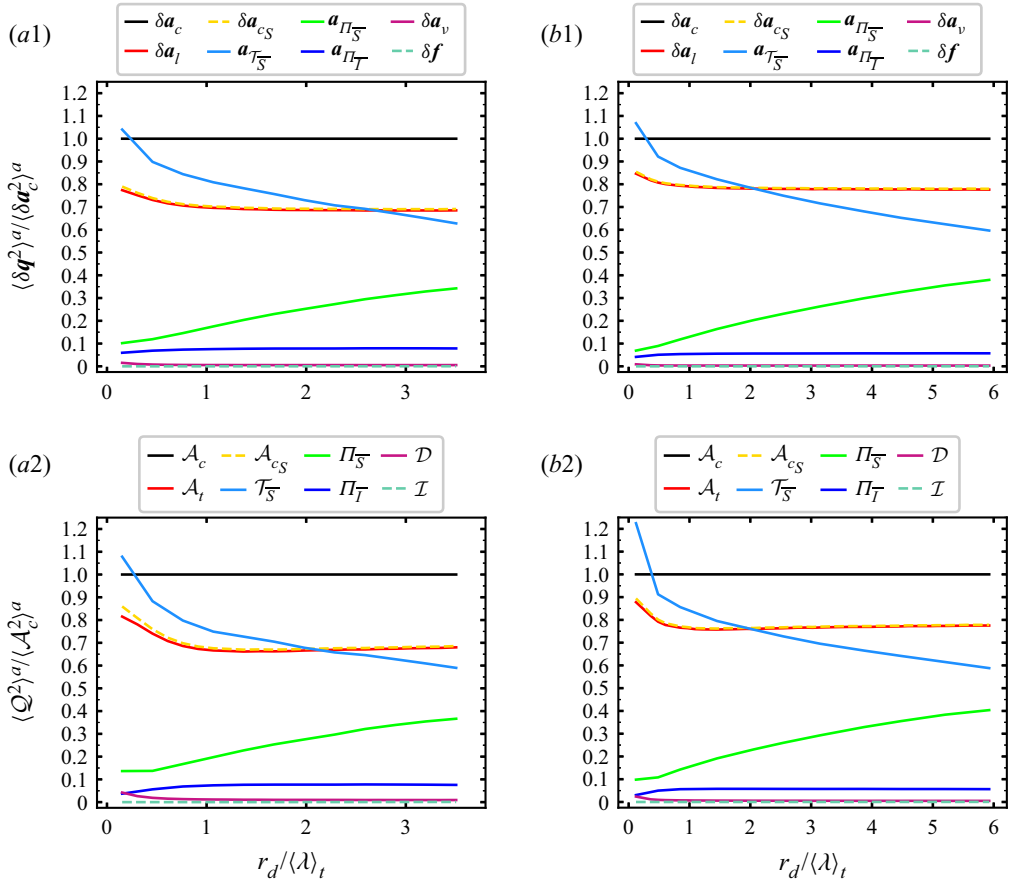

Figure 8. The NSD and KHMH relative average square magnitudes (which should be similar on the basis of (3.31)) for the terms listed above the figures: (*a*1) NSD and (*a*2) KHMH for $\langle Re_\lambda \rangle_t = 112$, (*b*1) NSD and (*b*2) KHMH for $\langle Re_\lambda \rangle_t = 174$.

paper between NS and NSD statistics. We can therefore use the approximate NSD relation (3.23) to deduce the following approximate KHMH relation:

$$\mathcal{A}_t + \mathcal{T}_{\bar{S}} + \Pi'_{\bar{S}} \approx 0, \tag{3.32}$$

understood in the sense that it holds in the majority of the domain for the majority of the time but that there surely exist relatively rare events within the flow where this approximate KHMH relation is violated.

This approximate equation $\mathcal{A}_t + \mathcal{T}_{\bar{S}} + \Pi'_{\bar{S}} \approx 0$ can be considered to be our fourth KHMH result. It is consistent with the order of fluctuation magnitudes in figure 8 that shows, in agreement with the NSD–KHMH correspondence just established, that the largest fluctuating magnitudes are those of $\mathcal{A}_c$, followed by the fluctuating magnitudes of $\mathcal{T}_{\bar{S}}$, $\mathcal{A}_t$ and $\mathcal{A}_{cS}$ ($\mathcal{A}_{cS} = \mathcal{T}_{\bar{S}} + \Pi_{\bar{S}}$). Note though that there is a crossover at about $r_d \approx 2\langle \lambda \rangle_t$ for both Reynolds numbers considered here between the fluctuation magnitudes of $\mathcal{T}_{\bar{S}}$ and those of $\mathcal{A}_t$ and $\mathcal{A}_{cS}$ that are about equal to each other in agreement with (3.32).

The fluctuation magnitudes of $\Pi_{\bar{S}}$ and $\Pi_{\bar{I}}$ are both smaller than those just mentioned, and those of $\Pi_{\bar{I}}$ are significantly smaller than those of $\Pi_{\bar{S}}$. Even smaller are the fluctuation

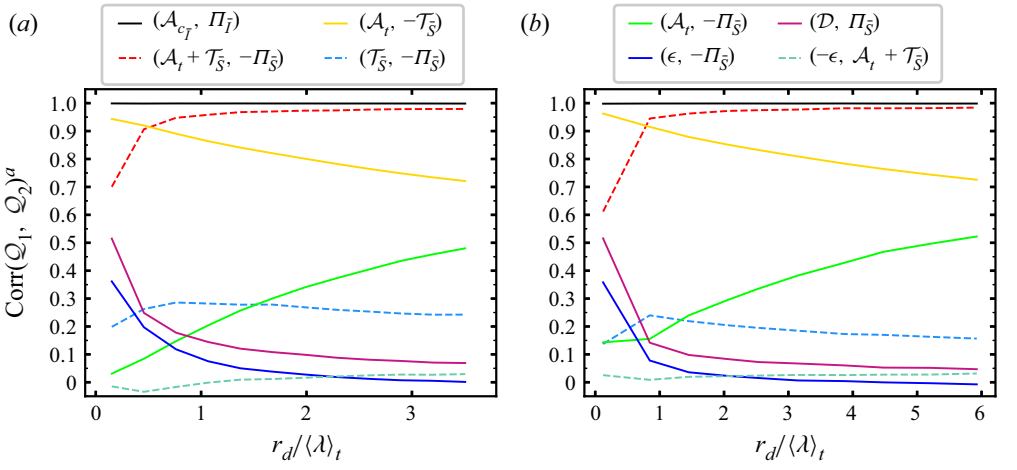

Figure 9. Spherically averaged correlation coefficients between KHMH terms $(\mathcal{Q}_1, \mathcal{Q}_2)$ listed above the plots (*a*,*b*). They are plotted as functions of scale r_d. Results are shown for (*a*) $\langle Re_\lambda\rangle_t = 112$, (*b*) $\langle Re_\lambda\rangle_t = 174$.

magnitudes of $\mathcal{D}$ and $\mathcal{I}$, in that order. In agreement with (3.16), our third and fourth KHMH conclusions incorporate

$$\langle \mathcal{A}_t^2\rangle \approx \langle \mathcal{A}_{cS}^2\rangle \gg \langle \mathcal{T}_p^2\rangle = 4\langle \Pi_{\tilde{I}}^2\rangle = 4\langle \mathcal{T}_{\tilde{I}}^2\rangle = \langle \mathcal{A}_{cI}^2\rangle \gg \langle \mathcal{D}^2\rangle \gg \langle \mathcal{I}^2\rangle, \tag{3.33}$$

where $\mathcal{A}_{cI} = \mathcal{T}_{\tilde{I}} + \Pi_{\tilde{I}}$.

An additional significant observation from figure 8 that we can count as our fifth KHMH result is that, as r_d decreases towards about $0.5\langle\lambda\rangle_t$, the fluctuation magnitude of $\mathcal{A}_{cS} = \mathcal{T}_{\tilde{S}} + \Pi_{\tilde{S}}$ remains about constant but that of $\mathcal{T}_{\tilde{S}}$ increases while that of $\Pi_{\tilde{S}}$ decreases. (At scale r_d smaller than $0.5\langle\lambda\rangle_t$, the fluctuation magnitudes of both $\mathcal{A}_{cS}$ and $\mathcal{T}_{\tilde{S}}$ increase with diminishing r_d whereas those of $\Pi_{\tilde{S}}$ remain about constant.) The convective nonlinearity is increasingly of the spatial transport type and diminishingly of the interscale transfer type as the two-point separation length decreases.

We now consider correlations between different intermediate and large-scale fluctuating KHMH terms in light of (3.27) and (3.32).

4. Fluctuating KHMH dynamics in homogeneous/periodic turbulence

4.1. *Correlations*

We start this section by assessing the existence or non-existence of local (in space and time) equilibrium between interscale transfer and dissipation at some intermediate scales. In figure 9 we plot correlations between various KHMH terms. In particular, this figure shows that the correlation coefficient between $\Pi'_{\tilde{S}}$ and $-\epsilon'$ lies well below 0.1 for all scales $r_d \geq \langle\lambda\rangle_t$. The scatter plots of these quantities in figure 10 confirm the absence of a local relation between interscale transfer rate and dissipation rate. For example, for a given local/instantaneous dissipation fluctuation, the corresponding local/instantaneous interscale transfer rate fluctuation can be close to equally positive or negative. There is no local equilibrium between these quantities as they fluctuate at scales $r_d \geq \langle\lambda\rangle_t$. Such a correlation should of course not necessarily be expected. However, as r_d decreases below $\langle\lambda\rangle_t$, the correlations between $\Pi'_{\tilde{S}}$ and either $-\epsilon'$ or $\mathcal{D}'$ increase up to values between about 0.3 and about 0.5. This increased correlation may suggest a feeble tendency towards local/instantaneous equilibrium between interscale transfer rate and dissipation rate at

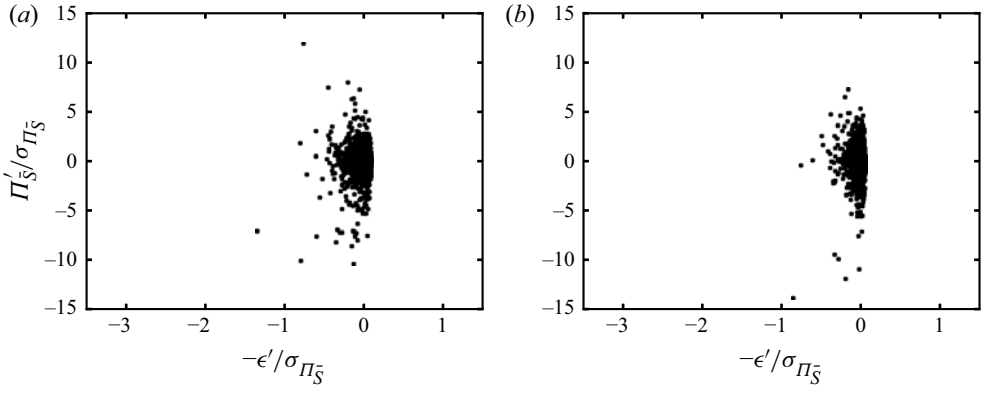

Figure 10. Scatter plots of $\Pi'_{\bar{S}}$ and ϵ' at random orientations $\boldsymbol{r}$ with $r_d/\langle\lambda\rangle_t = (1.45, 3.1)$ for (a,b), $\sigma_{\Pi_{\bar{S}}}$ is the standard deviation of $\Pi_{\bar{S}}$ and $\langle Re_\lambda\rangle_t = 174$.

scales $r_d < \langle\lambda\rangle_t$. However, these scales are strongly affected by direct viscous processes and can therefore not be inertial range scales.

Following the question of local/instantaneous equilibrium, we now look for local/instantaneous sweeping. Figure 9 shows strong anti-correlation between $\mathcal{A}_t$ and $\mathcal{T}_{\bar{S}}$, increasingly so as r_d decreases from large to small scales. Along with the fifth KHMH result at the end of the previous section (that the fluctuation magnitudes of $\mathcal{A}_t$ and $\mathcal{T}_{\bar{S}}$ become increasingly comparable as r_d decreases), this anti-correlation tendency suggests a tendency towards $\mathcal{A}_t + \mathcal{T}_{\bar{S}} \approx 0$ at decreasing scales in agreement with the concept of two-point sweeping introduced in § 3.2. In other words, the sweeping of $|\delta\boldsymbol{u}|^2$ by the mainly large-scale advection velocity $(\boldsymbol{u}^+ + \boldsymbol{u}^-)/2$ becomes increasingly strong with decreasing r_d. The scatter plots of $\mathcal{A}_t$ and $\mathcal{T}_{\bar{S}}$ in figure 11 make this local/instantaneous two-point sweeping tendency with decreasing r_d very evident, but also indicate that significant values of positive or negative $\Pi_{\bar{S}}$ can cause increasing deviations from $\mathcal{A}_t + \mathcal{T}_{\bar{S}} \approx 0$ as r_d increases. Note that $\mathcal{A}_t + \mathcal{T}_{\bar{S}} + \Pi_{\bar{S}} \approx 0$ as indicated by the correlation coefficients in figure 9 between $\mathcal{A}_t + \mathcal{T}_{\bar{S}}$ and $-\Pi_{\bar{S}}$ (which exceed 0.95 for $r_d \geq \langle\lambda\rangle_t$ at our Reynolds numbers) and by their overlapping fluctuation magnitudes in figure 6(*a*2,*b*2). The fluctuations of $\Pi_{\bar{S}}$ increase in magnitude as r_d increases and so do high values of $\Pi_{\bar{S}}$ too. The scatter plots in figure 11 highlight how the 5 % most negative $\Pi_{\bar{S}}$ events (values of $\Pi_{\bar{S}}$ for which the probability that $\Pi_{\bar{S}}$ is smaller than a negative value $\Pi_{\bar{S}_{0.05}}$ is 0.05) and the 5 % most positive $\Pi_{\bar{S}}$ events (values of $\Pi_{\bar{S}}$ for which the probability that $\Pi_{\bar{S}}$ is larger than a positive value $\Pi_{\bar{S}_{0.95}}$ is also 0.05) cause significant deviations from 'perfect sweeping' $\mathcal{A}_t = -\mathcal{T}_{\bar{S}}$, increasingly so for increasing r_d, in agreement with $\mathcal{A}_t + \mathcal{T}_{\bar{S}} + \Pi_{\bar{S}} \approx 0$.

The scatter plots in figure 12 show that it is only in relatively rare circumstances that $\mathcal{A}_t + \mathcal{T}_{\bar{S}} + \Pi_{\bar{S}} \approx 0$ is significantly inaccurate for scales $r_d \geq \langle\lambda\rangle_t$. Similarly to NSD dynamics, $\mathcal{A}_t + \mathcal{T}_{\bar{S}}$ can be viewed as a Lagrangian time rate of change of $|\delta\boldsymbol{u}|^2$ moving with $(\boldsymbol{u}^+ + \boldsymbol{u}^-)/2$. As more than average $|\delta\boldsymbol{u}|^2$ is cascaded from larger to smaller scales at a particular location ($\Pi'_{\bar{S}} < 0$), $\mathcal{A}_t + \mathcal{T}_{\bar{S}}$ increases; and as more than average $|\delta\boldsymbol{u}|^2$ is inverse cascaded from smaller to larger scales ($\Pi'_{\bar{S}} > 0$), $\mathcal{A}_t + \mathcal{T}_{\bar{S}}$ decreases. Here $\Pi'_{\bar{S}}$ is to a large extent determined by $\boldsymbol{a}_{\Pi_{\bar{S}}}$ that, as we show in Appendix C, is a non-local function in space of the vortex stretching and compression dynamics determining the two-point vorticity difference $\delta\boldsymbol{\omega}$.

A fairly complete way to summarise the details of the balance $\mathcal{A}_t + \mathcal{T}_{\bar{S}} + \Pi_{\bar{S}} \approx 0$ at scales $r_d \geq \langle\lambda\rangle_t$ is by noting that, as r_d decreases towards $\langle\lambda\rangle_t$, (i) the fluctuation magnitude

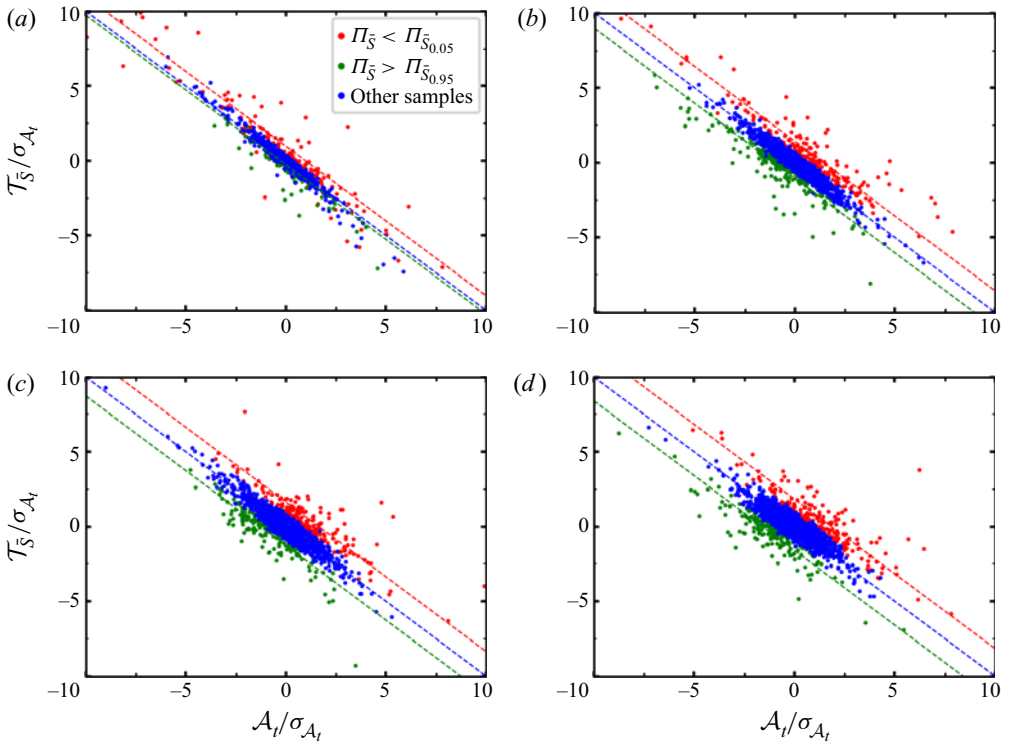

Figure 11. Scatter plots of $\mathcal{A}_t$ and $\mathcal{T}_{\bar{S}}$ at random orientations $\boldsymbol{r}$ normalised by $\sigma_{\mathcal{A}_t}$ and $\sigma_{\mathcal{T}_{\bar{S}}}$, their respective standard deviations. Here $\Pi_{\bar{S}_{0.05}}$ is the value of $\Pi_{\bar{S}}$ at the respective r_d for which 5 % of the samples are more negative than $\Pi_{\bar{S}_{0.05}}$ and $\Pi_{\bar{S}_{0.95}}$ is the value of $\Pi_{\bar{S}}$ for which 95 % of the samples are more positive than $\Pi_{\bar{S}_{0.95}}$. The events $\Pi_{\bar{S}} < \Pi_{\bar{S}_{0.05}}$ and $\Pi_{\bar{S}} > \Pi_{\bar{S}_{0.95}}$ are marked in red and green, respectively, while the remaining events are marked in blue. The red line marks $\mathcal{A}_t = -\mathcal{T}_{\bar{S}} - \langle \Pi_{\bar{S}} | \Pi_{\bar{S}} < \Pi_{\bar{S}_{0.05}} \rangle$, where $\langle \Pi_{\bar{S}} | \Pi_{\bar{S}} < \Pi_{\bar{S}_{0.05}} \rangle$ is the average value of $\Pi_{\bar{S}}$ conditioned on $\Pi_{\bar{S}} < \Pi_{\bar{S}_{0.05}}$. The green line marks $\mathcal{A}_t = -\mathcal{T}_{\bar{S}} - \langle \Pi_{\bar{S}} | \Pi_{\bar{S}} > \Pi_{\bar{S}_{0.95}} \rangle$ and the blue line marks $\mathcal{A}_t = -\mathcal{T}_{\bar{S}}$ (with all terms appropriately normalised with $\sigma_{\mathcal{A}_t}$ and $\sigma_{\mathcal{T}_{\bar{S}}}$). Here $r_d/\langle\lambda\rangle_t = (0.12, 1.45, 3.1, 5.2)$ for (*a–d*) and $\langle Re_\lambda \rangle_t = 174$.

of $\mathcal{T}_{\bar{S}}$ tends to become comparable to that of $\mathcal{A}_t$ while that of $\Pi_{\bar{S}}$ decreases by comparison, (ii) the correlation coefficient between $\mathcal{A}_t$ and $-\mathcal{T}_{\bar{S}}$ increases towards 0.9, and also (iii) (not mentioned till now but evident in figure 9) the correlation coefficient between $\mathcal{A}_t$ and $-\Pi_{\bar{S}}$ decreases towards values below 0.2.

4.2. *Conditional correlations*

At scales r_d below $\langle\lambda\rangle_t$, the relation $\mathcal{A}_t + \mathcal{T}_{\bar{S}} + \Pi_{\bar{S}} \approx 0$ becomes less accurate as the correlation coefficient between $\mathcal{A}_t + \mathcal{T}_{\bar{S}}$ and $-\Pi_{\bar{S}}$ drops from 0.95 to 0.7 with decreasing r_d, reflecting the increase of correlation between ϵ and $-\Pi_{\bar{S}}$ and the even higher increase towards values close to 0.5 of the correlation coefficient between $\mathcal{D}$ and $\Pi_{\bar{S}}$. This increase of correlation appears to reflect the impact of relatively rare yet intense local/instantaneous occurrences of interscale transfer rate as shown in figure 13 where we plot correlations conditional on relatively rare interscale events where the magnitudes of the spherically averaged interscale transfer rates are higher than 95 % of all interscale transfer rates of same sign (positive for backward and negative for forward transfer) in our overall spatio-temporal sample. This impact is highest at scales smaller than $\langle\lambda\rangle_t$ where the

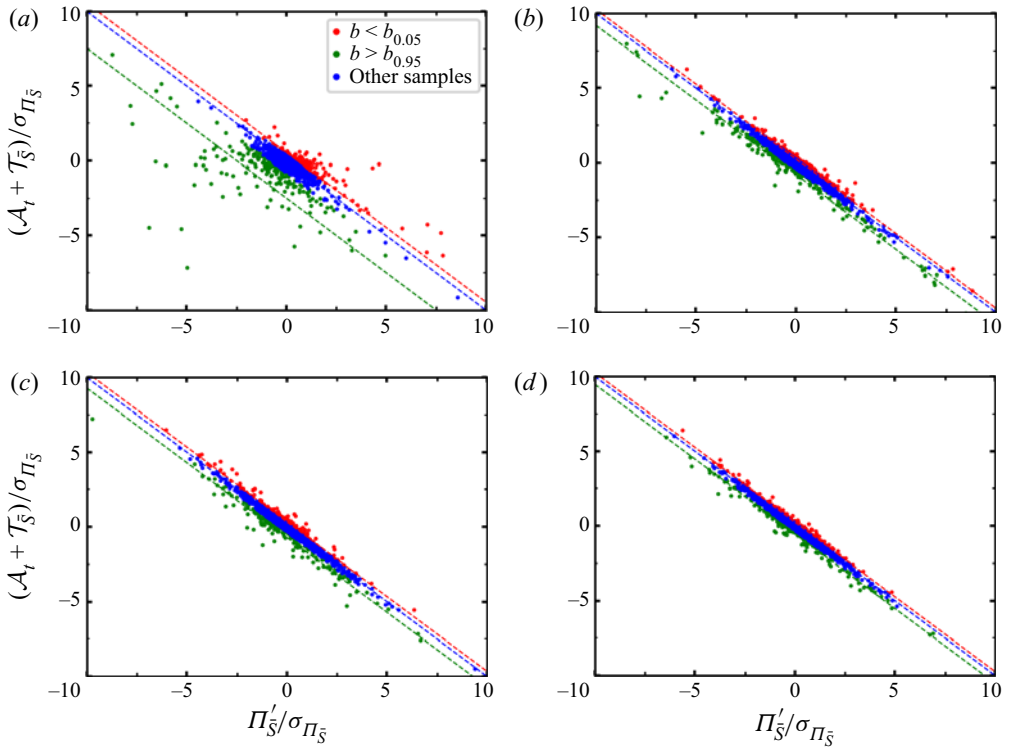

Figure 12. Scatter plots of $\mathcal{A}_t + \mathcal{T}_{\bar{S}}$ and $\Pi'_{\bar{S}}$ at random orientations $\boldsymbol{r}$. The residual $-b \equiv \mathcal{A}_t + \mathcal{T}_{\bar{S}} + \Pi'_{\bar{S}}$ and the values $b_{0.05}$ and $b_{0.95}$ are defined analogously as for $\Pi_{\bar{S}_{0.05}}$ and $\Pi_{\bar{S}_{0.95}}$ in the previous figure. The events $b < b_{0.05}$ and $b > b_{0.95}$ are marked in red and green, respectively, while the remaining events are marked in blue. The red line marks $\mathcal{A}_t + \mathcal{T}_{\bar{S}} = -\Pi'_{\bar{S}} - \langle b|b < b_{0.05}\rangle$, the green line $\mathcal{A}_t + \mathcal{T}_{\bar{S}} = -\Pi'_{\bar{S}} - \langle b|b > b_{0.95}\rangle$ and the blue line $\mathcal{A}_t + \mathcal{T}_{\bar{S}} = -\Pi'_{\bar{S}}$ (with all terms appropriately normalised with $\sigma_{\Pi_{\bar{S}}}$). Here $r_d/\langle\lambda\rangle_t = (0.12, 1.45, 3.1, 5.2)$ for (a, b, c, d) and $\langle Re_\lambda\rangle_t = 174$.

correlation coefficient conditioned on intense forward or backward interscale transfer rate events of $\pm\Pi_{\bar{S}}$ and either ϵ or $\mathcal{D}$ can be as high as 0.7 ($+\Pi_{\bar{S}}$ in the case of backward events and $-\Pi_{\bar{S}}$ in the case of forward events that causes significantly higher correlations between $\mathcal{A}_t + \mathcal{T}_{\bar{S}}$ and either $-\epsilon$ or $\mathcal{D}$ in the case of backward events than in the case of forward events as seen in figure 13). However, the impact of such relatively rare events is also manifest at scales larger than $\langle\lambda\rangle_t$ (see figure 13) where the conditioned correlation coefficient is significantly higher than the unconditioned one in figure 9. Interestingly, conditioning on these relatively rare events does not change the correlation coefficients of $\mathcal{A}_t + \mathcal{T}_{\bar{S}}$ with $-\Pi'_{\bar{S}}$ except at scales r_d smaller than $\langle\lambda\rangle_t$ where, consistently with the increased conditioned correlations between $-\Pi_{\bar{S}}$ and $\mathcal{D}$, they are smaller than the unconditional correlation coefficients of $\mathcal{A}_t + \mathcal{T}_{\bar{S}}$ with $-\Pi'_{\bar{S}}$, particularly at relatively rare forward interscale events where this conditional correlation drops to values close to 0.3 at scales well below $\langle\lambda\rangle_t$.

Given that our relatively rare intense interscale transfer rates can be the seat of some correlation between $\Pi_{\bar{S}}$ and either $-\epsilon$ or $\mathcal{D}$ particularly for $r_d < \langle\lambda\rangle_t$, and given that $\mathcal{A}_t + \mathcal{T}_{\bar{S}} \approx 0$ is a good approximation at scales smaller than $\langle\lambda\rangle_t$, do we have approximate two-point sweeping and approximate equilibrium $\Pi_{\bar{S}} \approx \mathcal{D}$ if we condition on relatively rare forward or backward interscale transfer rate events? In fact the conditional

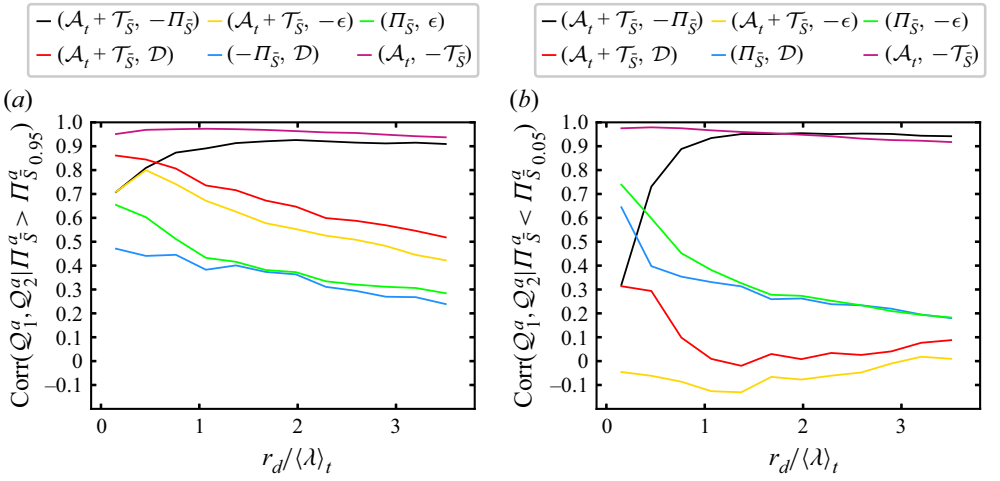

Figure 13. (*a*) Correlation coefficients among the 5 % strongest spherically averaged backward interscale transfer events $\Pi_{\bar{S}}^a > \Pi_{\bar{S}_{0.95}}^a$ for KHMH terms $(\mathcal{Q}_1^a, \mathcal{Q}_2^a)$ listed on top of the figure. (*b*) Correlation coefficients among the 5 % strongest spherically averaged forward interscale transfer events $\Pi_{\bar{S}}^a < \Pi_{\bar{S}_{0.05}}^a$ for KHMH terms $(\mathcal{Q}_1^a, \mathcal{Q}_2^a)$ listed on top of the figure. Here $\langle Re_\lambda\rangle_t = 112$. (Corresponding plots for $\langle Re_\lambda\rangle_t = 174$ are omitted because they are very similar.)

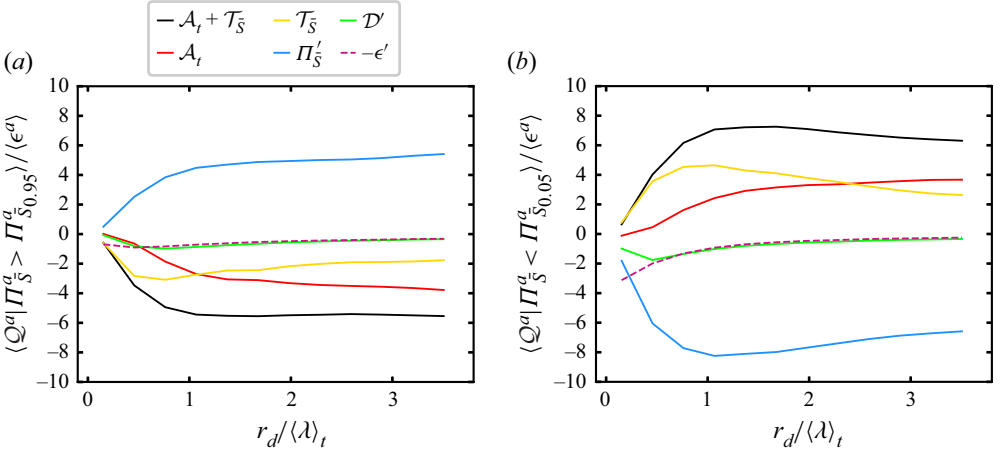

Figure 14. (*a*) Spatio-temporal averages of KHMH terms $\mathcal{Q}^a$ conditioned on the 5 % strongest spherically averaged backward (*a*) and forward (*b*) interscale transfer events. The KHMH terms are listed above figure (*a*) and $\langle Re_\lambda\rangle_t = 112$. (Corresponding plots for $\langle Re_\lambda\rangle_t = 174$ are omitted because they are very similar.)

correlations between $\mathcal{A}_t$ and $-\mathcal{T}_{\bar{S}}$ are very high (close to and above 0.95) at all scales (see figure 13), higher than the corresponding unconditional correlations. However, the conditional averages of $\mathcal{A}_t$ and $-\mathcal{T}_{\bar{S}}$ shown in figure 14 are also significantly different at all scales, implying that these strong conditional correlations do not actually amount to two-point sweeping at relatively rare forward and backward events. Furthermore, if we condition on high negative/positive values of $\Pi_{\bar{S}}$, the averages of both $\mathcal{A}_t$ and $\mathcal{T}_{\bar{S}}$ are positive/negative (figure 14), even though these conditional averages do tend to 0 as r_d tends to 0. This has two implications.

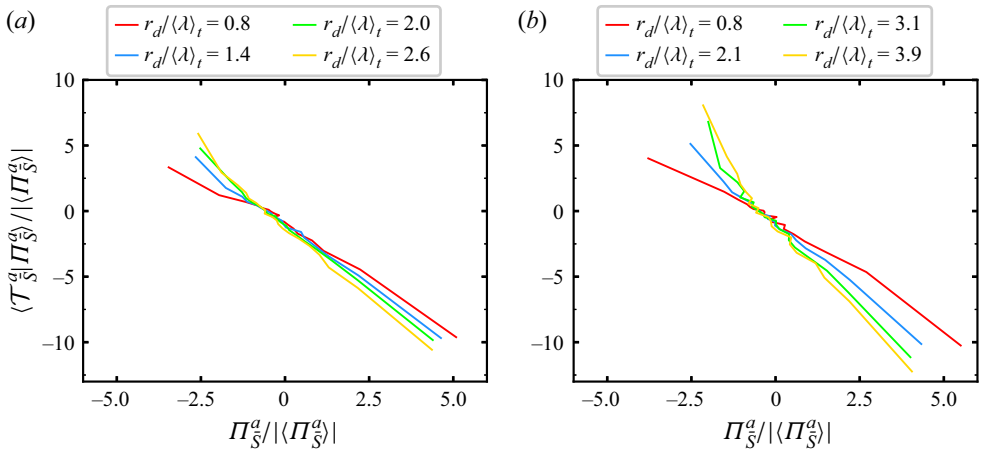

Figure 15. Spatio-temporal averages of $\mathcal{T}^a_{\bar{S}}$ across scales r_d conditioned on $\Pi^a_{\bar{S}}$ being within a certain range of $\Pi^a_{\bar{S}}$ values and we consider 20 such ranges of increasing values of $\Pi^a_{\bar{S}}$: the 5 % smallest/most negative $\Pi^a_{\bar{S}}$, the 5 % to 10 % smallest/most negative $\Pi^a_{\bar{S}}$ values and so on until the 5 % largest/most positive $\Pi^a_{\bar{S}}$ values. Results are shown for (*a*) $\langle Re\rangle_t = 112$, (*b*) $\langle Re\rangle_t = 174$.

(i) It implies that, even though $\mathcal{A}_t$ and $-\mathcal{T}_{\bar{S}}$ are very well correlated at these relatively rare events, $\mathcal{A}_t + \mathcal{T}_{\bar{S}}$ fluctuates around a constant C where $C > 0$ if we condition the fluctuations on relatively rare negative $\Pi_{\bar{S}}$ but $C < 0$ if we condition them on relatively rare positive $\Pi_{\bar{S}}$ ($C = 0$ if we do not condition). This amounts to a systematic deviation on the average from two-point sweeping even though the strong correlation between the high magnitude fluctuations of $\mathcal{A}_t$ and $-\mathcal{T}_{\bar{S}}$ point at a tendency towards sweeping that is frustrated by the presence of the comparatively low non-zero local $\Pi_{\bar{S}}$. Given (3.29), the presence of this non-zero constant C (clearly non-zero for all scales, and non-zero but tending towards zero as r_d tends to 0 well below $\langle\lambda\rangle_t$) means that the equilibrium $\Pi_{\bar{S}} \approx \mathcal{D}$ for scales smaller than $\langle\lambda\rangle_t$ does not hold either, even at scales smaller than $\langle\lambda\rangle_t$ where the conditional correlation between $\Pi_{\bar{S}}$ and $\mathcal{D}$ is significant. In fact, figure 14 shows that the conditional averages of $\Pi'_{\bar{S}}$ are much larger than those of both $\mathcal{D}'$ and $-\epsilon'$; they are much closer to those of $\mathcal{A}_t + \mathcal{T}_{\bar{S}}$.

(ii) The second implication of the conditional signs of $\mathcal{T}_{\bar{S}}$ is the existence of a relation between the conditional average of solenoidal interspace transfer rate $\mathcal{T}_{\bar{S}}$ and the solenoidal interspace transfer rate $\Pi_{\bar{S}}$ on which the average is conditioned: when one is positive/negative, the other is negative/positive, and we also find that their absolute magnitudes increase together (see figure 15). This is an observation that may prove important in the future for both subgrid scale modelling and the detailed study of the very smallest scales of turbulence fluctuations.

In conclusion, $\Pi_{\bar{S}}$ does not fluctuate with neither $-\epsilon$ nor $\mathcal{D}$. Instead, $\Pi_{\bar{S}}$ and $\mathcal{A}_t + \mathcal{T}_{\bar{S}}$ fluctuate together at all scales, in particular scales larger than $\langle\lambda\rangle_t$, and even at relatively rare interscale transfer events. At scales smaller than $\langle\lambda\rangle_t$, we have a general tendency towards two-point sweeping if we do not condition on particular events. At our relatively rare interscale transfer events this correlation tendency (now conditional) is in fact amplified but there is nevertheless a systematic average deviation from two-point sweeping consistent with the absence of equilibrium $\Pi_{\bar{S}} \approx \mathcal{D}$ at these events. Finally,

a relation exists between interspace and interscale transfer rates because the average interspace transfer rate conditioned on positive/negative values of interscale transfer rate is negative/positive. It must be stressed, however, that this relation does not imply an anti-correlation between interscale and interspace transport rates. The unconditioned correlation coefficients between $-\Pi_{\bar{S}}$ and $\mathcal{T}_{\bar{S}}$ are around 0.2 (see figure 9), and we checked that this 0.2 correlation does not change significantly if we condition on relatively rare intense occurrences of interscale transfer rate.

5. Inhomogeneity contribution to interscale transfer

5.1. *Average values and probability density functions*

The decomposition $\Pi = \Pi_{\bar{I}} + \Pi_{\bar{S}}$ helped us distinguish between the solenoidal vortex stretching/compression and the pressure-related aspects of the interscale transfer. As recently shown by Alves Portela *et al.* (2020), the interscale transfer rate Π can also be decomposed in a way that brings out the fact that it has a direct inhomogeneity contribution to it. This last part of the present study is an examination of the decomposition introduced by Alves Portela *et al.* (2020) that is $\Pi = \Pi_I + \Pi_H$, where

$$\Pi_I = \frac{1}{2}\delta u_i \frac{\partial}{\partial x_i}(u_k^+ u_k^+ - u_k^- u_k^-), \tag{5.1}$$

$$\Pi_H = -2\delta u_i \frac{\partial}{\partial r_i}(u_k^- u_k^+). \tag{5.2}$$

Here Π_I can be locally/instantaneously non-zero only in the presence of a local/instantaneous inhomogeneity. However, it averages to zero, i.e. $\langle \Pi_I \rangle = 0$, in periodic/statistically homogeneous turbulence. Note that $\Pi = \Pi_I = \Pi_H = 0$ at $\boldsymbol{r} = \boldsymbol{0}$. With $\boldsymbol{r}$-orientation averaging, the decomposition $\Pi^a = \Pi_I^a + \Pi_H^a$ is unique in the sense that any potentially suitable (e.g. such that it equals 0 at $\boldsymbol{r} = \boldsymbol{0}$) $\boldsymbol{x}$-gradient term added to Π_I vanishes after $\boldsymbol{r}$-orientation averaging (see Alves Portela *et al.* 2020).

An equivalent expression for Π_I that immediately reveals where the decomposition $\Pi = \Pi_I + \Pi_H$ comes from is $\Pi_I = \delta u_i(\partial/\partial r_i)(u_k^+ u_k^+ + u_k^- u_k^-)$. Given that the total interscale transfer rate is $\Pi = \delta u_i(\partial/\partial r_i)(\delta u_k \delta u_k)$, the Π_I part of the interscale transfer concerns the transferred energy differences coming mostly from differences between velocity amplitudes, i.e. local/instantaneous inhomogeneities of 'turbulence intensity' in the flow; the Π_H part of the interscale transfer concerns transferred energy differences coming mostly from differences between velocity orientations. Consistently with its link to local/instantaneous non-homogeneity, Π_I can be written in the form (5.1) making it clear that Π_I is zero where and when fluctuating velocity magnitudes are locally uniform.

In comparing the decompositions $\Pi = \Pi_{\bar{S}} + \Pi_{\bar{I}}$ and $\Pi = \Pi_I + \Pi_H$, it is worth noting that $\Pi_I = \Pi_{I_{\bar{I}}}$ given that $\Pi_{I_{\bar{S}}} = 0$ from its centroid gradient form (see (5.1)). It therefore follows that

$$\Pi_{\bar{S}} = \Pi_{H_{\bar{S}}}, \tag{5.3}$$

$$\Pi_{\bar{I}} = \Pi_I + \Pi_{H_{\bar{I}}}. \tag{5.4}$$

The inhomogeneity-based interscale transfer rate influences only the irrotational part of the total interscale transfer rate whereas Π_H influences both the irrotational and the solenoidal parts. As $\langle \Pi_I \rangle = 0$ and $\langle \Pi_{\bar{I}} \rangle = 0$, it follows that $\langle \Pi_{H_{\bar{I}}} \rangle = 0$. More to the point, $\langle \Pi_{\bar{S}} \rangle$ equals

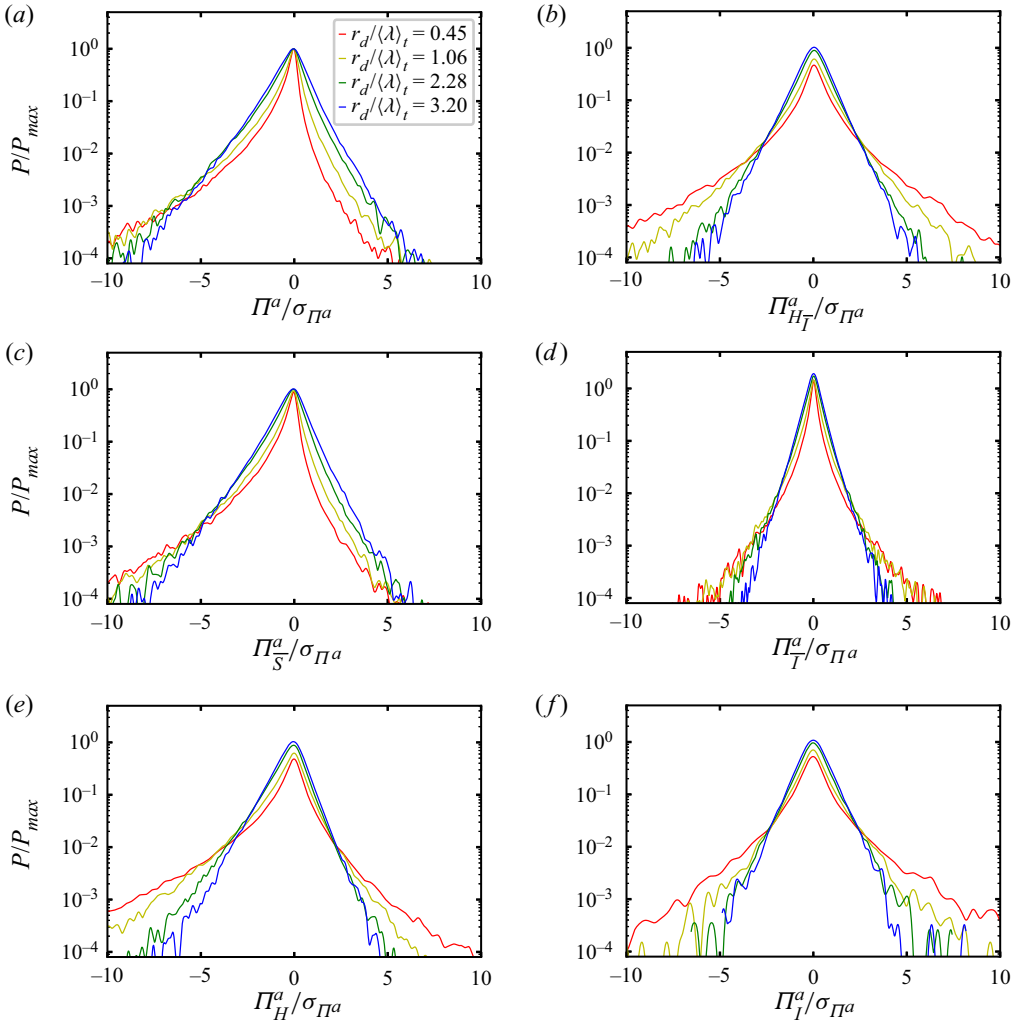

Figure 16. (*a–f*) The PDFs of Π decompositions ($\Pi, \Pi_{H_{\bar{I}}}, \Pi_{\bar{S}}, \Pi_{\bar{I}}, \Pi_H, \Pi_I$) at $\langle Re_\lambda\rangle_t = 112$. Here σ_{Π^a} denotes the standard deviation of Π^a and P_{max} denotes the maximum value of the PDF of Π^a. The inhomogeneity and homogeneity interscale transfer rates Π_I and Π_H are defined in (5.1)–(5.2) and the irrotational part of the homogeneity interscale transfer rate $\Pi_{H_{\bar{I}}}$ in (5.4).

$\langle\Pi_{H_{\bar{S}}}\rangle$ and so (3.28) reduces to

$$\langle\Pi\rangle = \langle\Pi_{H_{\bar{S}}}\rangle = \langle\mathcal{D}_{r,v}\rangle - \langle\epsilon\rangle + \langle\mathcal{I}\rangle. \tag{5.5}$$

The part of the interscale transfer rate that is present in the average interscale transfer/cascade dynamics is in fact $\Pi_{H_{\bar{S}}}$.

Given that the average interscale transfer is controlled by $\Pi_{H_{\bar{S}}} = \Pi_{\bar{S}}$, it is worth asking whether the well-known negative skewness of the probability density function (PDF) of Π^a (see, e.g. Yasuda & Vassilicos (2018) and references therein) is also present in the PDF of $\Pi^a_{\bar{S}}$ or/and whether it is spread across different terms of our two interscale transfer rate decompositions. In figure 16 we plot the PDFs of Π^a and of the different $\boldsymbol{r}$-orientation-averaged terms in the decompositions of Π that we use. It is clear that the

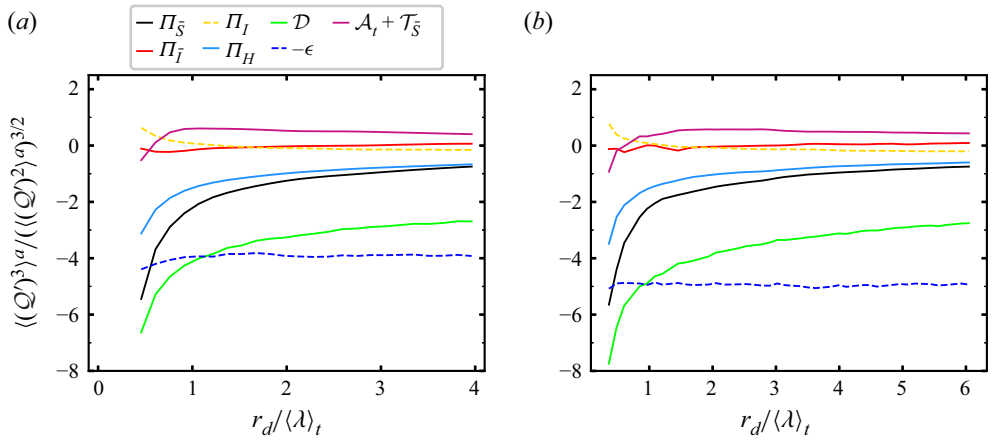

Figure 17. Skewness factors for KHMH terms $\mathcal{Q}$ listed on top of (*a*): (*a*) $\langle Re_\lambda\rangle_t = 112$, (*b*) $\langle Re_\lambda\rangle_t = 174$.

PDFs of Π and $\Pi_{\bar{S}}$ are nearly identical whilst the PDFs of Π_H are different though also negatively skewed. The PDFs of $\Pi_{H_{\bar{I}}}$, $\Pi_{\bar{I}}$ and Π_I are not significantly skewed. In figure 17 we plot the skewnes factors of the various interscale transfer terms as well as some other KHMH terms. The inhomogeneity interscale transfer Π_I has close to zero skewness across scales. Both $\Pi_{\bar{S}}$ and Π_H are negatively skewed, the former more so than the latter. Given (5.3)–(5.4) and $\Pi_H = \Pi_{\bar{S}} + \Pi_{H_{\bar{I}}}$, this difference in skewness factors is due to the irrotational part of Π_H that is not significantly skewed and reduces the skewness of Π_H relative to that of $\Pi_{\bar{S}}$. All in all, the skewness towards forward rather than inverse interscale transfers is present in its homogeneous and solenoidal components but is absent in its non-homogeneous and irrotational parts.

Figure 17 also shows that $\mathcal{A}_t + \mathcal{T}_{\bar{S}}$ is slightly positively skewed with flatness factors of approximately 0.5 at scales $r_d \geq \langle\lambda\rangle_t$ and close to 0 or below at scales below $\langle\lambda\rangle_t$. The skewness factor of $-\Pi_{\bar{S}}$ with which $\mathcal{A}_t + \mathcal{T}_{\bar{S}}$ is very well correlated (as we have seen in the previous section) is about the same at scales close to the integral scale but steadily increases to values well above 0.5 as r decreases, reaching nearly 6.0 at scales close to $0.5\langle\lambda\rangle_t$. This is a concrete illustration of the fact already mentioned earlier in this paper that $\mathcal{A}_t + \mathcal{T}_{\bar{S}} \approx -\Pi_{\bar{S}}$ is a very good approximation for most locations and most times but not all. Given the very significantly increased correlation/anti-correlation of $\Pi_{\bar{S}}$ with both $\mathcal{D}$ and ϵ at relatively intense forward/inverse interscale transfer events and with decreasing scale r_d, it is natural to expect the skewness factor of $\Pi_{\bar{S}}$ to veer towards the skewness factors of $\mathcal{D}$ and $-\epsilon$ which, as can be seen in figure 17, are highly negative with values between -3.0 and -7.0.

5.2. *Correlations*

We now consider the local/instantaneous relations between the various interscale transfer terms in terms of correlation coefficients plotted in figure 18(*a*). First, note the very strong correlation between Π and $\Pi_{\bar{S}}$ and the moderate correlation between Π and $\Pi_{\bar{I}}$. Even though Π and $\Pi_{\bar{S}}$ are highly correlated, we cannot ignore $\Pi_{\bar{I}}$ and cannot write $\Pi \approx \Pi_{\bar{S}}$. As seen earlier in the paper, we cannot ignore $\Pi_{\bar{I}}$ because it is the part of the interscale transfer that balances the pressure term, but we have also seen that the fluctuation magnitude of $\Pi_{\bar{S}}$ is significantly higher than the fluctuation magnitude of $\Pi_{\bar{I}}$. However, even if smaller, the fluctuation magnitude of $\Pi_{\bar{I}}$ is not negligible. There is no correlation between $\Pi_{\bar{S}}$ and $\Pi_{\bar{I}}$ (see figure 18*b*), and so Π correlates with both $\Pi_{\bar{S}}$ (strongly) and $\Pi_{\bar{I}}$

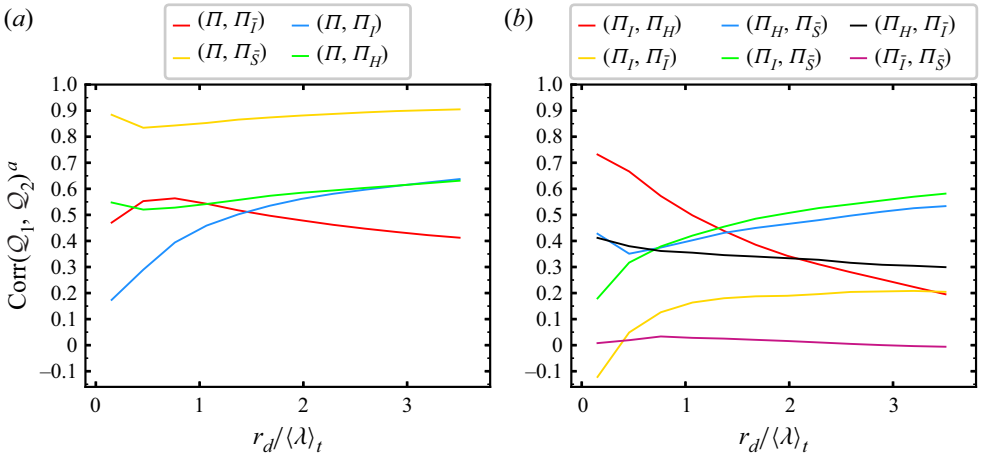

Figure 18. Correlation coefficients between various Π decompositions $(\mathcal{Q}_1, \mathcal{Q}_2)$ listed on top of the figures at $\langle Re_\lambda \rangle_t = 112$. (Corresponding plots for $\langle Re_\lambda \rangle_t = 174$ are omitted because they are very similar.)

(moderately) for different independent reasons. Here Π feels the influence of solenoidal vortex stretching/compression via $\Pi_{\tilde{S}}$ and the influence of pressure fluctuations via $\Pi_{\tilde{I}}$, the former influencing Π more than the latter.

Figure 18(*a*) also shows significantly smaller correlations between Π and Π_H than between Π and $\Pi_{\tilde{S}}$. This must be due to a decorrelating effect of $\Pi_{H_{\tilde{I}}}$ as $\Pi_H = \Pi_{\tilde{S}} + \Pi_{H_{\tilde{I}}}$. The correlations between Π and Π_I are even smaller at the smaller scales but at integral size scales these correlations are equal to those between Π and Π_H (figure 18*a*).

Figure 18(*b*) reveals a strong anti-correlation between Π_I and Π_H at the small scales and a weak one at the large scales. As the scales decrease, the interscale transfers of fluctuating velocity differences caused by local/instantaneous non-homogeneities and the interscale transfers of fluctuating velocity differences caused by orientation differences get progressively more anti-correlated. This anti-correlation tendency results in Π_H and Π_I having larger fluctuation magnitudes than Π at smaller scales, in particular scales smaller than $\langle \lambda \rangle_t$ (verified with our DNS data but not shown here for economy of space).

The other significant correlations revealed in figure 18(*b*) are those between Π_H and $\Pi_{\tilde{S}}$ and those between Π_I and $\Pi_{\tilde{S}}$, particularly as r_d increases from around/below $\langle \lambda \rangle_t$ to the integral length scale. These correlations relate to the very strong correlations between Π and $\Pi_{\tilde{S}}$ but are weaker. One can imagine that $\Pi_{\tilde{S}}$ correlates with Π_H sometimes and with Π_I some other times, but not too often with both given that Π_I and Π_H tend to be anti-correlated, and that this happens in a way subjected to a continuously strong correlation between $\Pi = \Pi_H + \Pi_I$ and $\Pi_{\tilde{S}}$.

We finally consider in figure 19 the average contributions of the various Π-decomposition terms conditional on relatively rare intense Π events. We calculate averages conditioned on 5 % most negative (forward transfer) $\Pi_{\tilde{S}}$ events (values of $\Pi_{\tilde{S}}$ for which the probability that $\Pi_{\tilde{S}}$ is smaller than a negative value $\Pi_{\tilde{S}_{0.05}}$ is 0.05) and on 5 % most positive $\Pi_{\tilde{S}}$ (inverse transfer) events (values of $\Pi_{\tilde{S}}$ for which the probability that $\Pi_{\tilde{S}}$ is larger than a positive value $\Pi_{\tilde{S}_{0.95}}$ is also 0.05). All these averages tend to 0 as r_d tends to 0 below $\langle \lambda \rangle_t$. The largest such conditional averages are those of $\Pi\prime$ followed by those of $\Pi'_{\tilde{S}}$. This is the forward-skewed part of the interscale transfer (in terms of PDFs) and it is dominant at both forward and backward intense interscale transfer events. The weakest such conditional averages are those of $\Pi_{\tilde{I}}$ for all r_d and both forward and inverse

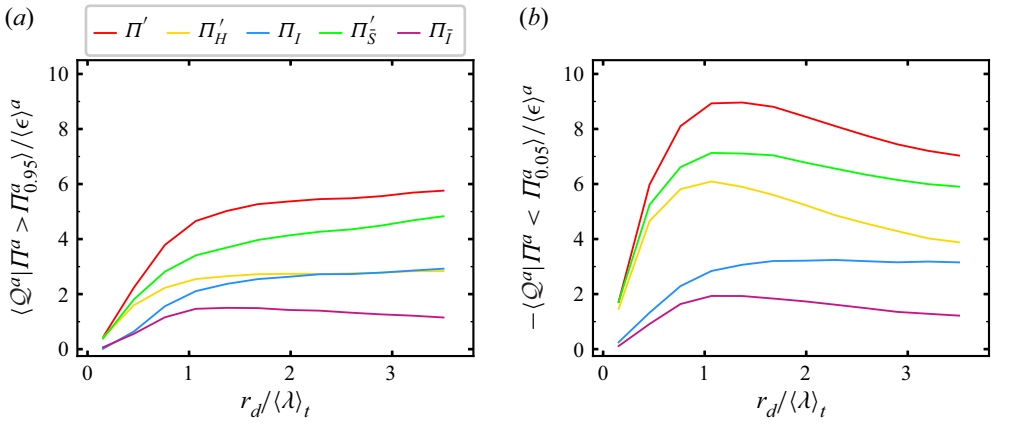

Figure 19. Average values of Π decompositions conditioned on (*a*) intense backward events, (*b*) intense forward events at $\langle Re_\lambda \rangle_t = 112$. The top of (*a*) lists the Π decompositions. (Corresponding plots for $\langle Re_\lambda \rangle_t = 174$ are omitted because they are very similar.)

extreme interscale transfer events. This is consistent with our observation in § 3.4 that the unconditional fluctuation magnitude of $\Pi_{\bar{I}}$ is smaller than the unconditional fluctuation magnitudes of Π followed by those of $\Pi_{\bar{S}}$.

The most interesting point to note in figure 19, however, is the difference between conditional averages of Π'_H and Π_I when conditioned on intense forward or intense inverse interscale transfer events. Whilst the conditional averages of these two quantities are about the same at intense inverse events, they differ substantially at forward transfer events where the conditional average of $-\Pi'_H$ is substantially higher than the conditional average of $-\Pi_I$ except close to the integral length scale.

6. Conclusions

The balance between space–time-averaged interscale energy transfer rate on the one hand and space–time-averaged viscous diffusion, turbulence dissipation rate and power input on the other does not represent in any way the actual energy transfer dynamics in statistically stationary homogeneous/periodic turbulence. In this paper we have studied the fluctuations of two-point acceleration terms in the NSD equation and their relation to the various terms of the KHMH equation. We now give a point-by-point summary of our results on KHMH dynamics (A), conditional KHMH dynamics (B) and inhomogeneity and homogeneity contributions to the interscale transfer rate (C).

A1. The various corresponding terms in the NSD and KHMH equations behave similarly relative to each other because the two-point velocity difference has a similar tendency of alignment with each one of the acceleration terms of the NSD equation (see figure 8).

A2. The terms in the two-point energy balance that fluctuate with the highest magnitudes are $\mathcal{A}'_c$ followed closely by the time-derivative term $\mathcal{A}_t$ and the solenoidal interspace transfer rate $\mathcal{T}_{\bar{S}}$. The fluctuation intensity of $\mathcal{A}_t + \mathcal{T}_{\bar{S}}$ is much reduced by comparison to both these terms (two-point sweeping) and is comparable to the fluctuation intensity of the solenoidal interscale transfer rate. The solenoidal interscale transfer rate, which averages according to (3.28), does not fluctuate with viscous diffusion and/or turbulence dissipation with which it

is negligibly correlated at scales larger than $\langle\lambda\rangle_t$ and rather weakly correlated at scales smaller than $\langle\lambda\rangle_t$. Its fluctuation magnitude is also significantly larger than that of $\mathcal{D}_{r,\nu}$, $-\epsilon$ and $\mathcal{I}$ at all scales (see figure 6 for KHMH magnitude results). Instead, the solenoidal interscale transfer rate fluctuates with $\mathcal{A}_t + \mathcal{T}_{\bar{S}}$ with which it is extremely well correlated at length scales larger than $\langle\lambda\rangle_t$ and very significantly correlated at length scales smaller than $\langle\lambda\rangle_t$ (see KHMH correlation results in figure 9).

A3. In fact, for scales larger than $\langle\lambda\rangle_t$, the relation

$$\mathcal{A}_t + \mathcal{T}_{\bar{S}} + \Pi'_{\bar{S}} \approx 0, \tag{6.1}$$

is a good approximation for most times and most locations in the flow. Here $\mathcal{A}_t + \mathcal{T}_{\bar{S}}$ can be viewed as a Lagrangian time rate of change of $|\delta\boldsymbol{u}|^2$ moving with $(\boldsymbol{u}^+ + \boldsymbol{u}^-)/2$. As more than average $|\delta\boldsymbol{u}|^2$ is cascaded from larger to smaller scales at a particular location ($\Pi'_{\bar{S}} < 0$), $\mathcal{A}_t + \mathcal{T}_{\bar{S}}$ increases; and as more than average $|\delta\boldsymbol{u}|^2$ is inverse cascaded from smaller to larger scales ($\Pi'_{\bar{S}} > 0$), $\mathcal{A}_t + \mathcal{T}_{\bar{S}}$ decreases (see § 4.1). The relatively rare space–time events that do not comply with this relation are responsible for the different skewness factors of the PDFs of $\mathcal{A}_t + \mathcal{T}_{\bar{S}}$ (small, mostly positive, skewness factor) and of $\Pi'_{\bar{S}}$ (negative skewness factor reaching increasingly large negative values with decreasing scale).

A4. As the length scale (i.e. two point separation length) decreases, the correlation between $\mathcal{A}_t$ and $-\mathcal{T}_{\bar{S}}$ increases and so do their fluctuation magnitudes relative to the fluctuation magnitude of $\Pi'_{\bar{S}}$ that reaches to be an order of magnitude smaller by comparison. In this limit, the correlation between $\mathcal{A}_t$ and $-\Pi_{\bar{S}}$ decreases. At length scales smaller than $\langle\lambda\rangle_t$ the correlation between $\mathcal{A}_t$ and $-\mathcal{T}_{\bar{S}}$ is extremely good indicating a tendency towards two-point sweeping. However, the correlation between $\mathcal{A}_t + \mathcal{T}_{\bar{S}}$ and $\Pi'_{\bar{S}}$ remains strong even if reduced from its near perfect values at length scales larger than $\langle\lambda\rangle_t$ and there remains a small difference of fluctuation magnitudes between $\mathcal{A}_t$ and $\mathcal{T}_{\bar{S}}$ that is mostly related to the small fluctuation magnitude of $\Pi'_{\bar{S}}$. At the other end of the length scale range, i.e. as the length scale tends towards the integral scale and larger, the fluctuation magnitudes of $\mathcal{T}_{\bar{S}}$ and $\Pi'_{\bar{S}}$ tend to become the same (the scatter plots in figures 11 and 12 evidence these behaviours).

A5. The irrotational part of the interscale transfer rate has zero spatio-temporal average but is exactly equal to the irrotational part of the interspace transfer rate and half the two-point pressure work term in the KHMH equation. A complete dynamic picture of the interscale transfer rate needs to also take this into account, even though the fluctuation magnitudes of these irrotational terms are smaller than those of the terms discussed in the previous paragraph. In fact, the exact relation $\Pi_{\bar{I}} = \mathcal{T}_{\bar{I}} = \frac{1}{2}\mathcal{T}_p$ explains the significant correlation between interscale transfer rate Π and $\mathcal{T}_p$ reported by Yasuda & Vassilicos (2018).

B1. The increase towards small correlations at length scales below $\langle\lambda\rangle_t$ between $\Pi_{\bar{S}}$ and both $\mathcal{D}_{r,\nu}$ and $-\epsilon$ is accountable to the significant correlations between these terms at these viscous scales when conditioned on relatively rare intense $\Pi_{\bar{S}}$ events, both forward cascading events with negative values of $\Pi_{\bar{S}}$ of high magnitude and backward cascading events with positive values of $\Pi_{\bar{S}}$ of high magnitude. The choice of $\Pi_{\bar{S}}$ to identify relatively rare intense events is predicated on the fact that the PDFs of $\Pi_{\bar{S}}$ are negatively skewed similarly to the PDFs of Π, whereas the PDFs of $\Pi_{\bar{I}}$ are not (the interscale transfer PDFs are given in figure 16).

The solenoidal part of the interscale transfer rate derives from the integrated two-point vorticity equation and includes non-local vortex stretching/compression effects at all scales whereas the irrotational part of the interscale transfer rate derives from the integrated Poisson equation for two-point pressure fluctuations (see Appendix C for mathematical details).

B2. At these relatively rare intense interscale transfer rate events, the tendency for two-point sweeping may appear increased because of the extremely good conditional correlation between $\mathcal{A}_t$ and $-\mathcal{T}_{\bar{S}}$ at all length scales; however, $\mathcal{A}_t$ and $-\mathcal{T}_{\bar{S}}$ also have very significantly different average values given the high absolute values of $\Pi_{\bar{S}}$ at these relatively rare interscale transfer events (see figures 13 and 14). This implies that there is neither local/instantaneous sweeping nor local/instantaneous balance between $\Pi_{\bar{S}}$ and $\mathcal{D}$ or $\Pi_{\bar{S}}$ and $-\epsilon$ at these relatively rare intense events, a conclusion confirmed by the observation that the conditional averages and the conditional fluctuation magnitudes of $\Pi_{\bar{S}}$ are much higher than those of $\mathcal{D}$ and $-\epsilon$ in absolute values.

B3. Another property of these relatively rare intense solenoidal interscale transfer rate events is that the conditional averages of solenoidal interscale and interspace transfer rates have opposite signs when sampling on these events (see figure 15). There is therefore a relation between them that may however be concealed by the fact that the fluctuation magnitudes of the interspace transport rate are higher than those of the interscale transfer rate.

C1. We have also considered the decomposition into homogeneous and inhomogeneous interscale transfer rates recently introduced by Alves Portela *et al.* (2020) (see (5.1) and (5.2)) and have studied their fluctuations in statistically stationary homogeneous turbulence. The PDFs of the homogeneous interscale transfer rate are skewed towards forward cascade events whereas the PDFs of the inhomogeneous interscale transfer rate are not significantly skewed. However, the skewness factors of the PDFs of the homogeneous interscale transfer rate are not as high as those of both the full and the solenoidal interscale transfer rates. Relating to this, Π is highly correlated with $\Pi_{\bar{S}}$ more than with $\Pi_{\bar{I}}$, Π_H and Π_I with all of which Π is, nevertheless, significantly correlated.

C2. There is an increasing correlation between Π_I and $-\Pi_H$ as the length scale decreases, in particular below $\langle\lambda\rangle_t$ where it reaches values above 0.6 (see figure 18). The interscale transfer of velocity difference energy caused by local inhomogeneities in fluctuating velocity magnitudes tends to cancel the interscale transfer of fluctuating velocity difference energy caused by misalignments between the two neighbouring fluctuating velocities, in particular at length scales below $\langle\lambda\rangle_t$. As a result, the fluctuation magnitudes of Π are smaller than those of both Π_I and $-\Pi_H$.

C3. Finally, the decomposition $\Pi = \Pi_I + \Pi_H$ can be used to physically distinguish between intense forward and intense inverse interscale transfer events. The averages of Π'_H and Π_I when conditioned on intense inverse interscale transfer events are about the same, but they differ substantially when conditioned on intense forward interscale transfer events where the conditional average of $-\Pi'_H$ is substantially higher than the conditional average of $-\Pi_I$ except close to the integral length scale (see figure 19).

Future subgrid scale models for LES that are dynamic reduced-order approaches to turbulent flows and their fluctuating large scales cannot rely on average cascade phenomenology describing spatio-temporal averages and should benefit from detailed

descriptions of the fluctuating dynamics of interscale and interspace energy transfers such as the one presented in this paper. Whilst LES models based on local equilibrium such as the Smagorinsky model can reproduce structure function exponents and correlations between velocity increments and subgrid-scale energy transfers as shown by Linkmann, Buzzicotti & Biferale (2018), Dairay *et al.* (2017) have found that the Smagorinsky model is unable to suppress small-scale spurious oscillations arising from numerical errors. Furthermore, the recent review by Moser, Haering & Yalla (2021) makes it clear that the need for new subgrid models that can faithfully operate with coarse resolutions remains unanswered. The results in the present paper suggest that LES models based on local equilibrium (e.g. the Smagorinsky model) cannot be fully suitable for calculating fluctuations in subgrid stresses, a weakness that may become increasingly evident with coarser resolution. On the other hand, the good correlations between subgrid stresses from similarity models (Bardina, Ferziger & Reynolds 1980; Cimarelli, Abbà & Germano 2019) and subgrid stresses from DNS suggest that these models might indeed approximate (unawarely) at least some of the cascade dynamics reported in this paper, for example, the fact that $\mathcal{A}_t + \mathcal{T}_{\bar{S}} + \Pi'_{\bar{S}} \approx 0$ holds in most of the flow most of the time. This relation incorporates both forward and backward interscale transfers, yet a recent work by Vela-Martín (2022) argues that backscatter represents spatial fluxes and can therefore be ignored. It is not yet clear how such a claim can be understood in the context of the present paper's results. Some new questions are therefore now raised concerning LES subgrid stress modelling that also need to be addressed in future work.

Acknowledgements. We thank Professor S. Goto for allowing us to use his parallelised pseudo-spectral DNS code for periodic turbulence.

Funding. H.S.L. and J.C.V. acknowledge support from EPSRC award number EP/L016230/1. J.C.V. also acknowledges the Chair of Excellence CoPreFlo funded by I-SITE-ULNE (grant no. R-TALENT-19-001-VASSILICOS); MEL (grant no. CONVENTION-219-ESR-06) and Region Hauts de France (grant no. 20003862).

Declaration of interests. The authors report no conflict of interest.

Author ORCIDs.
H.S. Larssen https://orcid.org/0000-0002-5571-1753;
J.C. Vassilicos https://orcid.org/0000-0003-1828-6628.

Appendix A. The Helmholtz decomposition in Fourier space

In this appendix we list the Helmholtz decomposition for periodic fields and note how this decomposition relates to the more general solution of the Helmholtz decomposition in the case of incompressible fields and fields that can be written as gradients of scalar fields.

Let $\boldsymbol{q}(\boldsymbol{x}, t)$ be a periodic, twice continuously differentiable three-dimensional vector field with the Helmholtz decomposition $\boldsymbol{q}(\boldsymbol{x}, t) = \boldsymbol{q}_I(\boldsymbol{x}, t) + \boldsymbol{q}_S(\boldsymbol{x}, t)$, where $\boldsymbol{q}_I(\boldsymbol{x}, t) = -\boldsymbol{\nabla}_{\boldsymbol{x}}\phi(\boldsymbol{x}, t)$, $\boldsymbol{q}_S(\boldsymbol{x}, t) = \boldsymbol{\nabla}_{\boldsymbol{x}} \times \boldsymbol{B}(\boldsymbol{x}, t)$. The scalar and vector potentials ϕ and $\boldsymbol{B}$ are unique within constants when $\boldsymbol{\nabla}_{\boldsymbol{x}} \cdot \boldsymbol{q}$ and $\boldsymbol{\nabla}_{\boldsymbol{x}} \times \boldsymbol{q}$ are known in the domain and $\boldsymbol{q}$ is known at the boundary (Bhatia *et al.* 2013). Here $\boldsymbol{q}(\boldsymbol{x}, t)$ has the Fourier representation $\hat{\boldsymbol{q}}(\boldsymbol{k}, t)$, which can be decomposed into a component parallel to $\boldsymbol{k}$ (the longitudinal $\hat{\boldsymbol{q}}^L$) and transverse to $\boldsymbol{k}$ (the transverse $\hat{\boldsymbol{q}}^{\mathrm{T}}$),

$$\hat{\boldsymbol{q}}^L(\boldsymbol{k}, t) = \frac{\boldsymbol{k}[\hat{\boldsymbol{q}}(\boldsymbol{k}, t) \cdot \boldsymbol{k}]}{k^2}, \quad \hat{\boldsymbol{q}}^T(\boldsymbol{k}, t) = \hat{\boldsymbol{q}}(\boldsymbol{k}, t) - \hat{\boldsymbol{q}}^L(\boldsymbol{k}, t). \tag{A1a,b}$$

It can be easily shown (see, e.g. Stewart 2012) that the irrotational part of $\boldsymbol{q}$ equals its longitudinal part $\boldsymbol{q}_I = \boldsymbol{q}^L$ and that the solenoidal part of $\boldsymbol{q}$ equals its transverse part $\boldsymbol{q}_S = \boldsymbol{q}^{\mathrm{T}}$. Hence, (A1*a*,*b*) provides the Fourier representation of the Helmholtz decomposition of $\boldsymbol{q}$.

The Helmholtz decomposition can also be written for very general boundary conditions as (Sprössig 2010)

$$\boldsymbol{q}_{IV}(\boldsymbol{x}, t) = \frac{1}{4\pi}\int_V \mathrm{d}\boldsymbol{y}\frac{\boldsymbol{x}-\boldsymbol{y}}{|\boldsymbol{x}-\boldsymbol{y}|^3}[\nabla_{\boldsymbol{y}}\cdot\boldsymbol{q}(\boldsymbol{y}, t)], \tag{A2}$$

$$\boldsymbol{q}_{IB}(\boldsymbol{x}, t) = -\frac{1}{4\pi}\int_S \mathrm{d}S_{\boldsymbol{y}}\frac{\boldsymbol{x}-\boldsymbol{y}}{|\boldsymbol{x}-\boldsymbol{y}|^3}[\hat{\boldsymbol{n}}_{\boldsymbol{y}}\cdot\boldsymbol{q}(\boldsymbol{y}, t)], \tag{A3}$$

$$\boldsymbol{q}_{SV}(\boldsymbol{x}, t) = -\frac{1}{4\pi}\int_V \mathrm{d}\boldsymbol{y}\frac{\boldsymbol{x}-\boldsymbol{y}}{|\boldsymbol{x}-\boldsymbol{y}|^3}\times[\nabla_{\boldsymbol{y}}\times\boldsymbol{q}(\boldsymbol{y}, t)], \tag{A4}$$

$$\boldsymbol{q}_{SB}(\boldsymbol{x}, t) = \frac{1}{4\pi}\int_S \mathrm{d}S_{\boldsymbol{y}}\frac{\boldsymbol{x}-\boldsymbol{y}}{|\boldsymbol{x}-\boldsymbol{y}|^3}\times[\hat{\boldsymbol{n}}_{\boldsymbol{y}}\times\boldsymbol{q}(\boldsymbol{y}, t)], \tag{A5}$$

where $\boldsymbol{q}_I = \boldsymbol{q}_{IV} + \boldsymbol{q}_{IB}$, $\boldsymbol{q}_S = \boldsymbol{q}_{SV} + \boldsymbol{q}_{SB}$ and $\hat{\boldsymbol{n}}_{\boldsymbol{y}}$ denotes the unit surface normal at $\boldsymbol{y}$ and $dS_{\boldsymbol{y}}$ is the differential surface element at $\boldsymbol{y}$. For periodic vector fields $\boldsymbol{q}(\boldsymbol{x}, t)$ that are incompressible or that can be written as the gradient of a scalar, this solution simplifies. In the case of a field $\boldsymbol{q}(\boldsymbol{x}, t)$ that is incompressible $\nabla_{\boldsymbol{x}}\cdot\boldsymbol{q}(\boldsymbol{x}, t) = 0$, it can be shown that $\hat{\boldsymbol{q}}(\boldsymbol{k}, t)\cdot\boldsymbol{k} = 0$ for every $\boldsymbol{k}$ (Pope 2000). By inspection of (A1*a*,*b*), it is clear that this condition yields $\hat{\boldsymbol{q}}^L(\boldsymbol{k}, t) = 0$ for every $\boldsymbol{k}$ such that $\hat{\boldsymbol{q}}(\boldsymbol{k}, t) = \hat{\boldsymbol{q}}(\boldsymbol{k}, t)^{\mathrm{T}}$. By applying the Fourier transform to this relation and applying $\boldsymbol{q}^{\mathrm{T}}(\boldsymbol{x}, t) = \boldsymbol{q}_S(\boldsymbol{x}, t)$ from above, we have $\boldsymbol{q}(\boldsymbol{x}, t) = \boldsymbol{q}_S(\boldsymbol{x}, t)$ for incompressible periodic vector fields. In the case of $\boldsymbol{q}(\boldsymbol{x}, t) = \nabla_{\boldsymbol{x}}\psi(\boldsymbol{x}, \boldsymbol{t})$, where $\psi(\boldsymbol{x}, t)$ is some scalar field, it can be shown that $\hat{\boldsymbol{q}}(\boldsymbol{k}, t) = \mathrm{i}\boldsymbol{k}\hat{\psi}(\boldsymbol{k}, t)$ (Pope 2000). If we insert this expression into the definition of $\hat{\boldsymbol{q}}^L(\boldsymbol{k}, t)$, it follows that $\hat{\boldsymbol{q}}(\boldsymbol{k}, t) = \hat{\boldsymbol{q}}^L(\boldsymbol{k}, t)$, which implies that $\boldsymbol{q}(\boldsymbol{x}, t) = \boldsymbol{q}_I(\boldsymbol{x}, t)$. If these properties are combined with (A2)–(A5), we have that a periodic incompressible vector field will have $\boldsymbol{q}_{IB} = \boldsymbol{q}_{IV} = 0$ and that a periodic vector field that can be written as a gradient of a scalar field has $\boldsymbol{q}_{SB} = \boldsymbol{q}_{SV} = 0$.

Appendix B. Irrotational and solenoidal NSD transport terms in Fourier space

We start this appendix with demonstrating that $\delta\boldsymbol{q}_I = \delta\boldsymbol{q}_{\bar{I}}$ and $\delta\boldsymbol{q}_S = \delta\boldsymbol{q}_{\bar{S}}$ for a periodic vector field $\boldsymbol{q}$ (see the second paragraph of § 3.3). The field $\boldsymbol{q}$ has the Fourier representation

$$\boldsymbol{q}(\boldsymbol{x}, t) = \sum_{\boldsymbol{k}}\hat{\boldsymbol{q}}(\boldsymbol{k}, t)\exp(\mathrm{i}\boldsymbol{k}\cdot\boldsymbol{x}), \tag{B1}$$

with the shifted fields

$$\boldsymbol{q}^+(\boldsymbol{x}, \boldsymbol{r}, t) = \boldsymbol{q}(\boldsymbol{x}+\boldsymbol{r}/2, t) = \sum_{\boldsymbol{k}}\hat{\boldsymbol{q}}(\boldsymbol{k}, t)\exp(\mathrm{i}\boldsymbol{k}\cdot(\boldsymbol{x}+\boldsymbol{r}/2)), \tag{B2}$$

$$\boldsymbol{q}^-(\boldsymbol{x}, \boldsymbol{r}, t) = \boldsymbol{q}(\boldsymbol{x}-\boldsymbol{r}/2, t) = \sum_{\boldsymbol{k}}\hat{\boldsymbol{q}}(\boldsymbol{k}, t)\exp(\mathrm{i}\boldsymbol{k}\cdot(\boldsymbol{x}-\boldsymbol{r}/2)), \tag{B3}$$

which have the Fourier coefficients

$$\widehat{\boldsymbol{q}^+}(\boldsymbol{k}, \boldsymbol{r}, t) = \hat{\boldsymbol{q}}(\boldsymbol{k}, t)\exp(\mathrm{i}\boldsymbol{k}\cdot\boldsymbol{r}/2), \tag{B4}$$

$$\widehat{\boldsymbol{q}^-}(\boldsymbol{k}, \boldsymbol{r}, t) = \hat{\boldsymbol{q}}(\boldsymbol{k}, t)\exp(-\mathrm{i}\boldsymbol{k}\cdot\boldsymbol{r}/2). \tag{B5}$$

From the definition of the irrotational part of a vector field in (A1*a*,*b*), it follows that

$$\delta \boldsymbol{q}_I(\boldsymbol{x},\boldsymbol{r},t) = \boldsymbol{q}_I^+(\boldsymbol{x},\boldsymbol{r},t) - \boldsymbol{q}_I^-(\boldsymbol{x},\boldsymbol{r},t), \tag{B6}$$

$$= \sum_{\boldsymbol{k}} [\widehat{\boldsymbol{q}_I^+}(\boldsymbol{k},\boldsymbol{r},t) - \widehat{\boldsymbol{q}_I^-}(\boldsymbol{k},\boldsymbol{r},t)] \exp(\mathrm{i}\boldsymbol{k}\cdot\boldsymbol{x}), \tag{B7}$$

$$= \sum_{\boldsymbol{k}} \frac{\boldsymbol{k}}{k^2} [\hat{\boldsymbol{q}}(\boldsymbol{k},t)\cdot\boldsymbol{k}](\exp(\mathrm{i}\boldsymbol{k}\cdot\boldsymbol{r}/2) - \exp(-\mathrm{i}\boldsymbol{k}\cdot\boldsymbol{r}/2)) \exp(\mathrm{i}\boldsymbol{k}\cdot\boldsymbol{x}), \tag{B8}$$

$$= \sum_{\boldsymbol{k}} \frac{\boldsymbol{k}}{k^2} [\hat{\boldsymbol{q}}(\boldsymbol{k},t)\cdot\boldsymbol{k}] 2\mathrm{i} \sin(\boldsymbol{k}\cdot\boldsymbol{r}/2) \exp(\mathrm{i}\boldsymbol{k}\cdot\boldsymbol{x}). \tag{B9}$$

Similarly, we can write

$$\delta \boldsymbol{q}(\boldsymbol{x},\boldsymbol{r},t) = \boldsymbol{q}^+(\boldsymbol{x},\boldsymbol{r},t) - \boldsymbol{q}^-(\boldsymbol{x},\boldsymbol{r},t), \tag{B10}$$

$$= \sum_{\boldsymbol{k}} \hat{\boldsymbol{q}}(\boldsymbol{k},t) 2\mathrm{i} \sin(\boldsymbol{k}\cdot\boldsymbol{r}/2) \exp(\mathrm{i}\boldsymbol{k}\cdot\boldsymbol{x}), \tag{B11}$$

and then calculate its irrotational centroid part

$$\delta \boldsymbol{q}_{\bar{I}}(\boldsymbol{x},\boldsymbol{r},t) = \sum_{\boldsymbol{k}} \frac{\boldsymbol{k}}{k^2} [\hat{\boldsymbol{q}}(\boldsymbol{k},t)\cdot\boldsymbol{k}] 2\mathrm{i} \sin(\boldsymbol{k}\cdot\boldsymbol{r}/2) \exp(\mathrm{i}\boldsymbol{k}\cdot\boldsymbol{x}), \tag{B12}$$

which shows that $\delta \boldsymbol{q}_I(\boldsymbol{x},\boldsymbol{r},t) = \delta \boldsymbol{q}_{\bar{I}}(\boldsymbol{x},\boldsymbol{r},t)$. By combining this with $\delta \boldsymbol{q} = \delta \boldsymbol{q}_I + \delta \boldsymbol{q}_S = \delta \boldsymbol{q}_{\bar{I}} + \delta \boldsymbol{q}_{\bar{S}}$, we also have $\delta \boldsymbol{q}_S(\boldsymbol{x},\boldsymbol{r},t) = \delta \boldsymbol{q}_{\bar{S}}(\boldsymbol{x},\boldsymbol{r},t)$, which is what we wanted to show.

Next we demonstrate that $\boldsymbol{a}_{\Pi_{\bar{I}}}(\boldsymbol{k},\boldsymbol{r},t) = \boldsymbol{a}_{\mathcal{T}_{\bar{I}}}(\boldsymbol{x},\boldsymbol{r},t)$ in homogeneous/periodic turbulence. We list the following expressions for the vectors and tensors related to these two terms:

$$\widehat{\delta u_j}(\boldsymbol{k},\boldsymbol{r},t) = 2\mathrm{i} \sin(\boldsymbol{k}\cdot\boldsymbol{r}/2)\hat{u}_j(\boldsymbol{k},t), \tag{B13}$$

$$\widehat{(u_j^+ + u_j^-)/2}(\boldsymbol{k},\boldsymbol{r},t) = \cos(\boldsymbol{k}\cdot\boldsymbol{r}/2)\hat{u}_j(\boldsymbol{k},t), \tag{B14}$$

$$\widehat{\frac{\partial \delta u_i}{\partial r_j}}(\boldsymbol{k},\boldsymbol{r},t) = \mathrm{i}k_j \cos(\boldsymbol{k}\cdot\boldsymbol{r}/2)\hat{u}_i(\boldsymbol{k},t), \tag{B15}$$

$$\widehat{\frac{\partial \delta u_i}{\partial x_j}}(\boldsymbol{k},\boldsymbol{r},t) = -2k_j \sin(\boldsymbol{k}\cdot\boldsymbol{r}/2)\hat{u}_i(\boldsymbol{k},t). \tag{B16}$$

By use of these equations, the Fourier coefficients of the transport terms read

$$\widehat{\boldsymbol{a}_{\mathcal{T}}}(\boldsymbol{k},\boldsymbol{r},t) = \sum_{\boldsymbol{k}=\boldsymbol{k}'+\boldsymbol{k}''} -2 \sin(\boldsymbol{k}''\cdot\boldsymbol{r}/2) \cos(\boldsymbol{k}'\cdot\boldsymbol{r}/2)\hat{u}_j(\boldsymbol{k}')k_j''\hat{\boldsymbol{u}}(\boldsymbol{k}''), \tag{B17}$$

$$\widehat{\boldsymbol{a}_{\Pi}}(\boldsymbol{k},\boldsymbol{r},t) = \sum_{\boldsymbol{k}=\boldsymbol{k}'+\boldsymbol{k}''} -2 \sin(\boldsymbol{k}'\cdot\boldsymbol{r}/2) \cos(\boldsymbol{k}''\cdot\boldsymbol{r}/2)\hat{u}_j(\boldsymbol{k}')k_j''\hat{\boldsymbol{u}}(\boldsymbol{k}''). \tag{B18}$$

Their irrotational parts are given per (A1*a*,*b*),

$$\widehat{\boldsymbol{a}_{\mathcal{T}_{\bar{I}}}}(\boldsymbol{k},\boldsymbol{r},t) = -\frac{\boldsymbol{k}}{k^2} \sum_{\boldsymbol{k}=\boldsymbol{k}'+\boldsymbol{k}''} 2 \sin(\boldsymbol{k}''\cdot\boldsymbol{r}/2) \cos(\boldsymbol{k}'\cdot\boldsymbol{r}/2)\hat{u}_j(\boldsymbol{k}')k_j''\hat{u}_l(\boldsymbol{k}'')k_l', \tag{B19}$$

$$\widehat{\boldsymbol{a}_{\Pi_{\bar{I}}}}(\boldsymbol{k},\boldsymbol{r},t) = -\frac{\boldsymbol{k}}{k^2} \sum_{\boldsymbol{k}=\boldsymbol{k}'+\boldsymbol{k}''} 2 \sin(\boldsymbol{k}'\cdot\boldsymbol{r}/2) \cos(\boldsymbol{k}''\cdot\boldsymbol{r}/2)\hat{u}_j(\boldsymbol{k}')k_j''\hat{u}_l(\boldsymbol{k}'')k_l'. \tag{B20}$$

If we employ the trigonometric identity $\sin x \cos y = \frac{1}{2}[\sin(x+y) + \sin(x-y)]$, we get

$$\widehat{a_{\mathcal{T}_{\bar{l}}}}(\boldsymbol{k}, \boldsymbol{r}, t) = -\frac{\boldsymbol{k}}{k^2} \sum_{\boldsymbol{k}=\boldsymbol{k}'+\boldsymbol{k}''} [\sin(\boldsymbol{k}\cdot\boldsymbol{r}/2) + \sin(\boldsymbol{k}''\cdot\boldsymbol{r}/2 - \boldsymbol{k}'\cdot\boldsymbol{r}/2)]\hat{u}_j(\boldsymbol{k}')k_j''\hat{u}_l(\boldsymbol{k}'')k_l', \tag{B21}$$

$$\widehat{a_{\Pi_{\bar{l}}}}(\boldsymbol{k}, \boldsymbol{r}, t) = -\frac{\boldsymbol{k}}{k^2} \sum_{\boldsymbol{k}=\boldsymbol{k}'+\boldsymbol{k}''} [\sin(\boldsymbol{k}\cdot\boldsymbol{r}/2) - \sin(\boldsymbol{k}''\cdot\boldsymbol{r}/2 - \boldsymbol{k}'\cdot\boldsymbol{r}/2)]\hat{u}_j(\boldsymbol{k}')k_j''\hat{u}_l(\boldsymbol{k}'')k_l'. \tag{B22}$$

Consider the term $\sin(\boldsymbol{k}''\cdot\boldsymbol{r}/2 - \boldsymbol{k}'\cdot\boldsymbol{r}/2)\hat{u}_j(\boldsymbol{k}')k_j''\hat{u}_l(\boldsymbol{k}'')k_l'$. If one adds this term with the wavenumber triad $\boldsymbol{k}' = \boldsymbol{k}^a$ and $\boldsymbol{k}'' = \boldsymbol{k}^b \neq \boldsymbol{k}^a$ with the same term with the wavenumber triad $\boldsymbol{k}' = \boldsymbol{k}^b$ and $\boldsymbol{k}'' = \boldsymbol{k}^a$, the result is zero. Furthermore, in the case of $\boldsymbol{k}^a = \boldsymbol{k}^b$ this term is zero per incompressibility. This yields that this term does not contribute instantaneously in the above expressions such that we attain the final result (see § 3.3 and (3.22))

$$\widehat{a_{\mathcal{T}_{\bar{l}}}}(\boldsymbol{k}, \boldsymbol{r}, t) = \widehat{a_{\Pi_{\bar{l}}}}(\boldsymbol{k}, \boldsymbol{r}, t) = -\frac{\boldsymbol{k}}{k^2}\sin(\boldsymbol{k}\cdot\boldsymbol{r}/2) \sum_{\boldsymbol{k}=\boldsymbol{k}'+\boldsymbol{k}''} \hat{u}_j(\boldsymbol{k}')k_j''\hat{u}_l(\boldsymbol{k}'')k_l'. \tag{B23}$$

Appendix C. Irrotational and solenoidal dynamics in non-homogeneous turbulence

Here we deduce the generalized Tsinober equations and the irrotational and solenoidal NSD and KHMH equations applicable to non-homogeneous turbulence. Consider the twice continously differentiable vector field $\boldsymbol{q}(\boldsymbol{x}, t)$ defined on a domain $V \subseteq \mathbb{R}^3$ with the bounding surface S. This field can be uniquely decomposed into the irrotational and solenoidal vector fields

$$\boldsymbol{q}(\boldsymbol{x}, t) = \boldsymbol{q}_I(\boldsymbol{x}, t) + \boldsymbol{q}_S(\boldsymbol{x}, t) = -\boldsymbol{\nabla}_{\boldsymbol{x}}\boldsymbol{\phi}(\boldsymbol{x}, t) + \boldsymbol{\nabla}_{\boldsymbol{x}} \times \boldsymbol{B}(\boldsymbol{x}, t). \tag{C1}$$

The solution to this problem under very general conditions (Sprössig 2010) is $\boldsymbol{q}_I = \boldsymbol{q}_{IV} + \boldsymbol{q}_{IB}$ and $\boldsymbol{q}_S = \boldsymbol{q}_{SV} + \boldsymbol{q}_{SB}$, where the solenoidal and irrotational volume and boundary terms are given in (A2)–(A5).

Consider an incompressible fluid that satisfies the incompressible vorticity equation

$$\boldsymbol{\nabla}_{\boldsymbol{y}} \times \left(\frac{\partial \boldsymbol{u}}{\partial t} + \boldsymbol{u}\cdot\boldsymbol{\nabla}_{\boldsymbol{y}}\boldsymbol{u} - \nu\nabla_{\boldsymbol{y}}^2\boldsymbol{u} - \boldsymbol{f}\right) = 0. \tag{C2}$$

By comparing this equation with (A4), it is clear that the vorticity equation can be used to derive an evolution equation for the solenoidal volume parts of the NS terms. We can apply the following operator to this equation:

$$-\frac{1}{4\pi}\int_V \mathrm{d}\boldsymbol{y}\frac{\boldsymbol{x}-\boldsymbol{y}}{|\boldsymbol{x}-\boldsymbol{y}|^3} \times \left[\boldsymbol{\nabla}_{\boldsymbol{y}} \times \left(\frac{\partial \boldsymbol{u}}{\partial t} + (\boldsymbol{u}\cdot\boldsymbol{\nabla}_{\boldsymbol{y}})\boldsymbol{u} - \nu\nabla_{\boldsymbol{y}}^2\boldsymbol{u} - \boldsymbol{f}\right)\right] = 0. \tag{C3}$$

Using (A4), we rewrite (C3) as

$$\left(\frac{\partial \boldsymbol{u}}{\partial t}\right)_{SV} + (\boldsymbol{u}\cdot\boldsymbol{\nabla}_{\boldsymbol{x}}\boldsymbol{u})_{SV} = (\nu\nabla_{\boldsymbol{x}}^2\boldsymbol{u})_{SV} + \boldsymbol{f}_{SV}. \tag{C4}$$

We can in a similar manner obtain the evolution equation for the irrotational volume NS terms from the Poisson equation for pressure

$$\frac{1}{4\pi}\int_V \mathrm{d}\boldsymbol{y}\frac{\boldsymbol{x}-\boldsymbol{y}}{|\boldsymbol{x}-\boldsymbol{y}|^3}\left[\boldsymbol{\nabla}_{\boldsymbol{y}}\cdot\left(\boldsymbol{u}\cdot\boldsymbol{\nabla}_{\boldsymbol{y}}\boldsymbol{u} + \frac{1}{\rho}\boldsymbol{\nabla}_{\boldsymbol{y}}p - \boldsymbol{f}\right)\right] = 0, \tag{C5}$$

which yields

$$(\boldsymbol{u}\cdot\boldsymbol{\nabla}_{\boldsymbol{x}}\boldsymbol{u})_{IV} = \left(-\frac{1}{\rho}\boldsymbol{\nabla}_{\boldsymbol{x}}p\right)_{IV} + \boldsymbol{f}_{IV}. \tag{C6}$$

Equations (C4) and (C6) state that in all incompressible turbulent flows, the solenoidal accelerations from volume contributions balance with solenoidal forces from volume contributions and irrotational accelerations from volume contributions balance with irrotational forces from volume contributions. The former can be viewed as an integrated vorticity equation which dictates a part of the solenoidal NS dynamics, while the latter equation as an integrated pressure Poisson equation that dictates a part of the irrotational NS dynamics. Due to the non-local character of the solenoidal and irrotational volume terms, we reformulate these equations in terms of a full NS term minus boundary terms, e.g. for the time derivative $(\partial\boldsymbol{u}/\partial t)_{SV} = \partial\boldsymbol{u}/\partial t - (\partial\boldsymbol{u}/\partial t)_{IB} - (\partial\boldsymbol{u}/\partial t)_{SB}$. The irrotational volume component (see (A2)) involves an integral of the divergence of the respective term $(\boldsymbol{\nabla}_{\boldsymbol{y}}\cdot\boldsymbol{q}(\boldsymbol{y}))$. Thus, due to incompressibility, the time derivative and viscous terms have zero volume irrotational components, $(\partial\boldsymbol{u}/\partial t)_{IV} = (\nu\nabla_{\boldsymbol{x}}^2\boldsymbol{u})_{IV} = 0$. The solenoidal volume component (see (A4)) involves an integral of the curl of the respective term, and as the curl of the pressure gradient equals zero, this term will have a zero solenoidal volume component, $(-(1/\rho)\boldsymbol{\nabla}_{\boldsymbol{x}}p)_{SV} = 0$. We rewrite the solenoidal volume terms in (C4) in terms of combinations of full terms and boundary terms to obtain

$$\begin{aligned}\frac{\partial \boldsymbol{u}}{\partial t} + ((\boldsymbol{u}\cdot\boldsymbol{\nabla}_{\boldsymbol{x}})\boldsymbol{u})_S &= \nu\nabla_{\boldsymbol{x}}^2\boldsymbol{u} + \boldsymbol{f}_S \\ &+ \left(\frac{\partial \boldsymbol{u}}{\partial t}\right)_{IB} - (\nu\nabla_{\boldsymbol{x}}^2\boldsymbol{u})_{IB} + \left(\frac{\partial \boldsymbol{u}}{\partial t}\right)_{SB} + ((\boldsymbol{u}\cdot\boldsymbol{\nabla}_{\boldsymbol{x}})\boldsymbol{u})_{SB} - (\nu\nabla_{\boldsymbol{x}}^2\boldsymbol{u})_{SB} - \boldsymbol{f}_{SB},\end{aligned} \tag{C7}$$

where the sum of the four rightmost terms on the right-hand side equals $(-(1/\rho)\boldsymbol{\nabla}_{\boldsymbol{x}}p)_{SB}$ as the NS equations are satisfied at the boundary. By using this simplification and writing out all the boundary terms, we arrive at

$$\begin{aligned}\frac{\partial \boldsymbol{u}}{\partial t} + ((\boldsymbol{u}\cdot\boldsymbol{\nabla}_{\boldsymbol{x}})\boldsymbol{u})_S &= \nu\nabla_{\boldsymbol{x}}^2\boldsymbol{u} + \boldsymbol{f}_S \\ &- \frac{1}{4\pi}\int_S \mathrm{d}S_{\boldsymbol{y}}\frac{\boldsymbol{x}-\boldsymbol{y}}{|\boldsymbol{x}-\boldsymbol{y}|^3}\left[\hat{\boldsymbol{n}}_{\boldsymbol{y}}\cdot\left(\frac{\partial \boldsymbol{u}}{\partial t} - \nu\nabla_{\boldsymbol{y}}^2\boldsymbol{u}\right)\right] - \frac{1}{4\pi}\int_S \mathrm{d}S_{\boldsymbol{y}}\frac{\boldsymbol{x}-\boldsymbol{y}}{|\boldsymbol{x}-\boldsymbol{y}|^3}\times\left[\hat{\boldsymbol{n}}_{\boldsymbol{y}}\times\boldsymbol{\nabla}_{\boldsymbol{y}}\frac{1}{\rho}p\right].\end{aligned} \tag{C8}$$

By rewriting the irrotational volume components in (C6) in terms of the full terms and the boundary terms, we have

$$((\boldsymbol{u}\cdot\boldsymbol{\nabla}_{\boldsymbol{x}})\boldsymbol{u})_I = -\frac{1}{\rho}\boldsymbol{\nabla}_{\boldsymbol{x}}p + \boldsymbol{f}_I + ((\boldsymbol{u}\cdot\boldsymbol{\nabla}_{\boldsymbol{x}})\boldsymbol{u})_{IB} - \left(-\frac{1}{\rho}\boldsymbol{\nabla}_{\boldsymbol{x}}p\right)_{IB} - \boldsymbol{f}_{IB} - \left(-\frac{1}{\rho}\boldsymbol{\nabla}_{\boldsymbol{x}}p\right)_{SB}, \tag{C9}$$

where the sum of the irrotational boundary terms equals $-(\partial\boldsymbol{u}/\partial t)_{IB} + (\nu\nabla_{\boldsymbol{x}}^2\boldsymbol{u})_{IB}$ by the NS equations at the boundary. If we use this relation and write out all boundary terms,

we have

$$((\boldsymbol{u}\cdot\boldsymbol{\nabla}_x)\boldsymbol{u})_I = -\frac{1}{\rho}\boldsymbol{\nabla}_x p + \boldsymbol{f}_I + \frac{1}{4\pi}\int_S \mathrm{d}S_y \frac{\boldsymbol{x}-\boldsymbol{y}}{|\boldsymbol{x}-\boldsymbol{y}|^3}\left[\hat{\boldsymbol{n}}_y\cdot\left(\frac{\partial \boldsymbol{u}}{\partial t} - \nu\nabla_y^2\boldsymbol{u}\right)\right] + \frac{1}{4\pi}\int_S \mathrm{d}S_y \frac{\boldsymbol{x}-\boldsymbol{y}}{|\boldsymbol{x}-\boldsymbol{y}|^3}\times\left[\hat{\boldsymbol{n}}_y\times\boldsymbol{\nabla}_y\frac{1}{\rho}p\right]. \tag{C10}$$

Equations (C8) and (C10) are generalizations of (3.4)–(3.5) for homogeneous/periodic turbulence and these equations are valid for all incompressible turbulent flows. The difference from homogeneous/periodic turbulence is the collection of boundary terms

$$\boldsymbol{R}(\boldsymbol{x},t) \equiv \frac{1}{4\pi}\int_S \mathrm{d}S_y \frac{\boldsymbol{x}-\boldsymbol{y}}{|\boldsymbol{x}-\boldsymbol{y}|^3}\left[\boldsymbol{n}_y\cdot\left(\frac{\partial \boldsymbol{u}}{\partial t} - \nu\nabla_y^2\boldsymbol{u}\right)\right] + \frac{1}{4\pi}\int_S dS_y \frac{\boldsymbol{x}-\boldsymbol{y}}{|\boldsymbol{x}-\boldsymbol{y}|^3}\times\left[\boldsymbol{n}_y\times\boldsymbol{\nabla}_y\frac{1}{\rho}p\right], \tag{C11}$$

$$= -(\boldsymbol{a}_l)_{IB} + (\boldsymbol{a}_\nu)_{IB} - (\boldsymbol{a}_p)_{SB}, \tag{C12}$$

which yields the final expressions for the general irrotational and solenoidal NS equations

$$\frac{\partial \boldsymbol{u}}{\partial t} + ((\boldsymbol{u}\cdot\boldsymbol{\nabla}_x)\boldsymbol{u})_S = \nu\nabla_x^2\boldsymbol{u} + \boldsymbol{f}_S - \boldsymbol{R}(\boldsymbol{x},t), \tag{C13}$$

$$((\boldsymbol{u}\cdot\boldsymbol{\nabla}_x)\boldsymbol{u})_I = -\frac{1}{\rho}\boldsymbol{\nabla}_x p + \boldsymbol{f}_I + \boldsymbol{R}(\boldsymbol{x},t). \tag{C14}$$

In homogeneous/periodic turbulence all the boundary terms in $\boldsymbol{R}(\boldsymbol{x},t)$ equal zero individually (see the last paragraph of Appendix A), such that we recover (3.4)–(3.5). In general, the boundary terms will be non-zero and differ in different flows, e.g. at a solid wall the boundary term from the time derivative will vanish because of no-slip and the NS equations at the wall can be used to rewrite the boundary terms as a non-local function of the pressure gradient only.

The NSD irrotational and solenoidal equations in general turbulent flows are obtained by subtracting the solenoidal and irrotational NS equations (C13) and (C14) at $\boldsymbol{x}-\boldsymbol{r}/2$ from the same equations at $\boldsymbol{x}+\boldsymbol{r}/2$,

$$\frac{\partial \delta\boldsymbol{u}}{\partial t} + \delta\boldsymbol{a}_{cS} = \delta\boldsymbol{a}_\nu + \delta\boldsymbol{f}_S - \delta\boldsymbol{R}, \tag{C15}$$

$$\delta\boldsymbol{a}_{cI} = -\frac{1}{\rho}\boldsymbol{\nabla}_{\boldsymbol{x}}\delta p + \delta\boldsymbol{f}_I + \delta\boldsymbol{R}. \tag{C16}$$

The rephrasing of the irrotational and solenoidal NSD equations in terms of the interscale and interspace transport terms can also be performed for non-homogeneous turbulence. We derive the centroid irrotational and solenoidal NSD equations similarly as for the NS irrotational and solenoidal equations by starting with the NSD equation (3.9). This yields

the equations

$$\delta \boldsymbol{a}_l + \boldsymbol{a}_{\mathcal{T}_{\bar{S}}} + \boldsymbol{a}_{\Pi_{\bar{S}}} = \delta \boldsymbol{a}_v + \delta \boldsymbol{f}_{\bar{S}} - \bar{\boldsymbol{R}}, \tag{C17}$$

$$\boldsymbol{a}_{\mathcal{T}_{\bar{I}}} + \boldsymbol{a}_{\Pi_{\bar{I}}} = \delta \boldsymbol{a}_p + \delta \boldsymbol{f}_{\bar{I}} + \bar{\boldsymbol{R}}, \tag{C18}$$

where

$$\bar{\boldsymbol{R}}(\boldsymbol{x}, \boldsymbol{r}, t) \equiv \frac{1}{4\pi} \int_S \mathrm{d}S_{\boldsymbol{y}} \frac{\boldsymbol{x} - \boldsymbol{y}}{|\boldsymbol{x} - \boldsymbol{y}|^3} [\hat{\boldsymbol{n}}_{\boldsymbol{y}} \cdot (\delta \boldsymbol{a}_l - \delta \boldsymbol{a}_v)] - \frac{1}{4\pi} \int_S \mathrm{d}S_{\boldsymbol{y}} \frac{\boldsymbol{x} - \boldsymbol{y}}{|\boldsymbol{x} - \boldsymbol{y}|^3} \times [\hat{\boldsymbol{n}}_{\boldsymbol{y}} \times \delta \boldsymbol{a}_p], \tag{C19}$$

$$= -(\delta \boldsymbol{a}_l)_{IB} + (\delta \boldsymbol{a}_v)_{IB} - (\delta \boldsymbol{a}_p)_{SB}. \tag{C20}$$

These boundary terms are individually equal to zero in homogeneous/periodic turbulence for the analogue reason as for the NS dynamics. Regarding the irrotational dynamics, in general, $\boldsymbol{a}_{\mathcal{T}_{\bar{I}}} \neq \boldsymbol{a}_{\Pi_{\bar{I}}}$, but the irrotational volume terms are always equal, $(\boldsymbol{a}_{\mathcal{T}})_{\overline{IV}} = (\boldsymbol{a}_{\Pi})_{\overline{IV}}$ from (A2) and

$$\boldsymbol{\nabla}_{\boldsymbol{x}} \cdot \boldsymbol{a}_{\Pi} = \boldsymbol{\nabla}_{\boldsymbol{x}} \cdot \boldsymbol{a}_{\mathcal{T}} = \frac{1}{2} \left(\frac{\partial u_k^+}{\partial x_i^+} \frac{\partial u_i^+}{\partial x_k^+} - \frac{\partial u_k^-}{\partial x_i^-} \frac{\partial u_i^-}{\partial x_k^-} \right). \tag{C21}$$

The solenoidal interscale transfer term $\boldsymbol{a}_{\Pi_{\bar{S}}}$ in non-homogeneous turbulence can be written as

$$\begin{aligned} \boldsymbol{a}_{\Pi_{\bar{S}}}(\boldsymbol{x}, \boldsymbol{r}, t) = &-\frac{1}{4\pi} \int_V \mathrm{d}\boldsymbol{y} \frac{\boldsymbol{x} - \boldsymbol{y}}{|\boldsymbol{x} - \boldsymbol{y}|^3} \times [\boldsymbol{\nabla}_{\boldsymbol{y}} \times \boldsymbol{a}_{\Pi}(\boldsymbol{y}, \boldsymbol{r}, t)] \\ &+ \frac{1}{4\pi} \int_S \mathrm{d}S_{\boldsymbol{y}} \frac{\boldsymbol{x} - \boldsymbol{y}}{|\boldsymbol{x} - \boldsymbol{y}|^3} \times [\hat{\boldsymbol{n}}_{\boldsymbol{y}} \times \boldsymbol{a}_{\Pi}(\boldsymbol{y}, \boldsymbol{r}, t)], \end{aligned} \tag{C22}$$

where the surface integral is of a smaller order of magnitude than the volume integral away from boundaries and increasingly so with increasing $\langle Re_\lambda \rangle_t$ (verified in our periodic DNS). Hence, for a qualitative interpretation of $\boldsymbol{a}_{\Pi_{\bar{S}}}$, we consider $\boldsymbol{a}_{\Pi_{\bar{S}}} \approx \boldsymbol{a}_{\Pi_{\overline{SV}}}$ with

$$\begin{aligned} (\boldsymbol{\nabla}_{\boldsymbol{x}} \times \boldsymbol{a}_{\Pi})_i = &\, \delta u_k \frac{\partial \delta \omega_i}{\partial r_k} - \frac{\delta \omega_k}{2} \frac{s_{ij}^+ + s_{ij}^-}{2} - \frac{\omega_k^+ + \omega_k^-}{4} \delta s_{ij} \\ &+ \frac{\epsilon_{ijk}}{2} \left[\frac{\partial u_l^+}{\partial x_j^+} \frac{\partial u_k^-}{\partial x_l^-} - \frac{\partial u_l^-}{\partial x_j^-} \frac{\partial u_k^+}{\partial x_l^+} \right], \end{aligned} \tag{C23}$$

where s_{ij} is the strain-rate tensor and ϵ_{ijk} is the Levi-Civita tensor. This set of terms constitutes a part of the nonlinear term in the evolution equation for the vorticity difference $\delta\boldsymbol{\omega}(\boldsymbol{x}, \boldsymbol{r}, t)$, i.e. vorticity at scales $|\boldsymbol{r}|$ and smaller, as $\boldsymbol{\nabla}_{\boldsymbol{x}} \times \delta \boldsymbol{a}_c = \boldsymbol{\nabla}_{\boldsymbol{x}} \times (\boldsymbol{a}_{\Pi} + \boldsymbol{a}_{\mathcal{T}})$. If one contracts (C23) with $2\delta\boldsymbol{\omega}$, the right-hand side corresponds to nonlinear terms that determine the evolution of the enstrophy $|\delta\boldsymbol{\omega}|^2$ at scales smaller or comparable to $|\boldsymbol{r}|$. We interpret the first term on the right-hand side of (C23) as vorticity interscale transfer. By the connection to $|\delta\boldsymbol{\omega}|^2$, we interpret the second and third terms as related to the enstrophy production/destruction at scales smaller or comparable to $|\boldsymbol{r}|$ due to interactions between the vorticity and strain fields. These three terms justify the interpretation of $\boldsymbol{a}_{\Pi_{\bar{S}}}$ being related non-locally in space to vortex stretching and compression dynamics. The last term in (C23) appears in $\boldsymbol{\nabla}_{\boldsymbol{x}} \times \boldsymbol{a}_{\mathcal{T}_{\overline{SV}}}$ with a negative sign such that these terms cancel.

The exact solenoidal and irrotational KHMH equations follow from contracting (C17) and (C18) with $2\delta\boldsymbol{u}$,

$$\mathcal{A}_t + \mathcal{T}_{\bar{S}} + \Pi_{\bar{S}} = \mathcal{D}_{r,\nu} + \mathcal{D}_{X,\nu} - \epsilon + I_{\bar{S}} - 2\delta\boldsymbol{u}\cdot\bar{\boldsymbol{R}}, \tag{C24}$$

$$\mathcal{T}_{\bar{I}} + \Pi_{\bar{I}} = \mathcal{T}_p + I_{\bar{I}} + 2\delta\boldsymbol{u}\cdot\bar{\boldsymbol{R}}, \tag{C25}$$

where $\mathcal{T}_{\overline{IV}} = \Pi_{\overline{IV}}$. This shows that the solenoidal and irrotational KHMH equations can be extended to non-homogeneous turbulence. In contrast to homogeneous/periodic turbulence, in general, boundary terms couple the irrotational and solenoidal dynamics.

References

Alves Portela, F., Papadakis, G. & Vassilicos, J.C. 2020 The role of coherent structures and inhomogeneity in near-field interscale turbulent energy transfers. *J. Fluid Mech.* **896**, A16.

Bardina, J., Ferziger, J. & Reynolds, W. 1980 Improved subgrid-scale models for large-eddy simulation. In *13th Fluid and Plasma Dynamics Conference*. AIAA.

Bhatia, H., Norgard, G., Pascucci, V. & Bremer, P. 2013 The Helmholtz-Hodge decomposition–a survey. *IEEE Trans. Vis. Comput. Graph.* **19** (8), 1386–1404.

Chen, J.G., Cuvier, C., Foucaut, J.-M., Ostovan, Y. & Vassilicos, J.C. 2021 A turbulence dissipation inhomogeneity scaling in the wake of two side-by-side square prisms. *J. Fluid Mech.* **924**, A4.

Chen, J.G. & Vassilicos, J.C. 2022 Scalings of scale-by-scale turbulence energy in non-homogeneous turbulence. *J. Fluid Mech.* **938**, A7.

Chevillard, L., Roux, S.G., Lévêque, E., Mordant, N., Pinton, J.-F. & Arnéodo, A. 2005 Intermittency of velocity time increments in turbulence. *Phys. Rev. Lett.* **95** (6), 64501.

Cimarelli, A., Abbà, A. & Germano, M. 2019 General formalism for a reduced description and modelling of momentum and energy transfer in turbulence. *J. Fluid Mech.* **866**, 865–896.

Dairay, T., Lamballais, E., Laizet, S. & Vassilicos, J.C. 2017 Numerical dissipation vs subgrid-scale modelling for large eddy simulation. *J. Comput. Phys.* **337**, 252–274.

Frisch, U. 1995 *Turbulence: The Legacy of A. N. Kolmogorov*. Cambridge University Press.

Galanti, B. & Tsinober, A. 2000 Self-amplification of the field of velocity derivatives in quasi-isotropic turbulence. *Phys. Fluids* **12** (12), 3097–3099.

Goto, S. & Vassilicos, J.C. 2016 Unsteady turbulence cascades. *Phys. Rev.* E **94** (5), 53108.

Gulitski, G., Kholmyansky, M., Kinzelbach, W., Lüthi, B., Tsinober, A. & Yorish, S. 2007 Velocity and temperature derivatives in high-Reynolds-number turbulent flows in the atmospheric surface layer. Part 2. Accelerations and related matters. *J. Fluid Mech.* **589**, 83–102.

Helmholtz, H. 1867 On integrals of the hydrodynamical equations, which express vortex-motion. *Lond. Edinb. Dubl. Phil. Mag.* **33** (226), 485–512.

Hill, R.J. 2002 Exact second-order structure-function relationships. *J. Fluid Mech.* **468**, 317–326.

Hill, R.J. & Thoroddsen, S.T. 1997 Experimental evaluation of acceleration correlations for locally isotropic turbulence. *Phys. Rev.* E **55** (2), 1600–1606.

Kolmogorov, A.N. 1941*a* Dissipation of energy in locally isotropic turbulence. *Dokl. Akad. Nauk SSSR* **32**, 16–18.

Kolmogorov, A.N. 1941*b* On the degeneration of isotropic turbulence in an incompressible viscous fluid. *Dokl. Akad. Nauk SSSR* **31**, 538–540.

Kolmogorov, A.N. 1941*c* The local structure of turbulence in incompressible viscous fluid for very large Reynolds numbers. *Dokl. Akad. Nauk SSSR* **30**, 301–305.

Leschziner, M. 2016 *Statistical Turbulence Modelling for Fluid Dynamics, Demystified: An Introductory Text for Graduate Engineering Students*. Imperial College Press.

Linkmann, M. 2018 Effects of helicity on dissipation in homogeneous box turbulence. *J. Fluid Mech.* **856**, 79–102.

Linkmann, M., Buzzicotti, M. & Biferale, L. 2018 Multi-scale properties of large eddy simulations: correlations between resolved-scale velocity-field increments and subgrid-scale quantities. *J. Turbul.* **19** (6), 493–527.

Linkmann, M.F. & Morozov, A. 2015 Sudden relaminarization and lifetimes in forced isotropic turbulence. *Phys. Rev. Lett.* **115** (13), 134502.

McComb, W.D., Berera, A., Yoffe, S.R. & Linkmann, M.F. 2015*a* Energy transfer and dissipation in forced isotropic turbulence. *Phys. Rev.* E **91** (4), 43013.

McComb, W.D., Linkmann, M.F., Berera, A., Yoffe, S.R. & Jankauskas, B. 2015*b* Self-organization and transition to turbulence in isotropic fluid motion driven by negative damping at low wavenumbers. *J. Phys.* A **48** (25), 25FT01.

Monin, A.S, Yaglom, A.M. & Lumley, J.L. 1975 *Statistical Fluid Mechanics*, vol. 2. MIT Press.

Moser, R.D., Haering, S.W. & Yalla, G.R. 2021 Statistical properties of subgrid-scale turbulence models. *Annu. Rev. Fluid Mech.* **53** (1), 255–286.

Patterson, G.S. & Orszag, S.A. 1971 Spectral calculations of isotropic turbulence: efficient removal of aliasing interactions. *Phys. Fluids* **14** (11), 2538–2541.

Podvigina, O. & Pouquet, A. 1994 On the non-linear stability of the 1:1:1 ABC flow. *Physica* D **75** (4), 471–508.

Pope, S.B. 2000 *Turbulent Flows*. Cambridge University Press.

Sagaut, P. 2000 *Large Eddy Simulation for Incompressible Flows: An Introduction*, 1st edn. Springer.

Schumacher, J., Scheel, J.D., Krasnov, D., Donzis, D.A., Yakhot, V. & Sreenivasan, K.R. 2014 Small-scale universality in fluid turbulence. *Proc. Natl Acad. Sci. USA* **111** (30), 10961–10965.

Sprössig, W. 2010 On Helmholtz decompositions and their generalizations–an overview. *Math. Meth. Appl. Sci.* **33** (4), 374–383.

Sreenivasan, K.R. & Antonia, R.A. 1997 The phenomenology of small-scale turbulence. *Annu. Rev. Fluid Mech.* **29** (1), 435–472.

Steiros, K. 2022 Balanced nonstationary turbulence. *Phys. Rev.* E **105** (3), 35109.

Stewart, A.M. 2012 Longitudinal and transverse components of a vector field. *Sri Lankan J. Phys.* **12**, 33.

Tang, S.L., Antonia, R.A. & Djenidi, L. 2022 Transport equations for the normalized *n*th-order moments of velocity derivatives in grid turbulence. *J. Fluid Mech.* **930**, A31.

Tennekes, H. 1975 Eulerian and Lagrangian time microscales in isotropic turbulence. *J. Fluid Mech.* **67** (3), 561–567.

Tsinober, A., Vedula, P. & Yeung, P.K. 2001 Random Taylor hypothesis and the behavior of local and convective accelerations in asotrophic turbulence. *Phys. Fluids* **13** (7), 1974–1984.

Vassilicos, J.C. 2015 Dissipation in turbulent flows. *Annu. Rev. Fluid Mech.* **47** (1), 95–114.

Vedula, P. & Yeung, P.K. 1999 Similarity scaling of acceleration and pressure statistics in numerical simulations of isotropic turbulence. *Phys. Fluids* **11** (5), 1208–1220.

Vela-Martín, A. 2022 Subgrid-scale models of isotropic turbulence need not produce energy backscatter. *J. Fluid Mech.* **937**, A14.

Xu, H., Ouellette, N.T., Vincenzi, D. & Bodenschatz, E. 2007 Acceleration correlations and pressure structure functions in high-Reynolds number turbulence. *Phys. Rev. Lett.* **99** (20), 204501.

Yasuda, T. & Vassilicos, J.C. 2018 Spatio-temporal intermittency of the turbulent energy cascade. *J. Fluid Mech.* **853**, 235–252.

Yeung, P.K., Pope, S.B., Lamorgese, A.G. & Donzis, D.A. 2006 Acceleration and dissipation statistics of numerically simulated isotropic turbulence. *Phys. Fluids* **18** (6), 65103.